Development of a Self-sustained Model to Predict the Water Desalination Performance of the Membrane Distillation Process

by

Sadaf Noamani

A thesis submitted in partial fulfillment of the requirements for the degree of

Master of Science

Department of Mechanical Engineering
University of Alberta

Abstract

The water crisis, as a result of the rapid increase in world population, industrialization, and extreme drought, has become one of the most global risks to the environmental, social, and economic development of many countries. The release of contaminants from the industries into water resources also causes more unreliable and aggravating situations for freshwater availability, especially in water-stressed regions. Therefore, it is essential to develop novel techniques for producing freshwater from seawater or contaminated wastewater and improve the current desalination and water treatment processes. Membrane distillation (MD) has gained a lot of attention in the last decade due to its high potential to produce clean water. MD is a thermally driven separation process in which vapor pressure difference across a hydrophobic membrane acts as a driving force for water desalination. It is an alternative solution for conventional seawater desalination methods, such as distillation and multi-stage flash due to its simple design, high production, and efficiency.

In this study, comprehensive experimental and theoretical studies of mass and heat transfer in different configurations of MD systems were investigated to provide a strong framework for a deeper understanding and optimization of the process. Inspired by the ∈-NTU method, a new theoretical model was first developed based on heat and mass transfer analyses of the direct contact membrane ditillation (DCMD) process. Although extensive research has been carried out on the modeling of the DCMD process, they mostly relied on some experimentally-determined parameters. The results from our model, which is independent to the experimentally measurement values (self-sustained model), were in good agreement with experimental results, with only a maximum 10% deviation. The results showed that feed temperature and membrane porosity, pore size, and thickness were the most effective parameters on the permeate flux and energy efficiency on the DCMD system. A 60% increase in the temperature of the feed solution increased the permeate flux and energy efficiency by 181% and 20%, respectively. Also, by almost a 20% increase in membrane porosity, the permeate flux and energy efficiency increased about 30% and 21%, respectively. The developed model was also used to minimize the undesirable effects of temperature and concentration polarizations and allowed for the proposal of optimum conditions for achieving higher performance in terms of energy efficiency and permeate flux. Following the same method, in the second part of this thesis, another important configuration of the MD process, i.e., air gap membrane distillation (AGMD), was modeled. The results of our model matched well with AGMD experimental results, with less than 4% deviation. Using the developed model, the AGMD performance was also systematically investigated in terms of permeate flux, energy efficiency, and temperature and concentration polarization effects, and the results are compared with the DCMD configuration. The results showed that feed temperature, thickness of the air-gap and flow rate had the most significant impact on the permeate flux and energy efficiency. In contrast, the membrane thermal conductivity and porosity did not play a determining role. A 60% increase in the feed temperature increased the permeate flux by 200 %. By increasing the flow rate from 0.2 to 8 LPM, the permeate flux was enhanced 67.19%. The air-gap thickness increment from 0.6 to 5.6 mm caused a 36.8% reduction in permeate flux. In our comparative study, the permeate flux and gained output ratio (GOR) for DCMD were 56.6% and 27.3% higher as compared to AGMD at the same conditions. However, the fraction of the energy transferring by the vapor molecules through the membrane and air gap (thermal efficiency) of the AGMD process was 24.7% larger than that of the DCMD process. The developed model provides solutions to minimize the undesirable effects of temperature and concentration polarization and proposes an optimum design map to achieve higher energy efficiency and permeate flux.

Preface

This thesis is an original work by Sadaf Noamani and highlights the comprehensive theoretical and experimental study of the membrane distillation process for wastewater treatment, mainly desalination application.

Chapter 3 and parts of chapter 2 of this thesis have been submitted to the *Desalination* and revision is requested. Title: **“Development of a self-sustained model to predict the performance of direct contact membrane distillation”**.

Chapter 4 and parts of chapter 2 of this thesis is ready for submission to the *Industrial & Engineering Chemistry Research*., Title: **“Development of a self-sustained model to predict the performance of air gap membrane distillation and comparative study with direct contact membrane distillation”**.

Parts of this thesis were published as a book chapter of “Nanocomposite membrane for water and gas separation” titled **“Prospects of nanocomposite membranes for water treatment by membrane distillation.”**

Dedicated to

My lovely parents,

And

Alireza, my supportive twin brother

Acknowledgments

I would like to express my sincere gratitude to my supervisor, Dr. Mohtada Sadrzadeh for his encouragement, patience, motivation, and immense knowledge. His guidance helped me tremendously in all the time of research and writing this thesis. He has been an excellent support and guidance throughout my journey. I am grateful to him for giving me an opportunity in his research group to pursue my M.Sc. degree.

I would like to thank Dr. Shirin Niroomand and Dr. Masoud Rastgar for their support, helpful suggestions, contribution, and their insightful comments on this research. I would like to thank my lab colleagues Pooria Karami, Behnam Khorshidi, Laleh Shamaeighahfarokhi, Ali Mohammadtabar, Farshad Mohammadtabar, Muhammad Islam, Adham Riad, Asad Asad, Amirreza Sohrabi for providing me suggestions, idea discussion and training for experiments.

I would like to thank my parents, my brother and sister in law who have been extremely supportive throughout the process.

Table of Contents

List of Tables

List of Figures

Nomenclature

A	Area	m^2
B_M	Total mass transfer coefficient	$\mathrm{kg/(m^2 sPa)}$
C	Conductivity	μS/cm
$\mathrm{c_p}$	Specific heat capacity	J/(kgK)
CPC	Concentration polarization coefficient	-
D	Water diffusion coefficient	$\mathrm{m^2/s}$
D_h	Hydraulic diameter of the flow channel	m
d_pore	Diameter of the membrane pores	μm
E	Emissivity	-
$\in -\mathrm{NTU}$	Effectiveness-Number of Transfer Units	-
g	gravitational acceleration	$\mathrm{m/s^2}$
Gr	Grashof number	-
h	Heat transfer coefficient	$\mathrm{W/(m^2K)}$
ΔH	Enthalpy or Latent Heat of vaporization of water	kJ/kg
J_w	Mass flux	$\mathrm{kg/(m^2s)}$
k	Thermal conductivities	W/mK
K	Overall mass transfer coefficient of salt ions	m/s
K_B	The Boltzmann constant	1.380649×10^{-23} J/K
K_M	Effective thermal conductivity of the membrane	W/mK
$\mathrm{K_n}$	Knudsen number	-
MW_w	Molecular weight of water	Kg/mol
$\dot{m}$	Flow rate	Kg/s
Δm	Mass	Kg
Nu	Nusselt number	-
P	Pressure	Pa
Pr	Prandtl number	-
Q	Heat transfer	$\mathrm{W/m^2}$
Q_H	The energy that was consumed for heating the feed solution	W
Q_M	Heat transfer through the membrane	$\mathrm{W/m^2}$
Q_cm	Heat conduction through the membrane material	$\mathrm{W/m^2}$
r	Radios of membrane pore size	μm
R	The universal gas constant	8.314 J/(Kmole)
Re	Reynolds number	-
S	Salt concentration	gr/L
T	Temperature	K
t	Time	hour
TPC	Temperature polarization coefficient	-
U	Overall heat transfer coefficient	$\mathrm{W/(m^2K)}$

x	Mole fraction	-

Greek symbols

μ	Viscosity	Kg/(ms)
η	Thermal efficiency	%
β	Thermal expansion	1/K
γ	Activity coefficient	-
δ	Thickness	μm
ε	Membrane porosity	%
λ	Mean free path of the transported molecules through membrane pores	m
ρ	Density	Kg/m^3
σ	The collision diameter of water molecules	2.641×10^{-10} m
τ	Tortuosity	-
ϑ	Kinematic viscousity	m^2/S

Subscripts

ag	Air gap
air, pore	Air inside pores
avg	Average
bf	Bulk feed
bp	Bulk Permeate
c	Cold
c,ag	Conduction in the air gap
c,m	Conduction in membrane
c,M-ag	Conduction through the membrane and air gap
cp	Condensing plate
dc	Direct contact
f	Feed
film	Water film on the cooling plate
gas	Air within the pores
h	Hot
in	Inlet
k	Knudsen
m or M	membrane
M-ag	Membrane to the air gap
mf	membrane surface on the feed side
mp	membrane surface on the permeate side
out	Outlet
p	Permeate
r	radiation
s	surface
v	Vapors/Vaporization

v,ag	Vapor in the air gap
v,m	Vapor in membrane
w	Water
wf	Water in feed
wvf	Water vapor feed
wvp	Water vapor permeate
$pore$	Pores
∞	Free stream conditions

Chapter 1

1 Introduction

1.1 Background and overview of desalination processes

Water is an essential need for the survival of humans, animals, and the ecosystem. There are different natural forms of water resources on the surface, under the ground, in the oceans, and even frozen in glaciers and ice caps. However, only 2.5% of these resources are considered freshwater. Only one-third of this small amount is unfrozen freshwater, which is mostly found as groundwater, and only a small fraction is available to humans as in rivers and lakes above the ground [1]. Moreover, although water covers 71% of the surface of the earth, more than 97% of this water is salt water that is unsuitable for direct human usage [2].

On the other hand, water resources deal with serious threats because of human activities, climate change, and aggravating water scarcity. Human activities, population growth, urbanization, industrial and agricultural activities, urban and rural waste, oil spills, and extreme drought cause detrimental effects on freshwater resources [3,4]. Moreover, the produced wastewater from the industries is increasing worldwide. Over 80% to 95% of the world's wastewater in various regions is released to the environment without any treatment, which adversely affects the human health, ecosystem and causes a reduction in the available surface and groundwater resources [5–9]. Currently, about 700 million people are living over the world in the areas of water scarcity (water supplies <1000 m^3 per person), and it is expected that 1.8 billion people will be living in areas with absolute water scarcity (water supplies <500 m^3 per person) until the year 2025, which means that two-third of world's population could be living under water-stressed situations [10–12]. Thereby, a shortage of water could be the main problem in the 21st century that the world population deals with [13]. All these issues have triggered an increase in the need for freshwater supply and have been calling for numerous efforts toward improving existing water treatment processes and the development of new techniques to produce potable water from seawater and recover usable water from industrial and municipal wastewater streams [1,14].

1.2 Freshwater production techniques

There are some technologies to meet the growing demand for freshwater by water and wastewater treatment such as coagulation/flocculation, gravity separation, skimming, flotation [15–18], desalination, ion exchange, and membrane separation processes [2,13,19–22]. Each of these methods is utilized based on the application and characteristics of the feed solution that needs to be treated. The feed stream could be different wastewaters containing various organic/inorganic matters and pollutants such as municipal, industrial, agricultural wastewaters or seawater and brackish water. Besides, for the successful implementation of these techniques, the availability of energy, infrastructure, and financing is essential. Among all these separation processes, desalination has gained significant importance as a purification process over the last few decades due to large shares of saltwater on the surface of the earth. Desalination technologies satisfy the human needs for potable water, especially in regions with inadequate natural renewable supply. According to the Global Water Intelligence database DesalData, large desalination plants provide about half of the global capacity for potable water demand, with capacities larger than 50000 m^3 per day, and smaller-scale plants meet the 3.5% of the global demand with a capacity lower than 1000 m^3 per day [23].

1.3 Desalination

Desalination techniques are classified into two categories, 1) Thermal processes such as the multi-stage flash distillation (MSF), the multi-effect desalination (MED), and vapor compression distillation (VCD) [9,24–26]. 2) Membrane separation processes such as reverse osmosis (RO), microfiltration (MF), ultrafiltration (UF), nanofiltration (NF), electrodialysis (ED), and membrane distillation (MD) [8,22,27].

Thermal desalination systems involve the phase change of the feed stream. Evaporation occurs by heating the saltwater. Then, by condensation of water vapor, pure water and brine are produced as an output. However, in the membrane-based process, relying on selective membranes as a physical barrier, the dissolved contaminants are rejected, and freshwater is collected. According to the current share of the desalination market by DesalData [23] and Figure **1.1** reverse osmosis (RO) accounts for more than

50% of the world's total desalination capacity. In the Persian Gulf area, multi-stage flash (MSF) and multi-effect desalination (MED) are commonly used. However, other desalination methods rarely contribute to the global desalination market [19,28–30].

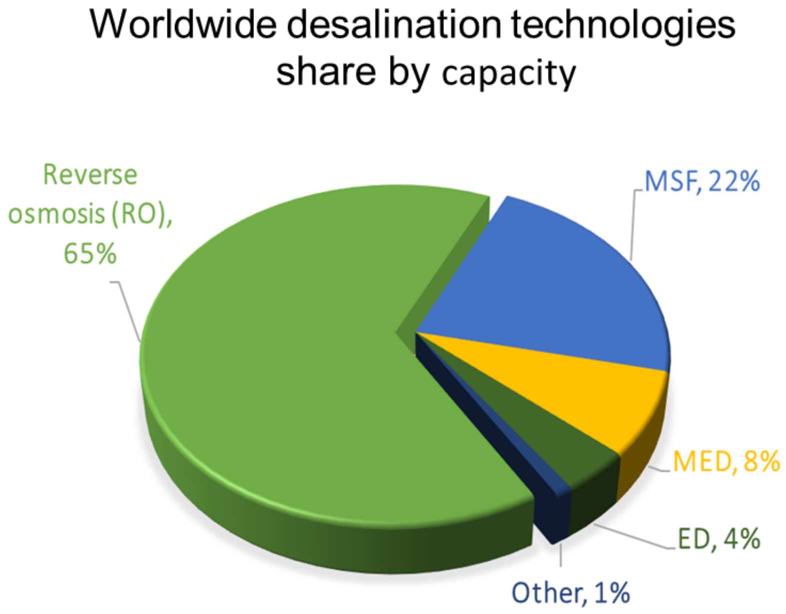

Figure 1.1. Worldwide desalination technologies share by capacity [28,29]

The technological approach and process of the most utilized desalination techniques are briefly introduced in the following section.

1.3.1 Thermal desalination processes

1.3.1.1 Multi-stage flash (MSF) distillation

MSF distillation technique is the classic industrial scale of thermal desalination, which runs along with some pre-treatments before entering seawater directly into the MSF unit, such as aeration, chlorination, coarse filtering, and pH adjustment of feed solution. The schematic of the MSF desalination process is illustrated in Figure **1.2**. Implementation of the MSF unit involves flashing portions of water into steam at multiple stages with different pressure and temperature. By repeating the process at lower and lower pressures, most of the water converts to a gaseous form that can be condensed and produce clean water.

First, the seawater is conducted to the heating section through passing all of the consecutive stages, where the brine solution is heated using the external steam source (boilers) to the highest temperature that is allowed by the plant (MSF process has shown the maximum efficiency at up to 115℃ temperature). Then, the heated seawater with the super high temperature is released into the brine solution in the first flashing chamber in which the absolute pressure is reduced to just below the feed vapor pressure at saturation condition. This causes the partial evaporation of seawater and flashing into steam until the brine solution reaches its saturation temperature. Next, after passing across the demisters, the vapor contacting the cold seawater tubes at the top of the chamber, condense, and pure water is collected in distillate trays. The concentrated feed (brine) solution is accumulated at the bottom of the chamber and then forwarded to the second flashing chamber. This process is repeated at each stage. As the feed stream passes through the successive chambers from the first towards the last one, the pressure becomes lower and provides the flashing conditions at each chamber. Moreover, the latent heat released during the condensation can be accompanied by preheating the feed stream and play the role of heat recovery in the MSF unit. MSF distillation process typically produces 10,000 to 35,000 m^3/day freshwater, and it can operate with 4 to 40 stages [28,31–34].

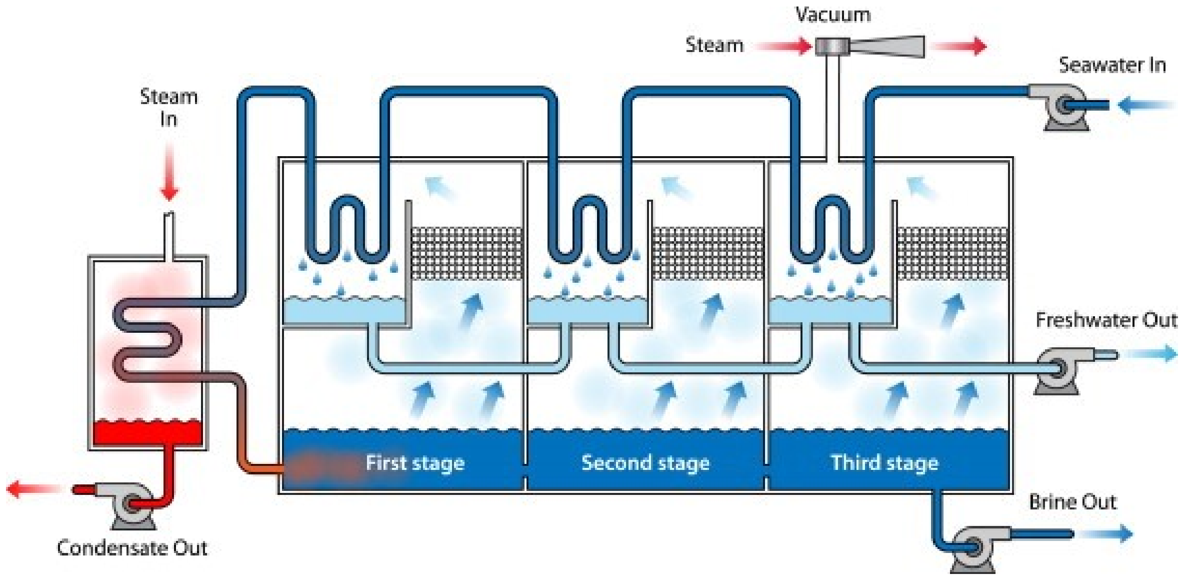

Figure 1.2. Schematic of Multi-stage flash distillation (MSF) process, Adapted with permission from ref [32]

1.3.1.2 Multi-effect desalination (MED)

The MED process is schematically demonstrated in Figure **1.3**. In this process, similar to MSF distillation, the feed solution needs pre-treatment before being introduced to the MED setup. Same as MSF distillation, the MED process utilizes pressure reduction in series of stages (usually 2 to 16 effects) with successively lower temperature and pressure to effectively separate freshwater from brine. In this process, firstly, seawater is piped into the first effect where there are warm tubes containing steam (the brine temperature here is increased to around 70℃). Then, the feed water is sprayed onto the surface of warm tubes by spray nuzzles. Once the feed solution makes the outer surface of the tubes wet, it is heated up until it reaches its boiling point. Then, the seawater evaporates partially and a brine solution is collected in the sump of the first chamber. The vapor passing through a mesh demister is conducted within evaporator tubes to the second effect. Next, by spraying of seawater onto the evaporator tubes, the vapor condenses within the tube, and pure water is piped and collected outside the chamber. The vapor of the last effect condenses within a final condenser. The released latent heat of condensation is reused to evaporate more seawater again. The MED process works at lower temperatures compared to MSF, which leads to smaller sized plant and operating costs. Moreover, the MED specific power consumption is approximately half that required for the MSF process. MED process are generally operated at capacities of 600 to 30,000 m^3/day [13,19,28,32].

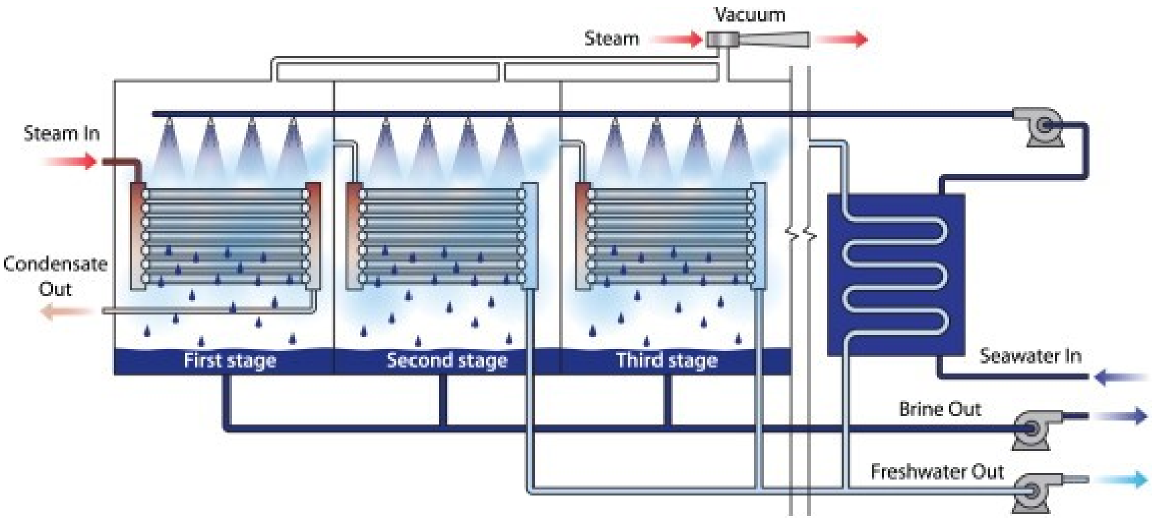

Figure 1.3. The schematic of the Multi-effect desalination (MED) process, Adapted with permission from ref [32]

1.3.1.3 Vapor compression distillation (VCD)

Vapor compression distillation is mostly similar to the MED process, but the heat is supplied by compressing the vapor and increasing its temperature (it operates at around 74℃ for effective operation). This method can be operated either by mechanical vapor compression (MVC) or thermo-vapor compression (TVC). As can be seen from Figure **1.4**, seawater enters the heat exchanger and then it is conducted to the chamber. The saltwater with lower temperature is sprayed on to the surface of the tubes containing vapor with super high temperature and evaporated. Then, the vapor is conducted to the vapor compressor to increase its temperature. Here, for MVC, the electricity is used to drive the compressor, while in TVC, a steam jet creates the lower pressure. Then, the vapor is conducted to the heat exchanger, where the heat is released, and pure water is provided by condensation. The concentrated brine solution also is removed by the recirculation pump and split into two streams. One is mixed with the incoming seawater, and the rest is pumped to the waste. The VC process usually is implemented in small-sized applications. The MVC units have smaller production capacities (100 to 3000 m^3/day) than TVC with 10,000 to 30,000 m^3/day [13,28,32,35].

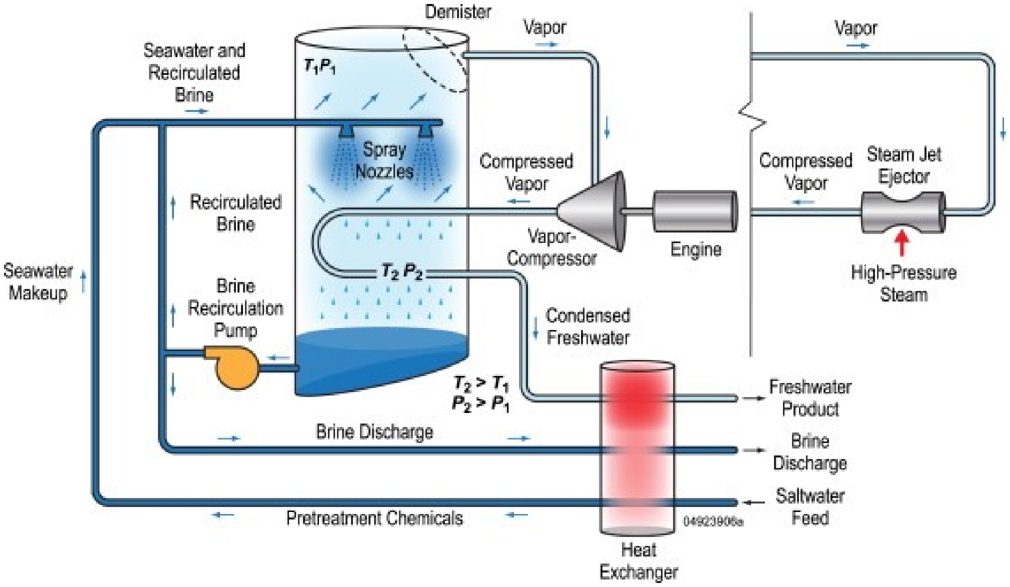

Figure 1.4. Schematic of Vapor compression distillation (VCD) process, Adapted with permission from ref [32]

1.3.2 Membrane Technology for water treatment and desalination

Membrane separation technology plays an important role in available water treatment processes as a promising method to produce freshwater from any contaminated water containing multiple sized organic pollutants, solutes, and organic materials. The driving force in the membrane filtration can be provided by a difference in pressure, temperature, concentration, or electric field across the membrane. The pressure-driven membrane processes are classified into microfiltration (MF), ultrafiltration (UF), nanofiltration (NF), and reverse osmosis (RO). The driving forces for the forward osmosis (FO) and electrodialysis (ED) are osmotic pressure gradient and electric potential across a membrane, respectively. Moreover, membrane distillation (MD) works based on temperature difference [6,8,27,36]. Among various membrane filtration methods, pressure-driven membranes are widely used for purifying solutions from any dispersed/dissolved contaminants. Especially in desalination technologies, large desalination plants make these membranes as a leading technology for treating sea/brackish water. More than 50% of total desalination capacity is associated with installations based on reverse osmosis (RO) technology. In addition, microfiltration (MF), ultrafiltration (UF), nanofiltration (NF) are more utilized in pre-treatment and post-treatment processes. RO membranes have a pore size of less than 1 nm, and they are considered as the tightest membranes. They are mainly utilized to produce high quality of sea/brackish water by separating monovalent ions. MF membranes can be used to isolate large colloidal and organic matters which have the pore size in the range of 0.05 μm to 10 μm. UF membranes have a smaller pore size than the MF membrane (10-100 μm), and they are used for removing macromolecules like protein, bacteria, and viruses. The pore size for the NF membranes is between 1 to 10 nm [36,37].

In the following, the conventional membrane technologies for commercial desalination applications are briefly explained.

1.3.2.1 Reverse osmosis (RO)

In the reverse osmosis (RO) process, a dense hydrophilic membrane is used to separate water from the dissolved salt in the solution for desalination application. The membrane only allows water to pass through the membrane, and it rejects salt ions from penetrating. The pressure greater than the osmotic pressure of the solution is required to apply as a driving force. The operating pressure ranges from 55 to 82 bars for seawater and 17 to 27 bars for brackish water [38]. The schematic of the RO filtration technique is illustrated in Figure **1.5**. In this process, the electricity is used to drive the high-pressure pump for generating the required pressure to push the water to pass through the membrane. The capacity range for RO desalination process is 0.1 m^3/day (in marine and household applications) to 395,000 m^3/day (for commercial applications) [8,32,35,37,39].

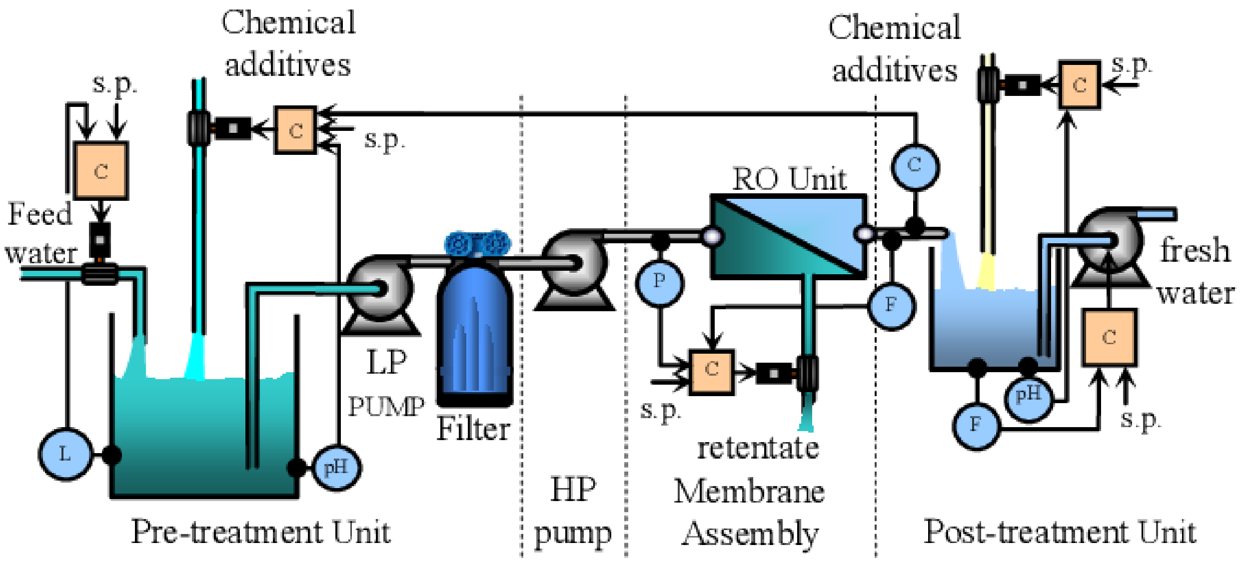

Figure 1.5. The schematic of the Reverse osmosis (RO) filtration technique, Adapted with permission from ref [40].

1.3.2.2 Electrodialysis (ED)

Water molecules, which are polar, can dissolve salt particles and make them as individual ions moving freely in the solution (such as Na^+ and Cl^-). Therefore, by applying direct current electricity between cathode and anode in the solution, salt ions move toward charged anode and cathode (e.g. Cl^- moves toward positively charged anode). Electrodialysis (ED) is the membrane technology (Figure **1.6**) that uses these ions movement for seawater desalination. The anion- and cation-selective membranes are used in this process to create two separate streams (dilute and concentrated streams). Since the driving force is an electric field, ED is only capable of removing ionic components from the solution. In addition, this technology can be operated for cleaning the membrane surface in the ED cell since salt or organic materials may tend to accumulate on the membrane surface. By reversing the flow of applied direct current, salt or organic materials are driven back into the solution, and the ED cell becomes clean. The typical capacity for an ED plants is in the range of 2 to 145,000 m^3/day [29,32,35,38].

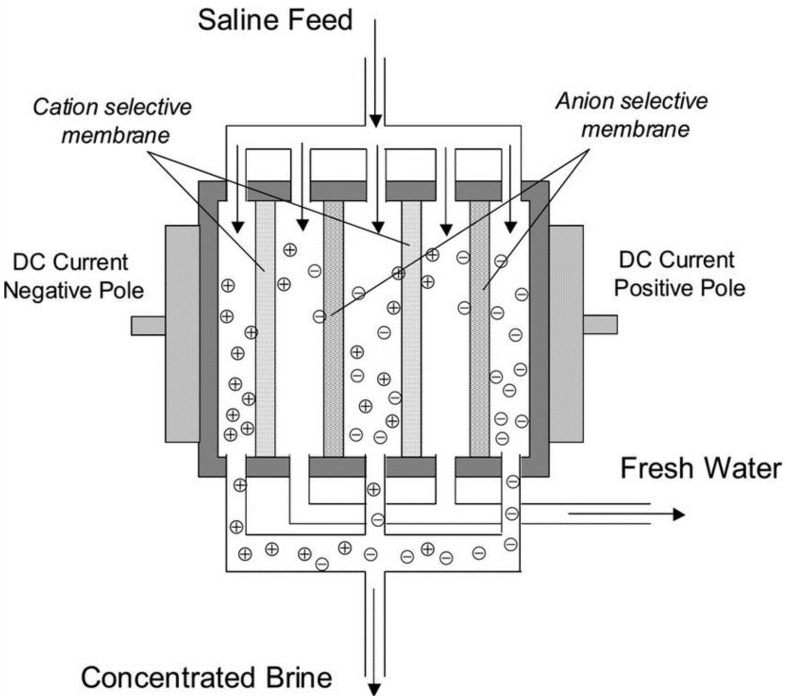

Figure 1.6. The schematic of the Electrodialysis filtration technique, Adapted with permission from ref [35] (open access)

1.4 Problems Facing Desalination

Although the problems of freshwater scarcity can be reduced significantly by conventional desalination methods, they pose some challenges in the environment. Desalination is an energy-intensive process that requires full consideration of the amount of both energy consumption and freshwater production. The energy required for desalination plants mostly originates from unsustainable and non-renewable energy sources, which makes it an unsustainable solution. Moreover, excessive usage of desalination can have noticeable detrimental impacts on the environment. The thermal desalination techniques need a large amount of fuel to provide the energy required for the desalination process compared to the equivalent of produced freshwater, which results in emissions of greenhouse gases such as Sulphur dioxide (SO_2), nitrite oxide (NO), nitrogen dioxide (NO_2), carbon monoxide (CO), carbon dioxide (CO_2) and other air pollutants [41,42]. Another concern in deployment of conventional desalination is water pollution by discharging highly concentrated brine containing many chemicals into the sea, which may cause sedimentation and adverse effects on marine life. Besides, fish or any other sea life in the seawater entering the desalination plant may be killed or trapped. Also, it could affect construction-related projects on the coastline. Moreover, in some desalination technologies, various chemicals such as (cleaning chemicals, anti-foaming, anti-corrosion, chlorine, etc.) may be engaged for pre-treatment and post-treatment processes of saline solution, which pose adverse impacts on the environment [43,44] and conventional desalination methods may fail in eliminating these harmful undissolved and dissolved chemical substances from freshwater [28]. Further issues address the costs for oceans desalination plants, which are more than any other option. Therefore, the water scarcity problem finally changes to environmental issues and energy consumption problem.

The energy consumption in desalination plants depends on different factors such as unit design, plant capacity, materials and chemicals, the quality and properties of seawater in the feed stream. In thermal desalination processes (MSF, MED, and VC), the energy consumption is not affected by the amount of salt concentration in the feed stream, and both thermal and electrical energies are needed to be consumed. However, for the membrane processes (RO and ED) the salt concentration is highly effective, and only electricity is engaged for energy consumption. Although thermal desalination methods are a more mature technology and they provide fast evaporation, they suffer from high energy consumption (typically 7 to 25 kWh m^{-3}) and scaling issues. However, membrane desalination techniques (RO and ED) consume much lower energy (1 to 12 kWh m^{-3}) [29,32]. Moreover, they do not require chemical additives, there is no phase change in these processes, they are easily controlled and scaled up, and there is no need for energy recovery devices. Therefore, based on Table **1.1**, membrane-based separation processes enjoy many advantages, compared to conventional thermal desalination methods, such as the reduction in operational expenses and reducing energy consumption. Besides, membrane-based separation technologies have smaller footprints, and they provide higher separation efficiency and productivity. In addition, they are capable of removing a wide range of pollutants from contaminated water (not only salt) such as heavy metals, mono, and multivalent ions and some micro-organisms [6,17,45]. Due to all these advantages of the membrane desalination process, RO membrane technology has become as a leading technique for new desalination installation in recent years for both sea and brackish water treatments. However, besides these benefits over thermal desalination techniques, RO membrane technology suffers from some problems such as the membrane fouling, which is the main challenge in membrane-based processes. Fouling is the accumulation of materials and contaminant particles on the surface or in the pores of the membrane, which causes clogging the membrane pores and reducing the freshwater production. RO also suffers from expensive high-pressure pumps, pressure vessels, and pressure recovery devices. Furthermore, the biggest limitation in RO desalination technology is its inability to be applied for treating high salinity streams [2,8].

Therefore, all the mentioned issues for desalination techniques and significant cost and energy consumption have motivated the efforts for the development of improved and sustainable desalination process for high productivity, energy efficiency, lower cost, and less detrimental effects on the environment. Therefore, besides improving the current desalination processes like reverse osmosis (RO), it is essential to develop novel versatile techniques for effective separation of freshwater from abundant seawater or contaminated wastewater resources [6,9,27,46].

Table 1.1. Energy consumption and average production cost of the main and conventional desalination processes (SW: seawater, BW: brackish water) [25,29,32,47–56].

Properties	**Thermal desalination techniques**				**Membrane-based desalination techniques**		
	MSF	MED	VC		RO		ED
			MVC	TVC	SW	BW	
Typical unit size (m^3/day)	10,000–70,000	600-30,000	100-3000	10,000-30,000	0.1-395000		2–145,000
Recovery rate (%)	15%-50%	15%-50%	20%-50%		30%-35%	60%-85%	50%-80%
Energy Consumption (kWh m−3)	14-27	7-25	7–12	16-26	4–6 SW	1.5–2.5	1-12
Average Cost of water (US$/m^3)	0.56-1.75	0.5-8	0.8-2.6		0.45-1.72	0.26-1.33	0.6-1.05
Product water quality (ppm)	10	10	10	10	400-500	200-500	150-500

1.5 Membrane distillation (MD)

The membrane distillation (MD) approach is the case that could be classified within both the thermal and the membrane desalination categories since it represents a thermal separation process that features a membrane. Membrane distillation is a thermally driven membrane separation process that operates under relatively low feed temperature (50°C–80°C) and atmospheric pressure. In this process, heated liquid feed (typically saline water) is brought into contact with a hydrophobic microporous membrane, while the cold-water stream flows on the other side of the membrane on the permeate side. The temperature difference between feed and permeate streams results in a vapor pressure gradient across the membrane, which moves water molecules through the membrane pores from the hot feed solution in gaseous form. The vapor molecules then condense at the cold permeate stream side. Due to the hydrophobic nature of the membranes used in MD, no liquid can penetrate through the pores unless a hydraulic pressure higher than the liquid entry pressure is applied over the membrane surface [2,21,57–

59]. Figure **1.7** is a typical schematic of the MD process. Depending on the type of configuration that the MD process is driven by, a specific condensation mechanism can occur. The four different modules that have mainly been proposed for the MD process are including Direct contact membrane distillation (DCMD), air gap membrane distillation (AGMD), vacuum membrane distillation (VMD), and sweeping gas membrane distillation (SGMD) (Figure **1.8**) [21,60]. In mentioned configurations, the feed solution is similarly in direct contact with the active side of the membrane, while their permeate sides are made by different arrangements. In the DCMD, the cold stream is in direct contact with the membrane backside. In the AGMD module, an air gap splits the membrane surface from the cold permeate fluid. The SGMD configuration is almost used for the removal of volatile vapors, where a sweeping gas is in charge of transferring the collected permeates out of the cell. In the VMD, the passed vapor molecules through the membrane pores are initially vacuumed and subsequently condensed into liquid form. Among all configurations, the DCMD is more common due to its simplicity and providing relatively high flux, however, it suffers from higher heat loss comparing to the other modules. The utilized air gap in the AGMD can partially decrease the heat loss, but it caused an additional resistance against vapor mass transfer which could be translated as less overall permeate flux [60–63].

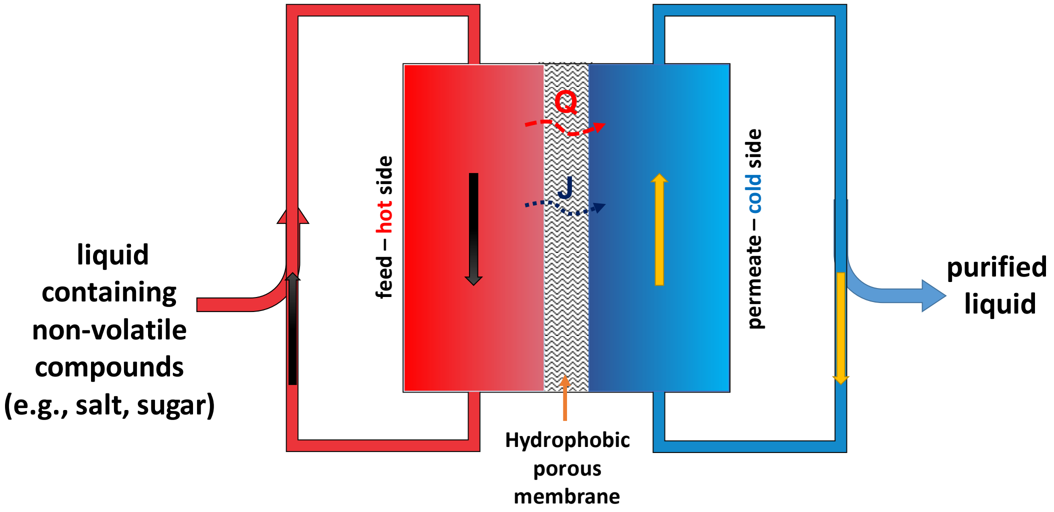

Figure 1.7. Typical schematic of the concept of MD process. The vapor passes through a hydrophobic porous membrane and condenses on the other side of the membrane. Q and J represent the mass and heat transfer, respectively. Adapted with permission from ref [22] (open access).

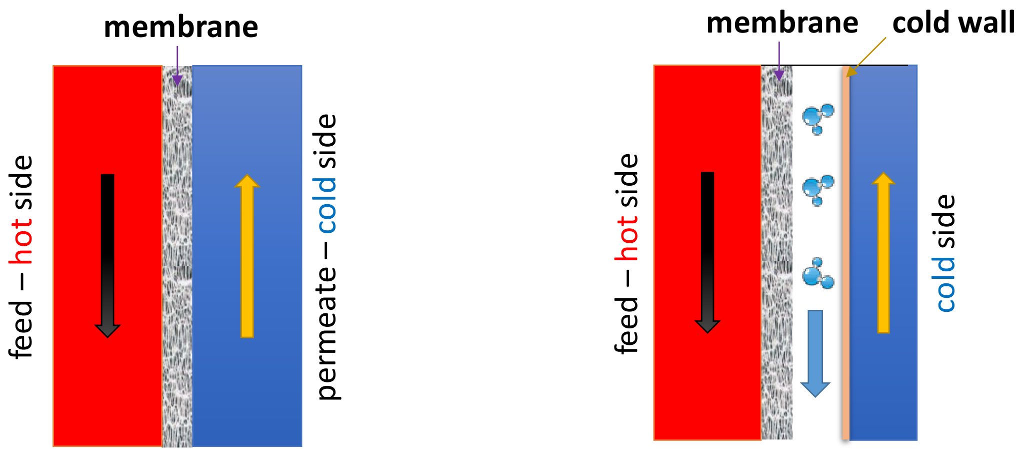

(a) DCMD: The membrane is in direct contact with the hot feed side (e.g., seawater) and the cold permeate side (e.g., pure water)

(b) AGMD: an air gap between the membrane and the cold side acts as a condenser to turn vapor into liquid

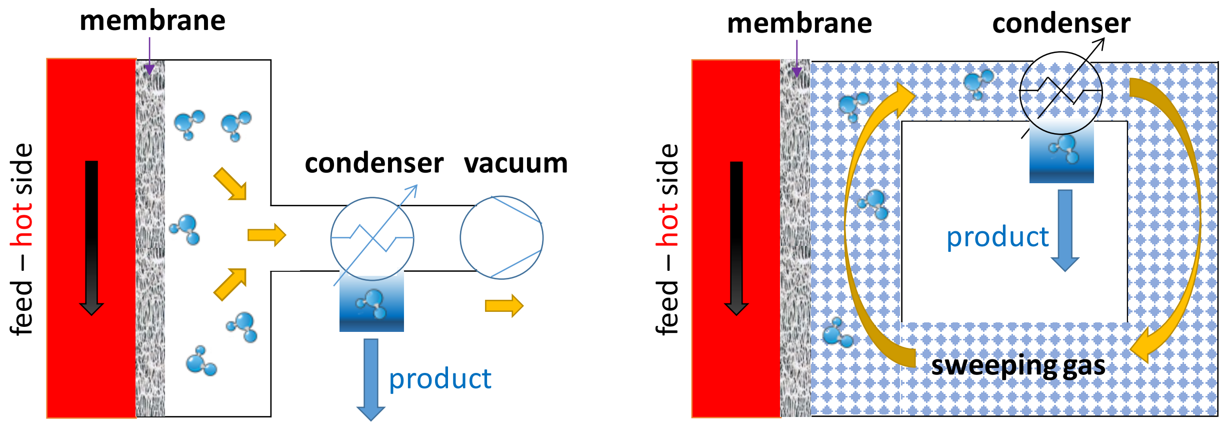

(c) VMD: the vapor is vacuumed out of the air gap. A condenser turns the vapor into liquid (product).

(d) SGMD: a cold, inert gas sweeps the transferred vapor out of the MD module. A condenser separates the vapor from the sweeping gas and turns it into liquid (product).

Figure 1.8. Four different configurations of Membrane Distillation (MD), Adapted with permission from ref [64]

Membrane distillation offers many advantages compared to other desalination methods. It can be performed at a low operating temperature (50°C – 80°C), which is lower than the boiling point of the feed solution. It can also be operated at ambient pressure, and it needs lower vapor space. It is unlimited to treat high osmotic pressure and salt concentration of feed stream, and it is capable of full rejection of all dissolved non-volatile species. Moreover, it can use any kind of low-grade waste heat or renewable energy (solar energy) for generating the required temperature difference across the membrane. The low operating temperature of the MD process can address the challenges of thermal desalination techniques with respect to their high energy consumption. Additionally, MD is also capable of overcoming the RO process challenges. MD system does not require expensive high-pressure pumps and devices because of the ambient operating pressure. Due to the absence of transmembrane pressure and the presence of hydrophobic microporous membrane, it has a lower tendency for membrane fouling. This low operating pressure also causes the MD system to have higher process safety and lower demand for membrane mechanical properties. In addition, the high chemically resistivity of common polymers used for MD membranes such as polytetrafluoroethylene (PTFE), polypropylene (PP), and polyvinylidene difluoride (PVDF), make MD be able to operate in harsh environments (concentrated acid). Moreover, it can produce higher freshwater than the RO process, even for high salinity feed solutions with lower energy consumption. It can also achieve desired salt rejection in a single pass, where the RO process needs multiple passes (pre/post-treatments). In the literature, the MD process showed a 77% recovery ratio, while it was 40.08% for RO in the same condition for seawater desalination, and the energy consumption of MD with 120 $Lm^{-2}h^{-1}$ water production was 1.5 $kWhm^{-3}$ while it was 4 $kWhm^{-3}$ for RO with 10 $Lm^{-2}h^{-1}$ water production [2,8,21,32,51,59,65]. Therefore, these advantages make the MD more attractive than other popular separation and desalination techniques. Owing to such excellent features, MD is employed in a wide range of applications, including desalination to remove non-volatile salts such as NaCl, KCl, and LiBr [66–69], completely, in the food industry to produce concentrated juice or milk [70–74], in the petrochemical industry to break azeotropic mixtures and recover volatile aromas [75–77], and in treatment of wastewater containing dyes, oils, heavy metals, and radioactive materials [78,79].

Despite all the mentioned benefits of MD, there are some obstacles which allowed to perform the MD process only on bench and pilot-scales and hindered the full deployment of the MD process in the industry [51,63,80–82]. Temperature and concentration polarization effects are one of the major challenges leading to water production decay. Another important bottleneck in the MD process is membrane pore wetting. When the liquid passes through the membrane, the membrane becomes wet, and the whole process comes to failure. Moreover, membrane and module design, and energetic and economic costs are other challenges that have to be investigated [27,51,63,80].

Therefore, as MD is a promising, yet still emerging technology for water treatment, before implementing the MD process in the industry, it is essential to develop a strong framework for a deeper understanding of effective parameters on the performance of the MD process to overcome the mentioned challenges. Mathematical modeling provides the feature to investigate how the MD process can be influential in addressing the other thermal desalination problems. Mathematical modeling also can set a strong framework for the optimization of the MD process by identifying process parameters and ideal membrane properties that lead to cost- and energy-efficient water desalination. Moreover, the impact of effective parameters such as membrane properties and operating conditions can be investigated on the performance of the MD system in terms of permeate flux, rejection, energy consumption, temperature, and concentration polarization. Quantitative comparison of different MD scenarios also provides valuable insight into the fabrication of innovative membranes, as well as smart adjustment of process parameters to diminish the adverse effect of the obstacles mentioned above.

In the next section, some previous research works of the MD modeling are presented.

1.6 Literature review

The membrane distillation process involves simultaneously interconnected heat and mass transfer mechanisms, which make it a complex process. Mathematical modeling allows us to build further insight for optimizing the system and effective investigation, which can lead to a breakthrough in the technology. So far, several theoretical models have been published in the literature for mass and heat transfer simulation in the water channels or inside the membrane for the MD process. In this section, different previous mathematical models are reviewed, and research gaps are presented.

1.6.1 Heat transfer

Heat transfer models are used to predict the temperature on the membrane interface layer at feed and permeate sides to be able to calculate the driving force, which is used as a backbone for mass transfer modeling. Several heat transfer models have been developed mostly for the forced convection in the laminar regime within the hot and cold streams channels and they used Nusselt number calculations for approximating the heat transfer coefficients. The heat transfer models in the literature mainly considered constant temperature on the membrane surface, and they developed a one-dimensional theoretical model for heat transfer. Besides, since the mass and heat transfers are connected, they utilized the obtained experimental permeate flux in the modeling algorithm or used several initial guesses for permeate flux and temperature of membrane interface [83–88]. In this type of modeling, the choice of Nu number equation which is obtained from semi-empirical correlations, should be done very carefully. Ali *et al*. [86] designed a specific membrane cell with several sensors to measure the temperature of bulk and membrane surface at both feed and permeate sides experimentally. They compared the experimental results with calculated temperature using Nu number correlation [86,87]. Moreover, they investigated the effect of flow rate and feed temperature on heat and mass transfer experimentally in the DCMD module for pure water as a feed solution [86]. Qtaishat *et al*. proposed a mathematical model for heat transfer to predict the membrane surface temperatures. They used experimentally measured values for inlet and outlet temperatures of bulk streams and permeate flux as inputs in their theoretical model and investigated the effect of bulk feed temperature on permeate flux and temperature polarization [88]. Phattaranawik *et al*. used Nu number correlations for both laminar and turbulent flow regimes to model the heat transfer in the DCMD process and investigated the effect of feed temperature on temperature polarization [85]. Moreover, in order to validate the used Nusselt equations for the heat transfer model, some authors have used aluminum foil or solid impermeable polymer sheets in the experiments instead of the membrane to compare the overall heat transfer coefficient obtained from the experiment with the calculated value from Nu number correlation. They used the Log Mean Temperature Difference (LMTD) method by measuring the inlet and outlet temperatures of the fluid stream in the membrane cell to find the overall heat transfer coefficient experimentally [84,85].

1.6.2 Mass transfer

The permeability of a porous membrane towards the gases and liquid can determine the approximation for water vapor permeation through the membrane. Moreover, it is required to relate the structural parameters of the membrane to the membrane permeability for estimating the permeate flux more realistically and accurately. However, this is not easily determined because the size and shape of the membrane pores are not known precisely. For the mass transfer modeling of vapor molecules through the membrane and the prediction of water production in the MD process, several methods have been proposed in the literature [89].

The simplest way to describe the mass transfer in the membrane region is Fick's law model. In this model, the membrane is assumed as an empty space containing stagnant air. In this method, by calculating the diffusion coefficient of water vapor through the air, the permeate flux is calculated theoretically, and then a theoretical calculation is calibrated with experimentally measured values to find the effective water production. This way does not consider any properties of the membrane in the modeling, such as porosity, pore size, and tortuosity [90]. Another introduced models for mass transfer are Schofield model [91,91,92] and Dusty-gas model (DGM) [80,93]. The Schofield model is a semi-empirical approximation for flux calculation, which is mostly determined for deaerated systems. It is dependent on the gas used for the permeation test, and it has shown a large deviation from experimental measurements [93,94]. The dusty-gas model describes the motion of gas and liquid mixture through the porous media [95]. This model is first applied by Lawson and Lloyd [94,96] for mass transfer in the DCMD process. The DGM is obtained from different empirical models, and it can simulate the mass transfer based on flow type within the membrane pores. Besides, the membrane properties (such as porosity, tortuosity, mean pore size, and membrane thickness) are considered in this method. However, it is derived for isothermal systems, while the MD is a thermally driven separation process. Nevertheless, it has been successfully applied in the MD system by using the average membrane temperature, and it has shown the accuracy for predicting the membrane permeability [97–99]. Khayet *et al*. [100] and Phattaranawik, *et al*. [101] used the Kinetic theory of gasses and DGM to propose an equation for calculating membrane permeability considering pore size distribution for non-interconnected cylindrical pores, since the membranes may not have uniform pore sizes. However, the authors claimed that the effect of pore size distribution is not noticeable for the MD process and considering the single mean pore size is adequate to model the mass transfer, especially for commercial membrane, although some discrepancies can be observed potentially for membranes which have a large standard deviation of pore size. Another method that is used for modeling heat and mass transfer in the literature is the computational fluid dynamics (CFD) method. This method is a numerical approach for simulating fluid flow in the channels. Some studies [102–104] utilized the CFD method to simulate the fluid characteristics (velocity, pressure, etc.) in the fluid channels for the spacer in the membrane test section in the MD process. They investigated the type of spacer or orientation of spacer channels on the heat transfer rate and temperature polarization . Moreover, a series of studies [105–108] focused on improving the heat and mass transfer in the fluid channels by simulating the heat flow inside the membrane cell. They assumed a constant overall mass transfer coefficient for the membrane to estimate the permeate flux locally. Also, they validated the results with experimentally measured values. Furthermore, Hwang *et al*. [109] developed a model for mass transfer inside the membrane by the CFD method. They calculated the overall mass transfer coefficient using the dusty-gas model through the membrane and predicted a local permeate flux. They also validated the model by comparison of the simulated fluxes with experimental data. Although the CFD method has been used a lot in the literature for modeling heat or mass transfer, it needs a high computational burden, making the modeling more complicated. Moreover, in most CFD studies, the geometry or physical phenomena in the channels and membrane were oversimplified, leaving room for further research.

Another introduces models are empirical approaches, which are entirely relied on experimental data. They only can represent the final output without investigating the actual phenomena that occur in the systems and channels. Artificial neural networks (ANN) [110–112] and the design of experiments (DOE) [113–115] toolbox are the two common empirical methods that have been applied to the MD process. They need a large amount of experimental data for the calibration, and the output from these models can only be used for optimizing the operating conditions. Besides, they can only be applied for a specific system, and they are not able to extrapolate to other systems.

1.6.3 Research gaps

In the previous section, the various developed models for the theoretical modeling of mass and heat transfer in the MD process were explained, and their limitations were mentioned. Nevertheless, although a lot of good theoretical models exist in the literature, more work requires to be done in the area of predicting the performance of the MD process and optimizing the module design, membrane properties, and operating parameters. Some previous modeling studies for the MD system only provided a one-dimensional model or relied on some experimentally determined parameters in the modeling, which made the simulation depend upon a specific experimental condition [86–88]. Experimental measurement of all involved parameters, particularly for larger-scale systems, is not practically feasible and requires expensive instrumentation to record and monitor the parameters associated with the MD performance. In addition, despite the development of some simplified one-dimensional models [86–88], other theoretical studies required many assumptions to predict MD system behavior [83–88], or they suffered from the high computational burden, especially the CFD simulations [102–104,109]. Moreover, in most of the previous studies, the exact details on how the simulations were set up were missing, and the permeate flux was evaluated only as of the primary response variable. However, other factors, such as module design, membrane characteristics, and operating conditions, need to be optimized and investigated. In addition, energy efficiency requires to be evaluated before industrial application deployment as an important parameter in the MD process, but it has not been included in the most previous theoretical and experimental articles. Furthermore, MD modeling studies are lacking the sensitivity analyses for all effective parameters and their interactive effects, which leaves room for more detailed exploration.

The MD system can be operated at different modes by changing temperatures, flow rates, concentrations, membranes properties, and module configuration. Therefore, in order to make the MD technology to be competitive to alternative separation and desalination techniques in the industry, first, an in-depth understanding of its full process inside the module channels and the membrane pores needs to be simulated and optimized. The physical and accurate model of the MD process can play a crucial role in predicting and improve these operational modes, system performance, and prevent an expensive and time-consuming job for doing all the analysis experimentally.

1.7 Thesis objectives

The main goal of this thesis is to develop a mathematical model for simulating heat and mass transfer in the membrane distillation process in a way to fill the mentioned research gaps in this field and provide the tool for well modeling and evaluating the MD system to be able to switch from a potential method to a real industry desalination technology.

We aim to provide a new approach for the MD process modeling to predict all the aspects of the process behavior such as temperature profile, permeate flux, energy efficiency, and temperature and concentration polarization without the need to utilize any parameter obtained from experimentation. Moreover, we tend to develop not only the simple model with a low computational burden but also with more precisely theoretical results in comparison with experimentations with the capability of applying to any systems with different dimensions and properties (self-sustained model). Additionally, the theoretical model has to be able to do the sensitivity analysis of effective parameters on the performance of the MD system to provide an optimum design map for membrane properties, module design, and operating conditions in order to have higher energy efficiency and water production.

This was achieved by getting a better understanding of the process both through experimental and theoretical results. The main objective of this thesis was met by conducting the study in the following steps:

- At the first step, an in-depth understanding of heat and mass transfer mechanisms and their essential effective parameters in fluid channels and within the membrane pores were studied
- In the second step, we applied the heat and mass transfer mechanisms for both DCMD and AGMD configurations.
- In the third step, by inspiring the Effectiveness-Number of Transfer Units (∈-NTU) method, a novel, self-sustained mathematical model was developed
- In the fourth phase, the performance of DCMD and AGMD systems was predicted in terms of permeate flux, energy efficiency, and temperature and concentration polarization by the developed mathematical model

- The predicted permeate fluxes from the theoretical model were validated with experimentally measured values for two different membranes over a wide range of operating conditions to ensure the accuracy of the developed model.
- Sensitivity analyses were conducted based on the membrane properties and operating conditions to provide an optimum design map for DCMD and AGMD systems.
- In the end, the performance of DCMD and AGMD processes were compared and guidelines to achieve higher energy efficiency and lower temperature and concentration polarization effects were provided.

1.8 Thesis Outline

Chapter 1 of the thesis gives a brief introduction to the problem of water crisis globally and the current solutions for pure water production by desalination methods. The limitations of the conventional desalination technologies are discussed, and membrane-based separation processes are presented as a possible solution to overcome the shortcomings. Among the membrane-based separation processes, MD is introduced as a future alternative to the current pressure-driven membrane-based separation processes due to its higher production, lower energy consumption and cost, and ability to treat high salinity feed solution. The principle of the MD process, its advantages and limitations are discussed. Then, the potential methods to address the challenges are mentioned. At the end of this chapter, a literature review on theoretical modeling of the MD system is presented, and the objectives of this study are explained.

In the second chapter of this dissertation, the detail of mass and heat transfer mechanisms of the MD process for both DCMD and AGMD systems are presented, and the novel mathematical modeling for predicting the system performance is introduced.

In the third chapter, the results from the developed mathematical model are compared with experimental results for the DCMD system, and sensitivity analyses are carried out to identify the effective parameters on system performance. Then optimum situation for operating conditions and membrane properties is provided for the DCMD system to achieve higher permeate flux and energy efficiency.

In chapter four, the results from the developed mathematical model are compared with experimentations for the AGMD system, and the influential factors on the performance of the AGMD system are identified by sensitivity analyses. Then an optimum design map for the AGMD system is provided based on operating conditions and membrane properties for better performance of the system. Finally, the system performance of the DCMD and AGMD process are compared.

In chapter five, the major findings of this work have been summarized. Based on the outcomes, guidelines, and recommendations are provided for overcoming the current challenges for the MD process and further development in this field.

Chapter 2

2 Materials and Methods

2.1 Development of a self-sustained model to predict the performance of the MD process

The MD process involves the simultaneous transfer of mass (*J*) and heat (*Q*) through the membrane pores because of the vapor pressure gradient and temperature difference, respectively. Here, the theoretical model based on mass and heat transfer mechanisms for both DCMD and AGMD modules is developed to predict the system performance at different operating conditions. A control volume around the membrane for the counter-current flow mode is as depicted as in Figure **2.1**. (a) and (b) for DCMD and AGMD, respectively. The transport phenomenon firstly involves the evaporation of volatile compounds or liquid over the membrane surface at the feed side due to the high temperature of the feed solution. Afterward, vapor molecules penetrate and pass through the hydrophobic membrane pores, and the vapor is finally condensed on the permeate side for the DCMD system; however, in the AGMD system, a slight gap is filled by stagnant air where vapor molecules diffuse through after passing from the membrane pores and then they are condensed on a surface of a cooling plate where the pure water is collected [13,21,116].

To calculate the mass flux and investigate the system performance, temperature, and water vapor pressure on the membrane interface layer at both feed and permeate sides and water film on the cooling plate in the AGMD module are required to calculate from heat and mass balance equations.

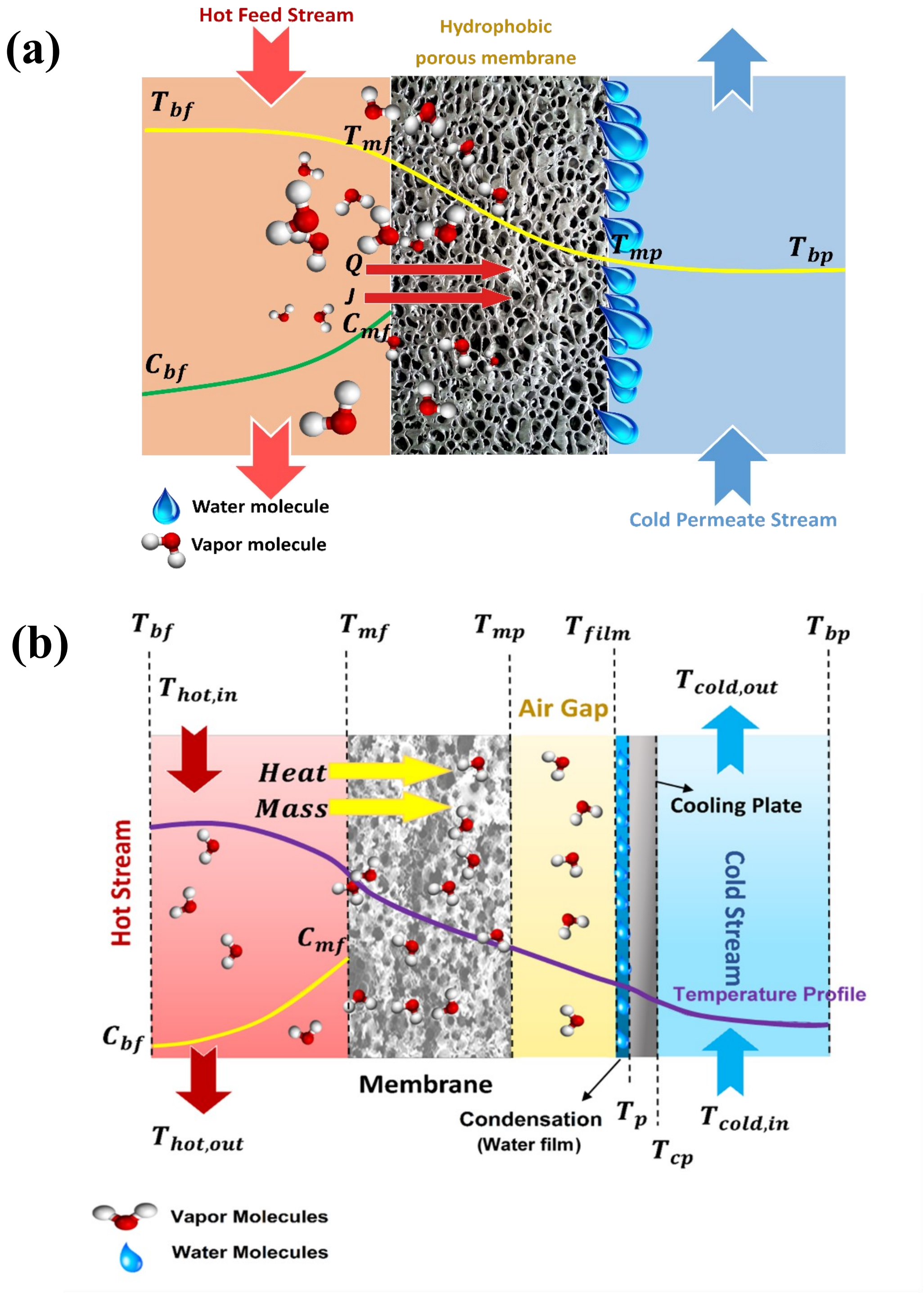

Figure 2.1. Schematic representation of heat and mass transfer across the membrane in the a) DCMD system and b) AGMD system

2.1.1 Heat Transfer

As illustrated in Figure **2.2**, three types of heat transfer may occur in the membrane test section for the DCMD system: (1) convection heat transfer from the feed side to the membrane (Q_{f} $(\mathrm{W/m^2})$), (2) heat transfer within the membrane, (Q_{M}), by heat conduction through the membrane material ($Q_{\mathrm{c,m}}$ $(\mathrm{W/m^2})$) and heat carried by water vapor through the membrane pores ($Q_{\mathrm{v,m}}$ $(\mathrm{W/m^2})$), and (3) convection heat transfer from the membrane to the permeate side (Q_{p} $(\mathrm{W/m^2})$). However, in addition to convection heat transfer from the feed side to the membrane (Q_{f}) and heat transfer through the membrane (Q_{M}), there are extra heat transfer rates after the membrane section for the AGMD system, as can be seen in Figure **2.3**. Within the air gap, the overall heat transportation includes heat conduction through the stagnant air ($Q_{\mathrm{c,ag}}$ $(\mathrm{W/m^2})$) and heat transferred by the vapor molecules ($Q_{\mathrm{v,ag}}$ $(\mathrm{W/m^2})$). Then, vapors reach to the coolant plate, where a film of water is created due to condensation. Here, we are dealing with convectional heat transfer through the liquid film to the cooling plate (Q_{film} $(\mathrm{W/m^2})$). Finally, the heat is conducted across the condensing plate (Q_{cp} $(\mathrm{W/m^2})$) and is transferred by convection to the permeate fluid (Q_{p} $(\mathrm{W/m^2})$). $Q_{\mathrm{M-ag}}$ is the heat transfer based on the actual driving force in the AGMD module between the membrane surface in the feed side with T_{mf} and water film on the cooling plate surface with T_{film}. These heat transfer rates are calculated from the equations in

Table 2.1 for the DCMD system and Table **2.2** for the AGMD system [27,117]. It is worth mentioning that, the heat transfer rate due to the radiation is negligible compared to the convection and conduction heat transfer rates (see Appendix B for calculating heat transfer rate due to radiation).

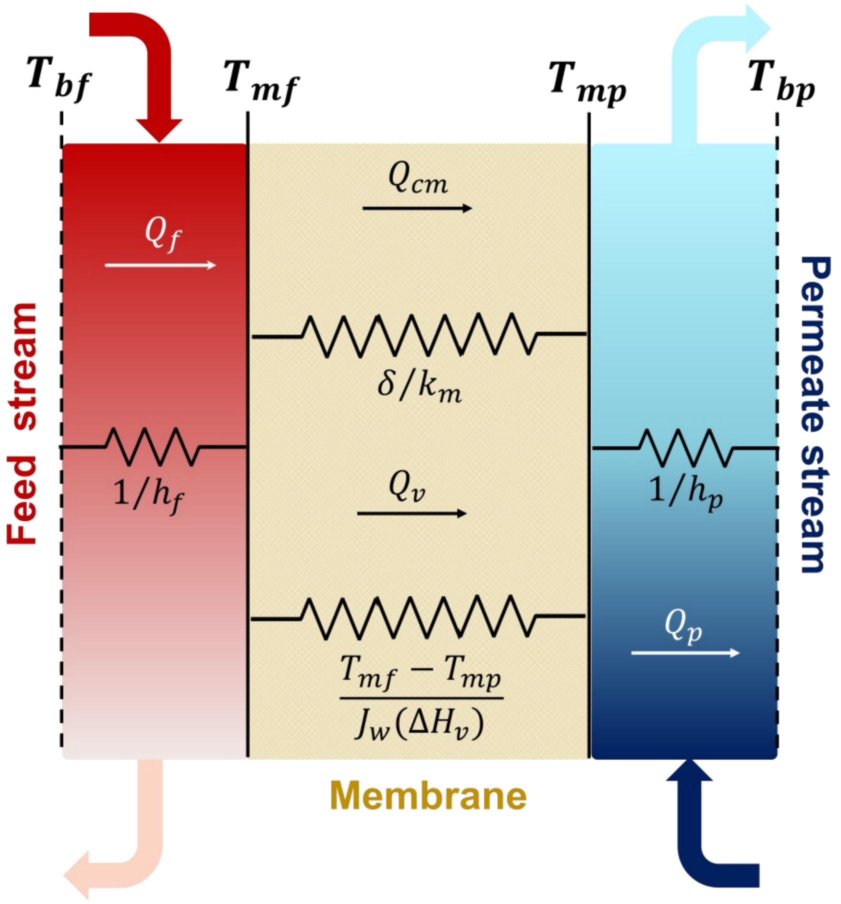

Figure 2.2. Heat transfer resistance model in the DCMD process.

Table 2.1. Heat transfer rates for the DCMD process

$Q_{\mathrm{f}} = h_{\mathrm{f}}(T_{\mathrm{bf}} - T_{\mathrm{mf}})$,	(1)
$Q_{\mathrm{M}} = Q_{\mathrm{c,m}} + Q_{\mathrm{v,m}}$, and	(2)
$Q_{\mathrm{c,m}} = \frac{K_{\mathrm{M}}}{\delta}(T_{\mathrm{mf}} - T_{\mathrm{mp}})$,	(3)
$Q_{\mathrm{p}} = h_{\mathrm{p}}(T_{\mathrm{mp}} - T_{\mathrm{bp}})$,	(4)

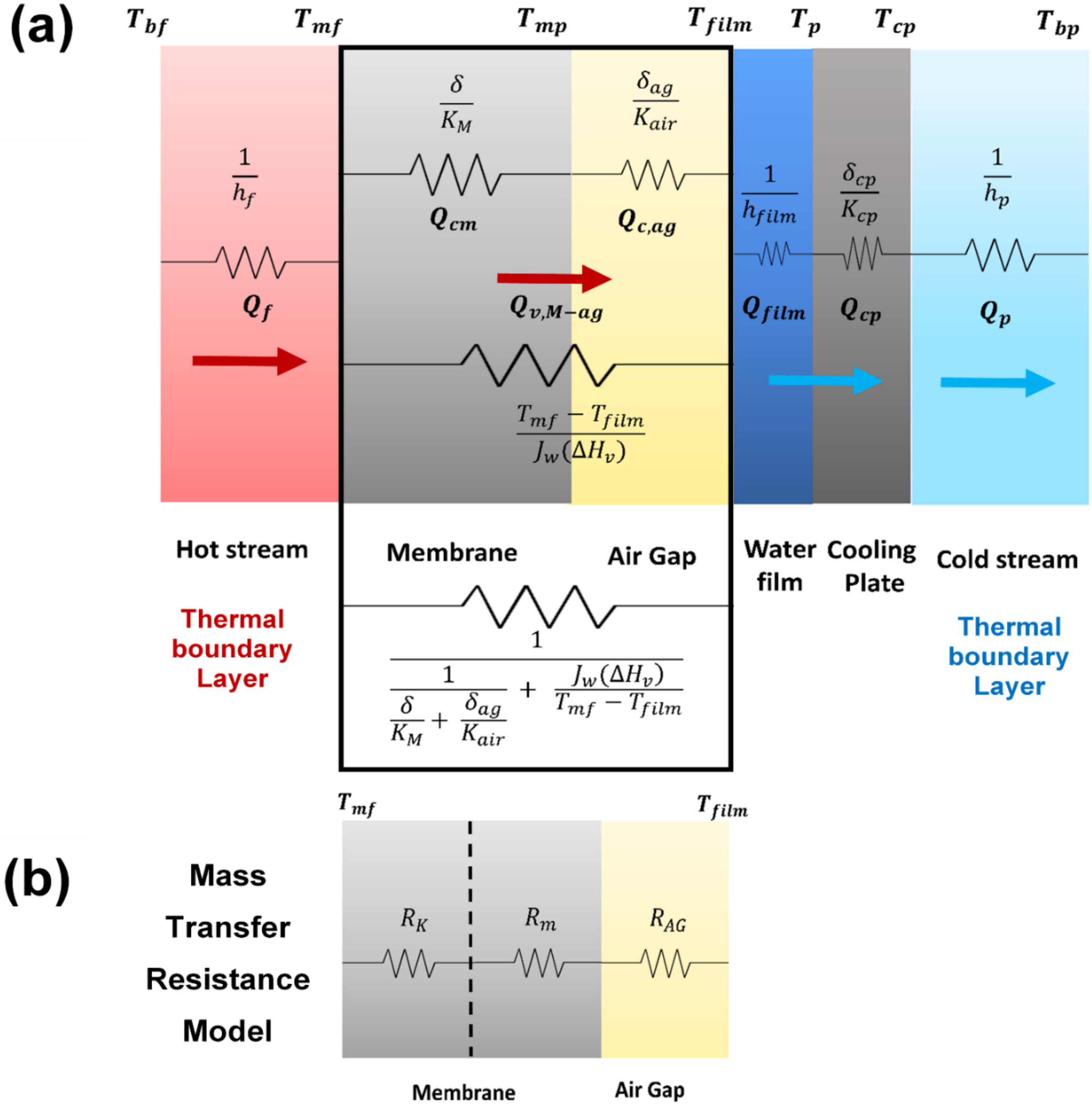

Figure 2.3. (a) Heat transfer and (b) Mass transfer resistance model in the AGMD process

Table 2.2. Heat transfer rates for the AGMD process

$Q_{\mathrm{f}} = h_{\mathrm{f}}(T_{\mathrm{bf}} - T_{\mathrm{mf,ag}})$,	(5)
$Q_{\mathrm{M}} = Q_{\mathrm{c,m}} + Q_{\mathrm{v,m}}$, and	(6)
$Q_{\mathrm{c,m}} = \frac{K_{\mathrm{M}}}{\delta}(T_{\mathrm{mf,ag}} - T_{\mathrm{mp,ag}})$,	(7)
$Q_{\mathrm{ag}} = Q_{\mathrm{c,ag}} + Q_{\mathrm{v,ag}}$, and	(8)
$Q_{\mathrm{c,ag}} = \dfrac{K_{\mathrm{air}}}{\delta_{\mathrm{ag}}}(T_{\mathrm{mp,ag}} - T_{\mathrm{film}})$	(9)
$Q_{\mathrm{M-ag}} = \frac{(T_{\mathrm{mf,ag}} - T_{\mathrm{film}})}{\frac{\delta}{K_{\mathrm{M}}} + \frac{\delta_{\mathrm{ag}}}{K_{\mathrm{air}}}} + Q_{\mathrm{v,M-ag}}$,	(10)
$Q_{\mathrm{film}} = h_{\mathrm{film}}(T_{\mathrm{film}} - T_{\mathrm{p}})$,	(11)
$Q_{\mathrm{cp}} = \frac{K_{\mathrm{cp}}}{\delta_{\mathrm{cp}}}(T_{\mathrm{p}} - T_{\mathrm{cp}})$,	(12)
$Q_{\mathrm{p}} = h_{\mathrm{p}}(T_{\mathrm{cp}} - T_{\mathrm{bp}})$,	(13)

where, T_{bf} and T_{bp} are the bulk temperatures in the feed and permeate tanks. h_{f}, h_{p} and h_{film} are the heat transfer coefficients of feed and permeate solutions and water film on condenser surface in the AGMD system respectively. K_{air} and K_{cp} are the thermal conductivities of air inside the air gap and coolant plate. δ, δ_{ag} and δ_{cp} are the membrane thickness, air gap width, and coolant plate thickness respectively. K_{M} is the effective membrane thermal conductivity which is dependent on thermal conductivity based on membrane material (k_{m}, Eq.(14)), the porosity of the membrane (ε), and air thermal conductivity inside the membrane pores (k_{gas}, Eq.(15)). Values for K_{M} is estimated based on the Maxwell equation (Eq. (17)) [2] as:

$$k_{\mathrm{m}} = \alpha_1 \times 10^{-4} T_{\mathrm{avg,m}} + \alpha_2 \times 10^{-2} , \tag{14}$$

$$k_{\mathrm{gas}} = 2.72 \times 10^{-3} + 7.75 \times 10^{-5} T_{\mathrm{avg,m}}, \tag{15}$$

$$\beta = (k_{\mathrm{m}} - k_{\mathrm{gas}})/(k_{\mathrm{m}} + 2k_{\mathrm{gas}}), \tag{16}$$

$$K_{\mathrm{M}} = \frac{k_{\mathrm{gas}}[1 + 2\beta(1-\varepsilon)]}{1 - \beta(1-\varepsilon)} \tag{17}$$

where α_1 and α_2 are constants, and their values depend on the type of membrane material. α_1 is 5.77 for both PTFE and PVDF membranes, and α_2 is 8.914 for PTFE and 0.914 for the PVDF membranes [27]. $T_{\mathrm{avg,m}}$ [K] is the average temperature between membrane surfaces at feed and permeate sides.

The Q_{v} is calculated based on the permeate flux (J_{w}) and enthalpy of vaporization (ΔH_{v}) from Eqs. (20) and (21) [2,9] as:

$$Q_{\mathrm{v}} = J_{\mathrm{w}}(\Delta H_{\mathrm{v}}), \text{ and} \tag{20}$$

$$\Delta H_{\mathrm{v}} = 1.7535 T_{\mathrm{avg}} - 2024.3 \tag{21}$$

Moreover, h_{film} can be obtained from Eq. (22) which is dependent on the acceleration due to gravity (g), the length of the cooling plate (L), density (ρ_{film}), thermal conductivity (K_{film}), viscosity (μ_{film}), enthalpy of vaporization ($\Delta H_{\mathrm{v,film}}$) of water film on the condensation plate surface in the AGMD system [21,117–120]. T_{avg} is the average temperature and it is calculated based on the average temperature between membrane surfaces at feed and permeate sides for $Q_{\mathrm{v,m}}$ ($T_{\mathrm{avg,m}} = \frac{T_{\mathrm{mf}}+T_{\mathrm{mp}}}{2}$), and the air-gap average temperature for $Q_{\mathrm{v,ag}}$, ($T_{\mathrm{avg,ag}} = \frac{T_{\mathrm{mp}}+T_{\mathrm{film}}}{2}$). Also, for $Q_{\mathrm{v,M-ag}}$, T_{avg} is obtained based on the average temperature between the membrane surface at the feed side and water film on the cooling plate ($T_{\mathrm{avg,M-ag}} = \frac{T_{\mathrm{mf}}+T_{\mathrm{film}}}{2}$).

The equations to calculate the fluid properties are described in Appendix A.

$$h_{\mathrm{film}} = \left[\frac{g(\rho_{\mathrm{film}})^2 \Delta H_{\mathrm{v,film}} K_{\mathrm{film}}{}^3}{L\mu_{\mathrm{film}}(T_{\mathrm{film}} - T_{\mathrm{p}})}\right]^{0.25} \quad (22)$$

By solving the energy balance equations (Eq. (23) and (24)) for DCMD system and (Eq. (28) and (29)) for AGMD system, at a steady-state condition in control volume around the membrane, the temperatures on the membrane surface (T_{mf}) and (T_{mp}) and water film (T_{film}) can be calculated as Eqs. (26), (27) for DCMD system, and Eqs. (31), (32) for AGMD system [9,21,64,88,121].

Table 2.3. Energy balance equations for DCMD system

$Q = Q_{\mathrm{f}} = Q_{\mathrm{M}} = Q_{\mathrm{p}} = U_{total,dc}\left(T_{\mathrm{bf}} - T_{\mathrm{bp}}\right),$	(23)
$Q = \dfrac{(T_{\mathrm{bf}} - T_{\mathrm{mf}})}{\dfrac{1}{h_{\mathrm{f}}}} = \dfrac{\left(T_{\mathrm{mf}} - T_{\mathrm{mp}}\right)}{\dfrac{1}{\left[\frac{K_{\mathrm{M}}}{\delta}\right] + [\frac{J_{\mathrm{w}}(\Delta H_{\mathrm{v}})}{T_{\mathrm{mf}} - T_{\mathrm{mp}}}]}} = \dfrac{\left(T_{\mathrm{mp}} - T_{\mathrm{bp}}\right)}{\dfrac{1}{h_{\mathrm{p}}}}$	(24)
$U_{total,dc} = \dfrac{1}{\left[\frac{1}{h_{\mathrm{f}}}\right] + \left[\dfrac{1}{\left[\frac{K_{\mathrm{M}}}{\delta}\right] + \left[\frac{J_{\mathrm{w}} \Delta H_{\mathrm{v}}}{T_{\mathrm{mf}} - T_{\mathrm{mp}}}\right]}\right] + \left[\frac{1}{h_{\mathrm{p}}}\right]}$	(25)
$T_{\mathrm{mf}} = \dfrac{k_{\mathrm{M}}\left(T_{\mathrm{bp}} + \frac{h_{\mathrm{f}}}{h_{\mathrm{p}}} T_{\mathrm{bf}}\right) + [\delta(h_{\mathrm{f}} T_{\mathrm{bf}} - J_{\mathrm{w}} \Delta H_{\mathrm{v}})]}{K_{\mathrm{M}} + [h_{\mathrm{f}}\left(\delta + \frac{K_{\mathrm{M}}}{h_{\mathrm{f}}}\right)]}$, and	(26)
$T_{\mathrm{mp}} = \dfrac{k_{\mathrm{M}}\left(T_{\mathrm{bf}} + \frac{h_{\mathrm{p}}}{h_{\mathrm{f}}} T_{\mathrm{bp}}\right) + [\delta\left(h_{\mathrm{p}} T_{\mathrm{bp}} + J_{\mathrm{w}} \Delta H_{\mathrm{v}}\right)]}{K_{\mathrm{M}} + [h_{\mathrm{p}}\left(\delta + \frac{K_{\mathrm{M}}}{h_{\mathrm{f}}}\right)]},$	(27)

Table 2.4. Energy balance equations for AGMD system

$$Q = Q_{\mathrm{f}} = Q_{\mathrm{M-\,ag}} = Q_{\mathrm{film}} = Q_{\mathrm{cp}} = Q_{\mathrm{p}} = U_{\mathrm{total,ag}}\left(T_{\mathrm{bf}} - T_{\mathrm{bp}}\right), \tag{28}$$

$$Q = U_{\mathrm{total,ag}}\left(T_{\mathrm{bf}} - T_{\mathrm{bp}}\right) = \frac{\left(T_{\mathrm{bf}} - T_{\mathrm{mf,ag}}\right)}{\frac{1}{h_{\mathrm{f}}}} = \frac{\left(T_{\mathrm{mf,ag}} - T_{\mathrm{film}}\right)}{\frac{1}{\left[\frac{1}{\left[\frac{\delta}{K_{\mathrm{M}}}\right] + \left[\frac{\delta_{\mathrm{ag}}}{K_{\mathrm{air}}}\right]}\right] + \left[\frac{J_{\mathrm{w}}(\Delta H_{\mathrm{v}})}{T_{\mathrm{mf,ag}} - T_{\mathrm{film}}}\right]}} = \frac{\left(T_{\mathrm{film}} - T_{\mathrm{p}}\right)}{\frac{1}{h_{\mathrm{film}}}} = \frac{\left(T_{\mathrm{p}} - T_{\mathrm{cp}}\right)}{\frac{\delta_{\mathrm{cp}}}{K_{\mathrm{cp}}}} = \frac{\left(T_{\mathrm{cp}} - T_{\mathrm{bp}}\right)}{\frac{1}{h_{\mathrm{p}}}} \tag{29}$$

$$U_{\mathrm{total,ag}} = \frac{1}{\left[\frac{1}{h_{\mathrm{f}}}\right] + \left[\frac{1}{\left[\frac{1}{\left[\frac{\delta}{K_M}\right] + \left[\frac{\delta_{ag}}{K_{air}}\right]}\right] + \left[\frac{J_w \Delta H_v}{T_{mf,ag} - T_{film}}\right]}\right] + \left[\frac{1}{h_{\mathrm{film}}}\right] + \left[\frac{\delta_{\mathrm{cp}}}{K_{\mathrm{cp}}}\right] + \left[\frac{1}{h_{\mathrm{p}}}\right]} \tag{30}$$

$$T_{\mathrm{mf,ag}} = T_{\mathrm{bf}} - \frac{\left(T_{\mathrm{bf}} - T_{\mathrm{bp}}\right) + J_{\mathrm{w}}(\Delta H_{\mathrm{v}})\left(\frac{K_{\mathrm{M}}}{\delta} + \frac{\delta_{\mathrm{ag}}}{K_{\mathrm{air}}}\right)}{h_{\mathrm{f}}\left(\frac{K_{\mathrm{M}}}{\delta} + \frac{\delta_{\mathrm{ag}}}{K_{\mathrm{air}}} + \frac{1}{h_{\mathrm{p}}} + \frac{1}{h_{\mathrm{f}}}\right)}, \text{ and} \tag{31}$$

$$T_{\mathrm{film}} = T_{\mathrm{bp}} + \frac{\left(T_{\mathrm{bf}} - T_{\mathrm{bp}}\right) + J_{\mathrm{w}}(\Delta H_{\mathrm{v}})\left(\frac{K_{\mathrm{M}}}{\delta} + \frac{\delta_{\mathrm{ag}}}{K_{\mathrm{air}}}\right)}{h_{\mathrm{p}}\left(\frac{K_{\mathrm{M}}}{\delta} + \frac{\delta_{\mathrm{ag}}}{K_{\mathrm{air}}} + \frac{1}{h_{\mathrm{p}}} + \frac{1}{h_{\mathrm{f}}}\right)} \tag{32}$$

U_{total} $(W/(m^2K))$ is the overall heat transfer coefficient based on the bulk feed and permeate temperatures.

The convection heat transfer coefficients in the feed (h_{f}) and permeate (h_{p}) boundary layers are obtained from the following equations:

$$h_{\mathrm{f}} = \frac{\mathrm{Nu}_{\mathrm{f}} k_{\mathrm{f}}}{D_{\mathrm{h}}}, \text{ and} \tag{33}$$

$$h_{\mathrm{p}} = \frac{\mathrm{Nu}_{\mathrm{p}} k_{\mathrm{p}}}{D_{\mathrm{h}}}, \tag{34}$$

where, k_{f} and k_{p} are thermal conductivities of feed and permeate solutions, respectively, D_{h} is the hydraulic diameter of the flow channel, and Nu is the Nusselt number [2,21,80,122,123]. In the MD process, Nu number is almost always estimated through empirical correlations [21,80,88,124]. In the present work, we used those correlations that provided a more satisfactory agreement with the experimental results. The procedure for the calculation of these coefficients is provided in Appendix A and Appendix D. It is worth mentioning that, in our heat transfer model, the forced convection mode is more dominant in the membrane feed and permeate sections over the free convection according to the Grashof number (Gr) calculation (see Appendix C)

2.1.2 Mass Transfer

The vapor permeation through the membrane pores is proportional to the vapor pressure difference across the membrane for DCMD, and the vapor pressure difference across the membrane and air gap for the AGMD system. The general expressions for mass transfer in DCMD and AGMD are given as explained in Eqs. (35) and (36) respectively:

$$J_{\mathrm{w}} = B_{\mathrm{M}}\left(P_{\mathrm{wv,mf}} - P_{\mathrm{wv,mp}}\right), \tag{35}$$

$$J_{\mathrm{w}} = B_{\mathrm{M}}\left(P_{\mathrm{wv,mf,ag}} - P_{\mathrm{wv,film}}\right) \tag{36}$$

where, J_{w} is the mass flux ($\mathrm{kg/(m^2 s)}$), B_{M}, is the total mass transfer coefficient (($\mathrm{kg/(m^2 sPa)}$), $P_{\mathrm{wv,mf}}$, $P_{\mathrm{wv,mp}}$ and $P_{\mathrm{wv,film}}$ (Pa) are the vapor pressures at the feed and permeate sides of the membrane surface and water film respectively [109,122,125–130]. To calculate the vapor pressures ($P_{\mathrm{wv,mf}}$, $P_{\mathrm{wv,mp}}$ and $P_{\mathrm{wv,film}}$), the Antoine equation is used in the following [19,27,88]:

$$P_{\mathrm{wv,mf}} = (\gamma_{\mathrm{wf}}\, x_{\mathrm{wf}}).\ \exp(23.1964 - (\frac{3816.44}{\boldsymbol{T}_{\mathbf{mf}} - 46.13})), \text{ and} \tag{37}$$

$$P_{\mathrm{wv,mp}} = \exp(23.1964 - (\frac{3816.44}{T_{\mathrm{mp}} - 46.13})), \tag{38}$$

$$P_{\mathrm{wv,film}} = \exp(23.1964 - (\frac{3816.44}{\boldsymbol{T}_{\mathbf{film}} - 46.13})) \tag{39}$$

The activity coefficient of water (γ_{wf}) and mole fraction of water (x_{wf}) must be considered in vapor pressure calculation if the feed solution is saline water. The activity coefficient indicates the behavior of substances from the ideal state because of the impurities in the solution, and the mole fraction of water is the ratio of the number of moles of water to the total number of moles present in the solution. For aqueous feed solution containing Sodium Chloride (NaCl), the water activity coefficient is obtained from Eq. (40) [9,27,131]:

$$\gamma_{\mathrm{wf}} = 1 - (0.5x_{\mathrm{NaCl}}) - (10(x_{\mathrm{NaCl}})^2) \tag{40}$$

where, x_{NaCl} is the mole fraction of NaCl in the feed solution.

The total mass transfer coefficient (B_{M}) is calculated based on the flow type that occurs in the membrane pores and the resistances against the mass transfer.

In the MD process, three mechanisms are involved in the control of diffusive mass transfer across the hydrophobic membrane pores, namely: (1) Knudsen flow (2) molecular-diffusion flow and (3) transition mechanism (a combination of the Knudsen and molecular-diffusion flow) [80,126,132]. The type of the mass transfer flow is defined by Knudsen number ($\mathrm{K_n}$) which can be obtained from Eq. (41) and (42).

$$\mathrm{K_n} = \frac{\lambda}{d_{\mathrm{pore}}}\text{, and} \tag{41}$$

$$\lambda = \frac{K_{\mathrm{B}}T_{\mathrm{m}}}{\sqrt{2}\pi P_{\mathrm{m}}\sigma^2} \tag{42}$$

where, d_{pore} is the diameter of membrane pores, λ is the mean free path of the transported molecules, K_{B} is the Boltzmann constant (1.380649×10^{-23} J/K), P_{m} is the mean pressure inside the membrane pores (almost atmospheric pressure) and σ is the collision diameter of water molecules (2.641×10^{-10} m). If $\mathrm{K_n} > 1$, mass transfer through the pores is primarily due to Knudsen flow, where vapor molecules collide more frequently with the pore wall than with each other. If $\mathrm{K_n} < 0.01$, the mass flow through the pores is mainly due to molecular-diffusion, where molecule-molecule collisions are dominant compared to molecule-wall collisions. If $0.01 < \mathrm{K_n} < 1$, the combination of these two types of flows is responsible for mass transfer. Each of these flow types creates resistance against mass transfer through the membrane pores Compared with DCMD, an additional resistance layer is built up against mass transfer due to the presence of stagnant air between the membrane and the coolant plate in the AGMD system based on the molecular diffusion model [118,133]. Therefore, according to the mass transfer resistance model (Figure **2.3**. (b)), based on the flow type inside the membrane pores and stagnant air in the air gap, the total mass transfer coefficient and resistances are calculated by following equations in Table **2.5** and Table **2.6** for DCMD and AGMD systems respectively (Eqs. (43-51)) [21,64,88,131].

$$R_{\mathrm{ag}} = \left[\frac{MW_{\mathrm{w}}PD}{RT_{\mathrm{avg,ag}}\delta_{\mathrm{ag}}P_{\mathrm{air,ag}}}\right]^{-1}, \tag{43}$$

$$R_{\mathrm{K}} = \left[\left(\frac{2\varepsilon r}{3\delta\tau}\right)\cdot\left(\frac{8MW_{\mathrm{w}}}{\pi RT_{\mathrm{avg,m}}}\right)^{0.5}\right]^{-1}, \tag{44}$$

$$R_{\mathrm{m}} = \left[\frac{MW_{\mathrm{w}}\varepsilon PD}{RT_{\mathrm{avg,m}}\delta\tau P_{\mathrm{air,pore}}}\right]^{-1}, \tag{45}$$

Table 2.5. Total mass transfer coefficient (B_M) calculation for DCMD process

$\mathrm{K_n} > 1$	$B_{\mathrm{M}} = (R_{\mathrm{K}})^{(-1)} = \left[\left(\frac{2\varepsilon r}{3\delta\tau}\right)\left(\frac{8MW_w}{\pi RT_{avg,m}}\right)^{0.5}\right],$	(46)
$\mathrm{K_n} < 0.01$	$B_{\mathrm{M}} = (R_{\mathrm{m}})^{(-1)} = \left[\frac{MW_w\varepsilon PD}{RT_{avg,m}\delta\tau P_{air,pore}}\right],$	(47)
$0.01 < \mathrm{K_n} < 1$	$\begin{cases} B_{\mathrm{M}} = (R_{\mathrm{K}} + R_{\mathrm{m}})^{(-1)} \text{ , and} \\ B_M = \left\{\left[\left(\frac{2\varepsilon r}{3\delta\tau}\right)\cdot\left(\frac{8MW_{\mathrm{w}}}{\pi RT_{\mathrm{avg,m}}}\right)^{0.5}\right]^{-1} + \left[\frac{MW_{\mathrm{w}}\varepsilon PD}{RT_{\mathrm{avg,m}}\delta\tau P_{\mathrm{air,pore}}}\right]^{-1}\right\}^{-1}, \end{cases}$	(48)

Table 2.6. Total mass transfer coefficient (B_M) calculation for AGMD process

$\mathrm{K_n} > 1$	$B_{\mathrm{M}} = (R_{\mathrm{K}} + R_{\mathrm{ag}})^{(-1)} = \left\{\left[\left(\frac{2\varepsilon r}{3\delta\tau}\right)\cdot\left(\frac{8MW_{\mathrm{w}}}{\pi R T_{\mathrm{avg,m}}}\right)^{0.5}\right]^{-1} + \left[\frac{MW_{\mathrm{w}}PD}{RT_{\mathrm{avg,ag}}\delta_{\mathrm{ag}}P_{\mathrm{air,ag}}}\right]^{-1}\right\}^{-1},$	(49)
$\mathrm{K_n} < 0.01$	$B_{\mathrm{M}} = (R_{\mathrm{m}} + R_{\mathrm{ag}})^{(-1)} = \left\{\left[\frac{MW_{\mathrm{w}}\varepsilon PD}{RT_{\mathrm{avg,m}}\delta\tau P_{\mathrm{air,pore}}}\right]^{-1} + \left[\frac{MW_{\mathrm{w}}PD}{RT_{\mathrm{avg,ag}}\delta_{\mathrm{ag}}P_{\mathrm{air,ag}}}\right]^{-1}\right\}^{-1},$	(50)
$0.01 < \mathrm{K_n} < 1$	$B_{\mathrm{M}} = (R_{\mathrm{K}} + R_{\mathrm{m}} + R_{\mathrm{ag}})^{(-1)}$, and $B_M = \left\{\left[\left(\frac{2\varepsilon r}{3\delta\tau}\right)\cdot\left(\frac{8MW_{\mathrm{w}}}{\pi R T_{\mathrm{avg,m}}}\right)^{0.5}\right]^{-1} + \left[\frac{MW_{\mathrm{w}}\varepsilon PD}{RT_{\mathrm{av,m}}\delta\tau P_{\mathrm{air,pore}}}\right]^{-1} + \left[\frac{MW_{\mathrm{w}}PD}{RT_{\mathrm{avg,ag}}\delta_{\mathrm{ag}}P_{\mathrm{air,ag}}}\right]^{-1}\right\}^{-1},$	(51)

where, R_{ag} is the resistance against the mass transfer due to stagnant air in the air gap, R_{K} and R_{m} are the resistivities because of the Knudsen and molecular diffusion flow modes through the membrane pores respectively. As can be observed from Eqs. (46 to 51), B_{M} is dependent on the membrane properties such as pore size (*r*), porosity (ε), tortuosity ($\tau = 1/\varepsilon$), membrane thickness (δ), air gap width (δ_{ag}), membrane and air gap average temperatures ($T_{\mathrm{avg,m}} = \frac{T_{\mathrm{mf}}+T_{\mathrm{mp}}}{2}, T_{\mathrm{avg,ag}} = \frac{T_{\mathrm{mp.ag}}+T_{\mathrm{film}}}{2}$)

MW_{w} is the molecular weight of water, *R* is the universal gas constant (8.314 J/(Kmole)), *P* is the total pressure, which is the summation of the partial pressures of air (P_{air}) and water vapor (P_{V}) within the membrane pores or air gap. *D* is the water diffusion coefficient (m^2/s) and the value of *P.D* (Pam^2/s) (Eq. (52)) is obtained based on the average temperature ($T_{\mathrm{avg}} = T_{\mathrm{avg,m}}$ for membrane and $T_{\mathrm{avg}} = T_{\mathrm{avg,ag}}$ for the air gap). $P_{\mathrm{air,pore}}$ is the log mean air pressure in the membrane pores, $P_{\mathrm{air,ag}}$ is the log mean air pressure within the air gap. The procedure for calculating $P_{\mathrm{air,pore}}$ and $P_{\mathrm{air,ag}}$ are described in the following expressions. (P_V is calculated using the Antoine equations based on temperature) [88,101,132] and D^0 is the mass diffusivity between the air and water vapour at standard condition ($24 \times 10^{-6}\ m^2/s$) [13].

$$P.D = 1.895 \times 10^{-5} T_{\text{avg}}^{2.072} , \quad (52)$$

$$D = D^0 \left[\frac{T_{\text{avg}}}{298}\right]^{2.334} , \quad (53)$$

$$P = \frac{PD}{D^0 \left[\frac{T_{\text{avg}}}{298}\right]^{2.334}} , \quad (54)$$

$$P_{\text{air}} = P - P_{\text{V}} , \quad (55)$$

$$P_{\text{air,pore}} = \frac{P_{\text{air,mf}} - P_{\text{air,mp}}}{\log\frac{P_{\text{air,mf}}}{P_{\text{air,mp}}}} \text{, and} \quad (56)$$

$$P_{\text{air,ag}} = \frac{P_{\text{air,mp}} - P_{\text{air,film}}}{\log\frac{P_{\text{air,mp}}}{P_{\text{air,film}}}} , \quad (57)$$

$$P_{\text{air,mf}} = P - P_{\text{v,mf}} , \quad (58)$$

$$P_{\text{air,mp}} = P - P_{\text{v,mp}} , \quad (59)$$

$$P_{\text{air,film}} = P - P_{\text{v,film}} , \quad (60)$$

2.1.3 Temperature and concentration polarization effects

2.1.3.1 Temperature polarization effect

Thermal resistance due to boundary layers adjacent to the feed and permeate sides of the membrane test section creates a temperature gradient between the membrane surface and the bulk fluid (see the temperature profile across the membrane in Figure **2.1**). This phenomenon is called temperature polarization, causing a remarkable reduction in the thermal driving force and thus the permeate flux. To investigate the effect of temperature polarization on the MD performance, the temperature polarization coefficient (TPC) is defined as Eq. (61) for DCMD process and as Eq.(62) for AGMD system [22,27,119,124]

$$TPC = \frac{T_{\text{mf}} - T_{\text{mp}}}{T_{\text{bf}} - T_{\text{bp}}} \quad (61)$$

$$TPC = \frac{T_{\text{mf,ag}} - T_{\text{film}}}{T_{\text{bf}} - T_{\text{bp}}} \quad (62)$$

The smaller the TPC, the more significant the effect of temperature polarization on the performance of MD.

2.1.3.2 Concentration polarization effect

During the MD process, the water vapor molecules pass through the membrane pores, while diffusion of salt ions is hindered. As a result, the salt concentration close to the membrane surface on the feed side increases gradually, resulting in concentration polarization. The concentration polarization results in lower vapor pressure at the feed side, which reduces the overall vapor pressure-based driving force (Eq. (37)) The resistance to mass transfer due to the thickness of the concentration boundary layer and retarded driving force results in lower mass flux. The concentration polarization coefficient (CPC) is estimated by using Eq.(63) [2,21,24,134,135].

$$\mathrm{CPC} = \frac{C_{\mathrm{mf}}}{C_{\mathrm{bf}}}, \text{ and} \tag{63}$$

$$C_{\mathrm{mf}} = C_{\mathrm{bf}}\, e^{\left(\frac{J_{\mathrm{w}}}{\rho_{\mathrm{f}} K}\right)}, \tag{64}$$

where, C_{mf} is the salt concentration on the membrane surface in the feed side, C_{bf} is the bulk salt concentration, and K is the overall mass transfer coefficient of salt ions through the concentration boundary layer at the feed side (See Appendix E) for the procedure to calculate K). The larger the CPC, the more significant the effect of concentration polarization on undermining the performance of MD modules.

2.1.4 Energy efficiency

To understand the energy efficiency of the MD process, the thermal efficiency, and overall energy efficiency of the system are important factors that must be taken into consideration. The fraction of the energy transferring by the vapor molecules through the membrane and air gap is defined as the thermal efficiency of the system, which is explained by Eq. (65) for DCMD and Eq. (66) for AGMD system:

$$\text{Thermal efficiency } (\eta) = \frac{Q_{\mathrm{v}}}{Q_{\mathrm{v}} + Q_{\mathrm{c,m}}} \times 100 \tag{65}$$

$$\text{Thermal efficiency } (\eta) = \frac{Q_\mathrm{v}}{Q_\mathrm{v}+Q_\mathrm{c,M-ag}} \times 100, \text{ and} \tag{66}$$

$$Q_\mathrm{c,M-ag} = \frac{(T_\mathrm{mf,ag} - T_\mathrm{film})}{\frac{\delta}{K_\mathrm{M}} + \frac{\delta_\mathrm{ag}}{K_\mathrm{air}}}, \tag{67}$$

where, $Q_\mathrm{c,m}$ and $Q_\mathrm{c,M-ag}$ are the heat loss from the membrane module to the ambient environment in DCMD and AGMD system respectively. The overall energy efficiency of the MD system is the ratio of heat transferred by the vapor molecules through the membrane test section to the energy that is consumed for heating the feed solution, which is evaluated by the gained output ratio (GOR, Eq. (68)) [88,89,119]. Q_H is the energy consumption for heating the feed solution.

$$\mathrm{GOR} = \frac{Q_\mathrm{v}}{Q_\mathrm{H}} \tag{68}$$

2.2 A mathematical model based on the Effectiveness-NTU (∈-NTU) method

The temperature distribution on the membrane surface may be determined by using a finite difference method based on the Effectiveness-Number of Transfer Units (∈-NTU) model by considering the temperature variation over the membrane thickness and along the fluid channels. The novelty of this work is mainly related to the use of ∈-NTU method for analyzing heat and mass transfer in the MD system. The heat exchanger analogy allows modeling of membrane distillation using non-dimensional parameters from counter/parallel-flow heat exchangers, such as effectiveness (∈) and the number of transfer units (NTU). ∈ reflects the ratio of the actual heat transfer rate for a heat exchanger to the maximum possible heat transfer rate, and NTU shows heat transfer capability [136,137]. Since the parameters at the outlet of cold and hot streams are not determined, a calculation based on ∈-NTU method enables precise prediction of the outlet properties as well as temperature profile. It should be noted that the ∈-NTU method, developed by Kays and London [136,137], does not take into consideration phase change effects, while in the MD process, the mass transfer and vaporization occure.

However the permeat flow arte is about three order of magnitudes smaller than the flow rate of feed and cold stream. Therefore, ∈-NTU method can be used for the MD process. To simulate the heat and mass transfer in the MD process more accurately, the temperature variation both across the membrane thickness and along the cell channel is considered. Moreover, fluid properties, such as specific heat capacity, might change as a result of temperature variations, and thus the overall heat transfer coefficient might be influenced by the variation of fluid properties and flow conditions. Although the finite-difference method can accurately predict the heat and mass transfer, it may require a longer time to solve the problem. Besides, this method is independent of the geometry, membrane area, and flow pattern (parallel flow, counter-flow, cross-flow, etc.) [138]. On the other hand, by using ∈-NTU method, the details of each node cannot be specified. ∈-NTU method relies on the average values of temperature and other properties, where the temperature distribution in two dimensions is neglected, leading to less accurate results. Therefore, in the present work, we combined finite-difference and ∈-NTU methods to comprehensively solve the heat and mass transfer in the MD system. Such an integrated method enables simulating the MD process with reasonable accuracy and a low computational burden. Also, the ∈-NTU method helps us to simulate the heat and mass transfer without the need to measure some experimental data such as outlet temperatures of streams.

The assumptions for the modeling are as follows: (1) steady-state conditions (2) the heat loss from the combination of membrane module and flow systems to the ambient environment is negligible since our experimental test setup is sufficiently insulated to reduce heat loss to the environment. (3) The transmembrane pressure is zero because the driving force in the MD process is the temperature gradient. (4) The effect of viscous flow on the mass transfer through the membrane pores can be disregarded, which is justified by considering the presence of air inside the membrane pores and zero pressure difference across the membrane. (5) Membrane pores are assumed to be uniform cylindrical channels. Moreover, for the modeling of AGMD process, the following assumptions are added: (6) constant pressure inside the air gap, (7) stagnant air within the membrane pores, (8) and a film-wise of water condensation is considered on the cooling plate surface in the air gap. Moreover, (9) diffusion and conduction are assumed to be responsible for mass and heat transfer respectively within the air gap.

2.2.1 Mathematical Algorithm

The mathematical algorithms for the prediction of DCMD and AGMD performance are illustrated in Figure **2.5** and Figure **2.6** respectively. MATLAB programming software was used for coding and modeling. The modeling inputs are categorized into four groups:

(i) membrane properties such as thickness (δ), porosity (ε), pore size (d_p), tortuosity (τ), thermal conductivity (K_m), and an active area of the membrane (A), air gap properties including the width of the air gap and thermal conductivity of stagnant air, cooling plate properties (thickness and thermal conductivity),

(ii) physical properties of fluids (feed and permeate streams) including C_p, thermal conductivity, μ, and ρ (Appendix. A),

(iii) module geometry (length and width of the flow channel and D_h), and

(iv) operating conditions for the experiments: bulk temperatures ($T_\mathrm{bf}, T_\mathrm{bp}$), flow rates and the salt concentration in the feed solution (S_f).

The outputs include permeation flux, heat transfer rates, temperature and concentration polarization effects, temperature profile over the membrane surface and across the membrane, and energy efficiency of the MD system. The modeling procedure of DCMD and AGMD systems is illustrated in Figure **2.5** and Figure **2.6** respectively.

First, the fluid velocity, Reynolds (Re), Prandtl (Pr), and Nusslet (Nu) numbers, as well as heat transfer coefficients ($h_\mathrm{f}, h_\mathrm{p}$) were calculated based on the input values and feed and permeate bulk temperatures. We assumed that the inlet temperature of feed and permeate streams are the same as the bulk temperatures ($T_{h,in} = T_{f,in} = T_{bf}$ and $T_{c,in} = T_{p,in} = T_{bp}$). Then, the outlet temperatures ($T_{f,out}$ and $T_{p,out}$) were determined using the $\in -$NTU method for a counter-current MD process based on the equations in Table **2.7**. In the next step, the membrane surface was divided into a finite number of elements, and the temperature profile along the membrane surface was calculated (Figure **2.4**). In the main loop, the estimated outlet permeate temperature from the previous step ($T_{p,out}$) was used as the only initial guess for the inlet temperature of the permeate stream for the first element, and the parallel flow pattern was considered for continuing the calculations. Then, the iterative procedure was used to find the final membrane surface temperatures (T_{mf} & T_{mp}) and water film temperature (T_{film}). Finally, based on $\in -$NTU method for parallel flow (See Appendix F for more details), the outlet temperatures for each element were calculated, and this iteration was continued until the outlet permeate temperature for the last element (N) became equal to the main inlet permeate temperature. Finally, when the iteration converged, permeate flux, energy efficiency, TPC, CPC, and thermal efficiency were calculated.

Table 2.7. Equations for calculating outlet temperature using ∈-NTU method.

$$C_c = \dot{m}_c c_{p,c}\ , \tag{69-a}$$

$$C_h = \dot{m}_h c_{p,h}, \tag{69-b}$$

$$C_{min} = Min(C_h, C_c), \tag{70-a}$$

$$C_{max} = Max(C_h, C_c), \tag{70-b}$$

$$NTU = U.(membrane\ area)/C_{\min}, \tag{71}$$

$$C_{\mathrm{r}} = \frac{C_{\min}}{C_{\max}}, \tag{72}$$

$$\text{If } \ C_{\mathrm{r}} = 1\text{:} \ \in = \frac{NTU}{1+NTU}, \tag{73-a}$$

$$\text{If } \ C_{\mathrm{r}} < 1\ \text{:} \ \in = \frac{1-\exp\left(-NTU(1-C_{\mathrm{r}})\right)}{1-C_{\mathrm{r}}\exp\left(-NTU(1-C_{\mathrm{r}})\right)} \tag{73-b}$$

$$\in = \frac{Q}{Q_{\max}}\ , \tag{74}$$

$$Q = C_{\mathrm{c}}\ (T_{\mathrm{c,out}} - T_{\mathrm{c,in}}), \tag{75}$$

$$Q_{\max} = C_{\min}(T_{\mathrm{h,in}} - T_{\mathrm{c,in}}), \tag{76}$$

$$T_{h,out} = T_{f,out} = \ T_{h,in} - ((T_{c,out} - T_{c,in})/C_r), \text{ and} \tag{77}$$

$$T_{c,out} = T_{p,out} = \ T_{c,in} + Q/C_c \tag{78}$$

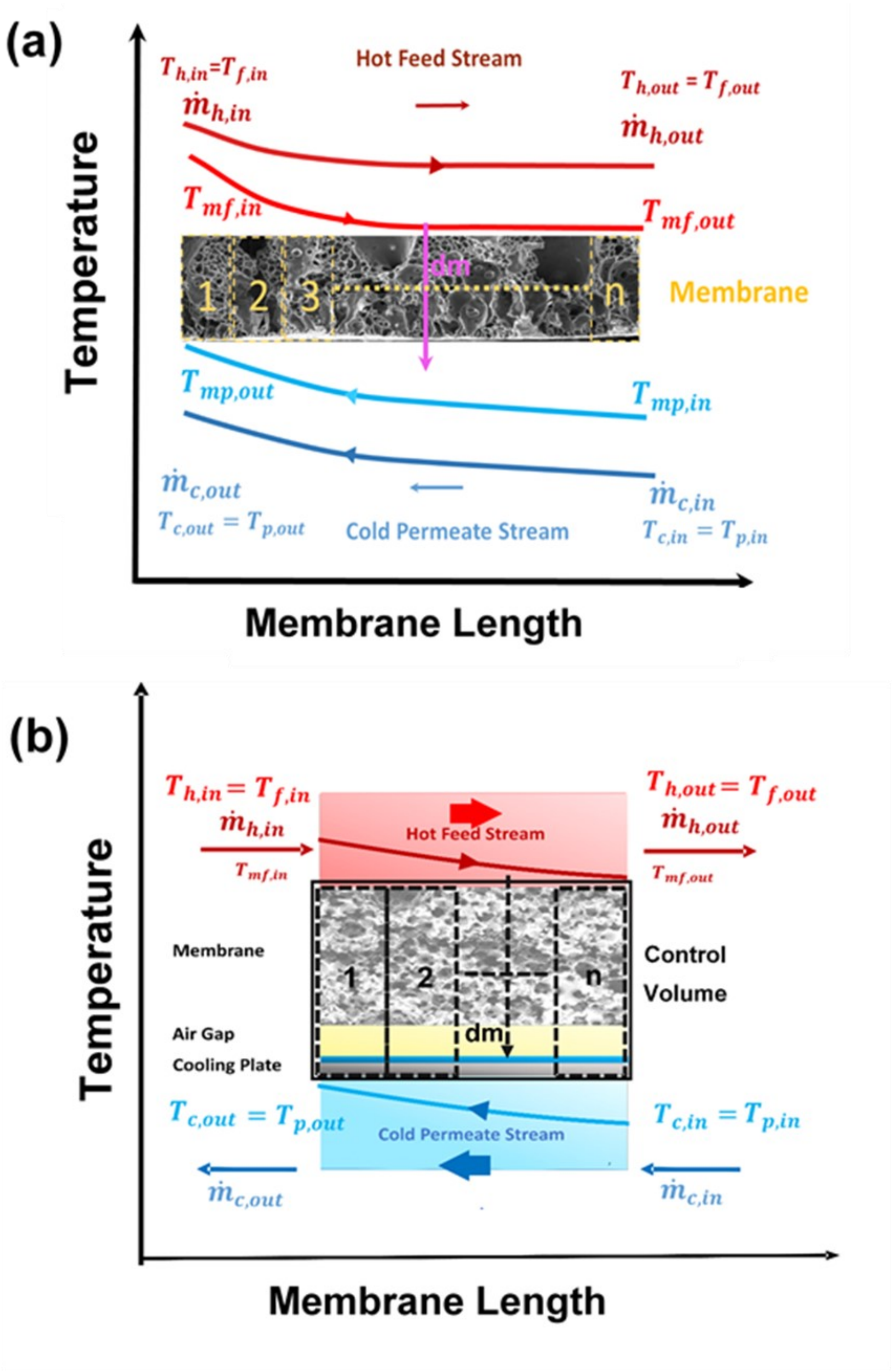

Figure 2.4. Temperature distribution over the membrane surface in the counter-current flow model and dividing membrane into the number of elements. (a) DCMD, (b) AGMD

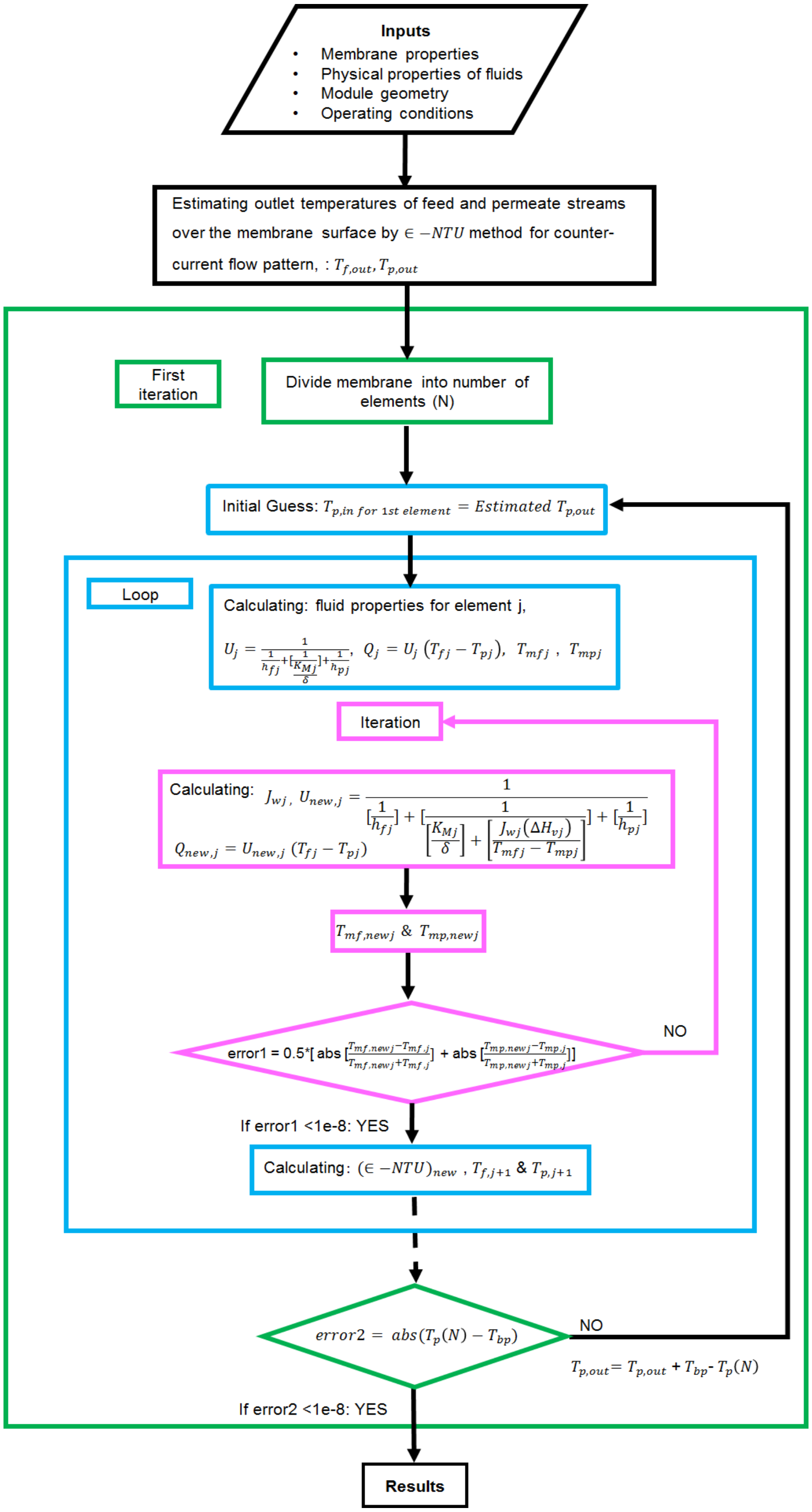

Figure 2.5. The developed mathematical algorithm to predict the DCMD performance by MATLAB software.

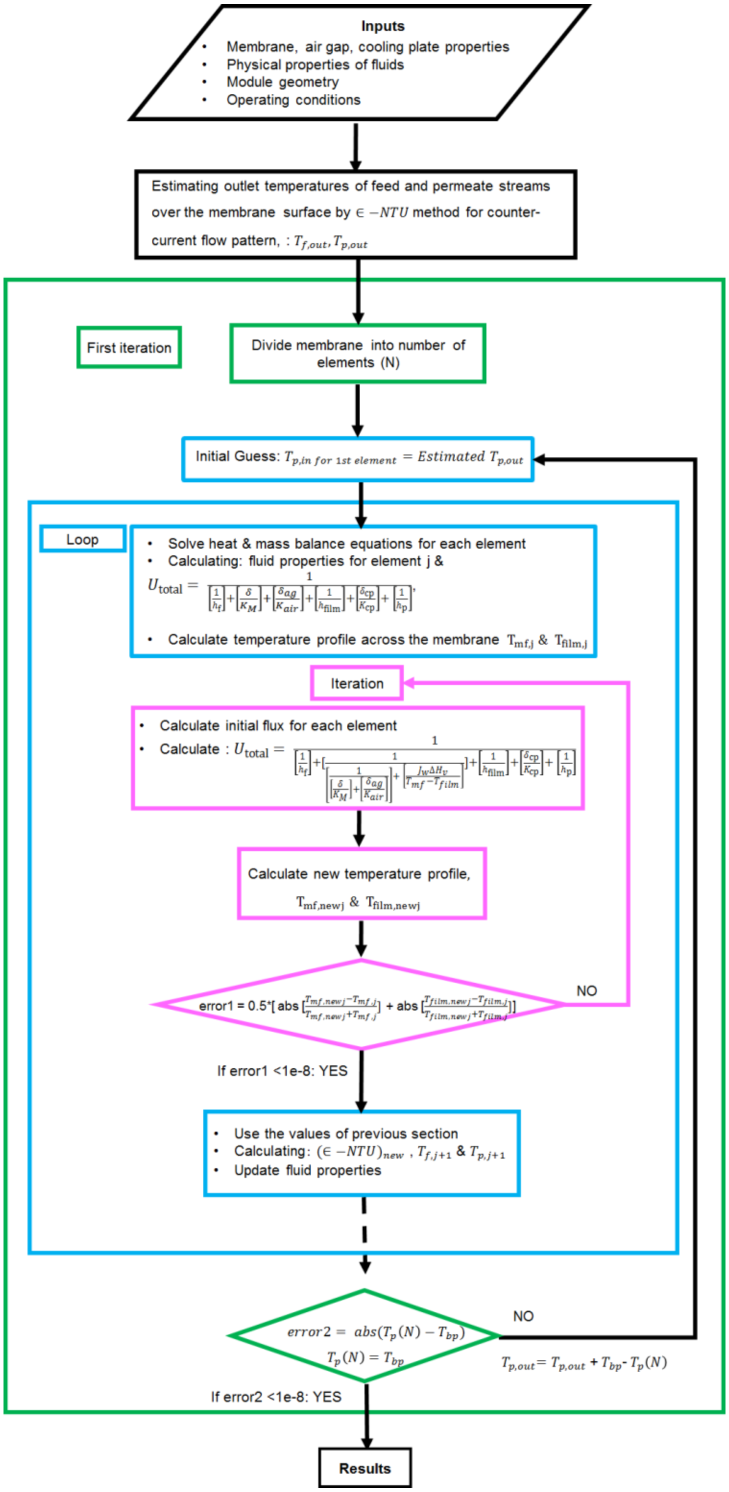

Figure 2.6. The developed mathematical algorithm to predict AGMD performance by MATLAB software

2.3 Experimental work

2.3.1 DCMD setup

The DCMD flow diagram is shown in Figure **2.7**(a). The major parts of the test facility are the test module (Figure **2.7**(b)), hot feed solution, and cold permeate solution loops. The temperatures in the feed and permeate loops were controlled through two external thermal baths, and the solutions were circulated by two pumps. All parameters, such as temperature in tanks, flow rates, pressure, and conductivity of the feed and permeate solutions, were monitored by inline sensors throughout the experiments. The test setup was sufficiently insulated to reduce heat loss to the ambient environment. As can be seen in Figure **2.7**(b), the membrane is placed between two insulated compartments. The feed stream enters the cell in the perpendicular direction and flows along the membrane surface. Vertical flow from bottom to top prevents the accumulation of air bubbles on the membrane surface. The air bubble accumulation over the membrane surface decreases the active area of the membrane exposed to the feed stream and thus leads to a reduction in the permeate flux. The permeate stream is circulated through the other compartment of the membrane cell in the opposite direction with the feed solution flow (counter-current mode).

2.3.2 AGMD setup

The experimental setup and the flow diagram for the AGMD system are schematically illustrated in Figure **2.8**. The main objects of the setup facility are similar to DCMD setup including the membrane cell module, hot feed, and cold permeate solution loops. The feed and permeate streams were circulated by two pumps with adjustable flow rates. Thermal baths were used to heat the feed solution and keep the temperatures in two permeate and feed tanks at constant and desired temperatures during the experiment. Also, all parameters such as temperature in tanks, flow rates, pressure, and conductivity of the feed and permeate solutions were monitored by inline sensors in the experiment and the membrane was placed between two insulated compartments in the membrane cell. As can be seen from Figure **2.8**, the feed stream is connected to the heating system, then, the hot saline solution is brought into direct contact with the membrane surface, in the feed side inside the membrane module, while at the permeate side, there is an air gap which is in contact with an aluminum coolant plate. The thickness for the air gap and coolant plate was 5.6 mm and 1.4 mm, respectively and the effective area of membrane was 140 cm^2. Besides, the membrane test section was insulated to reduce the heat loss to the ambient environment and the experiments were functioned in counter-current flow mode.

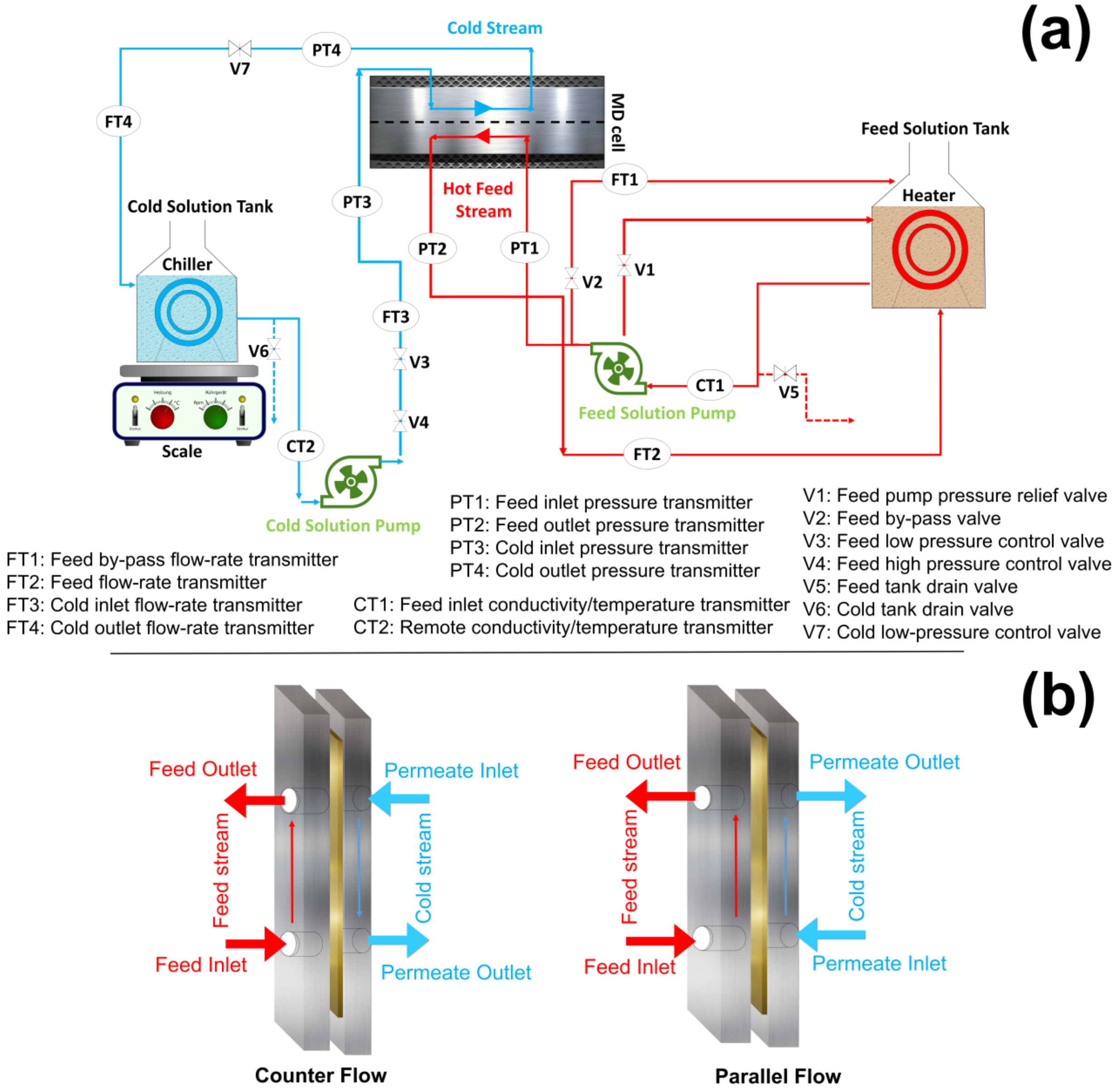

Figure 2.7. (a) The flow diagram of the DCMD unit that was used for conducting experiments and (b) two different flow modes for feed and permeate streams.

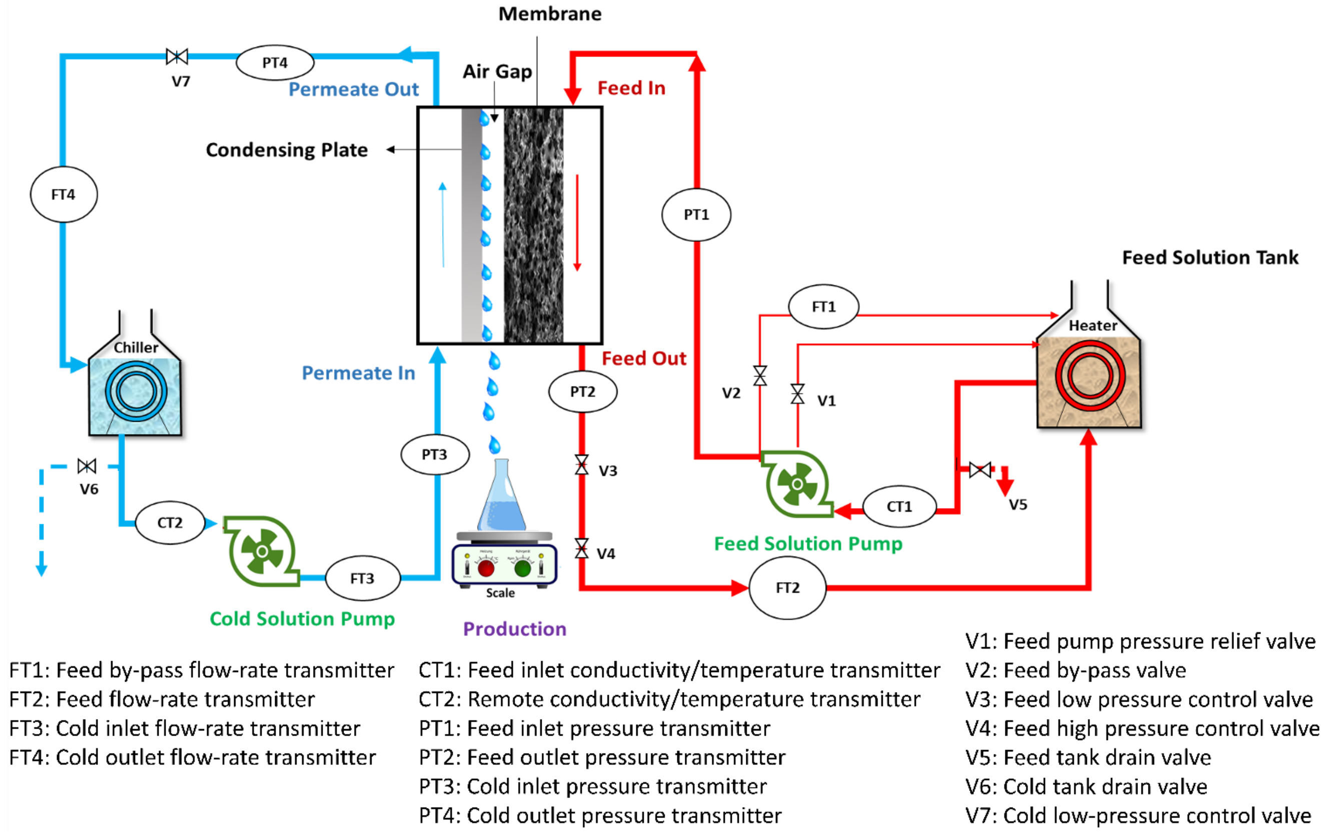

Figure 2.8. The schematic of (a) experimental setup (Sterlitech, Kent, USA) and (b) the flow diagram for the AGMD system

Two different kinds of commercial hydrophobic membranes, namely polytetrafluoroethylene (PTFE) and polyvinylidene difluoride (PVDF) (Sterlitech, Kent, USA) were used to evaluate the effect of membrane properties on MD performance. The structural and contact angle properties of these membranes are presented in Table **2.8** and Table G.1 in Appendix G, respectively.

Table 2.8. The structural properties of the membranes used in the DCMD experiments.

Membrane	Pore size (µm)	Water Contact Angle (°)	Thickness (µm)	Porosity (%)
PTFE	0.1	138°	160	72
PTFE	0.2	135.5°	100	81
PTFE	0.45	123°	100	83.23
PVDF	0.3	95°	150	80

To investigate the effect of different parameters on the MD performance, a series of MD experiments were conducted on the treatment of aqueous salt solutions (NaCl, 35 gr/L). Two important parameters to assess the performance of the DCMD process are water flux and salt rejection. The salt rejection was obtained by the following equation.

$$Rejection = \frac{C_{\text{feed}} - C_{\text{permeate}}}{C_{\text{feed}}} \times 100, \tag{79}$$

where C_{permeate} and C_{feed} are the concentrations of dissolved salts in permeate and feed solutions, respectively, which were calculated based on the conductivity measurement of solutions. A digital weight balance (Sterlitech, Kent, USA) was placed under the permeate tank to measure the mass increment (Δm) over the experimental time (*t*) for the DCMD system, but for AGMD, a weight scale (Mettler Toledo) was used to measure the mass of permeate during the experiment. The precision of the digital weight balance was ±5 gr for the DCMD process. The water flux was calculated as follows, with

$$permeate\ flux = \frac{\Delta m}{At}\left[\frac{kg}{m^2 hr}\right], \tag{80}$$

where *A* is the surface area of the membrane which is in contact with hot feed solution. The uncertainty analysis for measuring mass flux during the experiment is explained in Appendix H.

Chapter 3

3 Direct contact membrane distillation modeling[1]

3.1 Introduction

Mathematical modeling of the MD process enables a deeper understanding and prediction of the impact of effective parameters on the performance of MD in terms of permeate flux, rejection, and energy consumption. It also sets a strong framework for the optimization of the MD process by identifying process parameters and ideal membrane properties that lead to cost- and energy-efficient water desalination. Quantitative comparison of different MD scenarios provides valuable insight into the fabrication of innovative membranes, as well as smart adjustment of process parameters to diminish the adverse effect of the obstacles in the MD process mentioned in chapter 1. So far, several mathematical models have been developed and reported for the MD process [19,21,89,109,121,122,125,127]. Ali et al. studied the effect of hydrodynamic and thermal conditions on heat and mass transport phenomena in direct contact membrane distillation (DCMD) to analyze the temperature polarization effect. By installing many sensors on the membrane surface, the impact of the feed temperature on the temperature polarization phenomenon was analyzed and compared with theoretical calculations [86]. Winter, [19] investigated the role of material properties of the membrane, backing structures, and gap spacers in different configurations of the MD process on permeate flux and thermal efficiency. Furthermore, the process sensitivity to operational parameters such as temperature, flow rate, and salinity was assessed. Khalifa et al. evaluated the effect of different operating parameters, such as feed temperature, fluid velocity, and salt concentration, on permeate flux solving mass and heat transfer equations [9]. Although extensive research has been carried out on the modeling of the MD process, most of the developed models were one-dimensional [86–88,125,139], or relied on some experimentally determined parameters that made the simulation depend upon a specific

---

[1] The material presented in this chapter has been submitted as a research paper to the journal of Desalination.

experimental condition [86,88]. Experimental measurement of all involved parameters, particularly for larger-scale systems, is not practically feasible and requires expensive instrumentation to record and monitor the parameters associated with the MD performance. Besides, some theoretical studies required many assumptions [83,85–88,122,140] or suffered from a high computational burden; e.g., the CFD modeling works [86,102,103,109]. Finally, in most of the previous studies, the permeate flux was evaluated as the primary response variable, and other important factors, including module design, membrane characteristics, and operating conditions, were disregarded [40,62,121,122,127]. For example, energy efficiency, as a significant component of the MD process deployment, has not been included in most of the earlier theoretical and experimental studies. The interactive effects of influential factors in the MD process were also missed due to a lack of sensitivity analysis. The main goal of this study is to address these research gaps by developing a self-sustained two-dimensional model for simulating heat and mass transfer in the DCMD process.

Here, in this study, a novel, self-sustained 2D mathematical model was developed to analyze DCMD performance based on combining the finite difference and Effectiveness-Number of Transfer Units ($\in -$NTU) methods. The objective is to find the optimum design parameters for a direct contact membrane distillation (DCMD) system. Our model is able to predict the temperature and vapor pressure profiles on the membrane surface. With such valuable information, the permeate flux and thermal efficiency of the DCMD system can be calculated without the need to utilize any parameter obtained from experimentation. The modeling algorithm is described in detail, and sensitivity analysis was conducted based on the membrane properties and operating conditions. The model was validated by comparing its predictions with experimental results for two different membranes over a wide range of operating conditions. The results showed that the feed temperature, membrane porosity, pore size, and thickness are the most dominant factors in the MD system. In addition, the influence of temperature and concentration polarizations on the performance of DCMD and energy efficiency were investigated. Guidelines to achieve higher energy efficiency are provided. The details of mathematical modeling for DCMD system was explained in chapter 2. The results and discussion of theoretical and experimental studies for the DCMD process are presented in the following section.

3.2 Results and Discussion

In this section, the results of our developed mathematical model are first validated with experimental results. Then, the effect of each design parameter on the performance of a DCMD system, in terms of permeate flux, thermal efficiency, GOR, TPC, and CPC, are analyzed using the modeling results. Finally, a design map for the optimum performance of a DCMD system based on effective parameters is presented.

3.2.1 Effect of operating conditions on DCMD performance

3.2.1.1 Feed Temperature

The effect of feed temperature on the permeate flux for both modeling and experiments is depicted in Figure **3.1** (a). As can be seen, the predictions from the theoretical model were in good agreement with the experimentally measured values at different temperatures ($\sim 10\%$ deviation). Besides, by increasing the feed temperature, the permeate flux increased significantly. A 60% increase in feed temperature (from 50℃ to 80℃), led to 181% increment in the permeate flux (from 12.65 to 35.59 $\mathrm{kg/(m^2hr)}$). The higher the feed temperature, the larger the vapor pressure gradient across the membrane (Eqs. (37) and (38)), which resulted in a higher driving force for water transport. Moreover, increasing the feed temperature from 50℃ to 80℃ resulted in about a 20% increase in both GOR value (from 0.65 to 0.78) and thermal efficiency (from 67.82% to 81.17%), as can be observed from Figure **3.1** (b). Because based on Eqs. (20), (35), (65) and (68), higher feed temperature led to higher permeate flux and Q_v, which consequently caused higher GOR and thermal efficiency to be achieved. Figure **3.1** (c) demonstrates the effect of feed temperature on TPC and CPC. The TPC represents the thermal variation that exists between the membrane surface and the bulk solution. Based on Eq. (61), the maximum temperature difference between the two sides of the membranes is achieved when the TPC value approaches 1. According to Figure **3.1** (c) and Table **3.1**, as feed temperature becomes larger, the surface temperatures at both sides of the membrane increased as well, according to Eqs. (26) and (27). As a result, the temperature difference between the two sides of the membrane increased less significantly than the bulk temperature difference, which consequently lowered down the TPC value. By increasing the feed temperature from 50℃ to 80℃, the TPC reduced by 33.2% (from 0.374 to 0.250). Furthermore, by increasing the feed temperature, the permeate flux increased, and higher salt concentration on the membrane surface was created, leading to higher CPC value (from 1.118 to 1.350), based on Eq. (63).

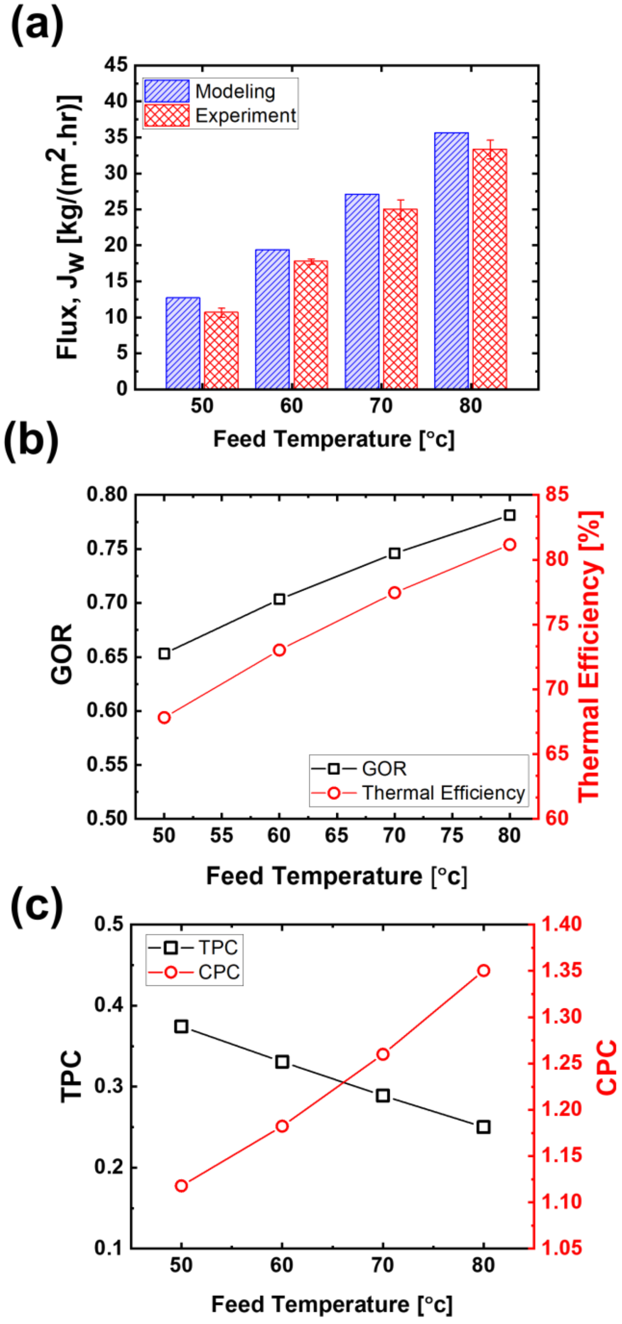

Figure 3.1. DCMD performance based on different feed temperature a) modeling and experimental results for permeate flux b) GOR & thermal efficiency c) TPC & CPC. For all, 35 gr/L NaCl was used in the feed solution, and permeate temperature was kept at 20 °C. Both streams had flow rates of 0.5 LPM, and PTFE (0.45 μm) was used as a m

Table 3.1. Calculated membrane surface temperatures based on different bulk temperatures

T_{bf} (℃)	T_{bp} (℃)	ΔT_{bulk} (℃)	T_{mf} (℃)	T_{mp} (℃)	$\Delta T_{membrane\ surface}$ (℃)
50	20	30	39.79	28.38	11.41
60	20	40	45.47	31.89	13.57
70	20	50	50.70	35.70	15.00
80	20	60	55.52	39.73	15.79

3.2.1.2 Feed and permeate flow rates

The influence of the feed and permeate flow rates on the water flux is presented in Figure **3.2**(a). The modeling results were found to align well with the experimental results. Higher flow rates, or larger Reynolds number, resulted in lower heat transfer resistances ($1/h_{\text{i}}$) and lower thickness of the thermal boundary layer, which eventually led to a higher membrane surface temperature and larger water flux, according to Eqs. 24-27,33, 34, Antoine Equations, and the results are shown in Table **3.2**. It is worth mentioning that the effect of flow rate on permeate flux was not as significant as that of feed temperature. As can be observed from Figure **3.2** (a), increasing the flow rates by 300% (from 0.2 to 0.8 LPM), enhanced the permeate flux by 51.45% (from 20.31 to 30.76 $\text{kg}/(\text{m}^2\text{hr})$), while 60% increment in feed temperature led to a 181% increase in permeate flux. Moreover, by increasing the circulation velocity, the water flux seemed to reach the maximum values asymptotically. The reason can be the reduction of thermal boundary layer thickness, which might have decreased as a result of the increase in the circulation velocity until it reached a plateau. After this threshold, the permeate flux did not change significantly [45,109,136,141].

Figure **3.2** (b) shows that higher flow rates resulted in larger GOR values. Based on Eq. (20), Q_v directly relates the permeate flux and the enthalpy of vaporization (ΔH_v). Permeate flux was higher for larger flow rates, as described earlier. Moreover, due to higher convection heat transfer coefficients at larger flow rates, the surface temperatures approached the bulk temperatures of the fluids, boosting ΔH_v value. Besides, at higher flow rates, the residence time for heat exchange between hot and cold fluids decreased, which consequently reduced the temperature difference between the outlets of feed and permeate streams with the inlet temperatures (Table **3.2**). Hence, the ΔT in heat exchanger decreased at larger flow rates. On the other hand, at higher flow rates, Q_H on the denominator become larger, which offset the rising effect of Q_v on GOR (Eq. 68). Nevertheless, increment in flow rates from 0.2 to 0.8 LPM increased the GOR slightly from 0.7421 to 0.7476 (only 0.74%). Figure **3.2** (b) also shows the negligible effect of the flow rate on the thermal efficiency of the MD process. This can be again attributed to the less effective influence of feed and permeate flow rates on water flux. However, as can be observed in Figure **3.2** (c), increasing the flow rates from 0.2 to 0.8 LPM had a positive impact on the TPC with a 47.5% increment (from 0.221 to 0.326). Higher heat transfer coefficients at larger flow rates caused surface temperatures to be nearly equal to the bulk temperatures of the fluids (see Table **3.2**). Since CPC is mainly affected by water flux, the change in flow rates did not cause a significant variation in the CPC value.

Table 3.2. Influence of different flow rates on membrane surface temperatures and heat transfer coefficients, for PTFE 0.45-micron membrane and counter-current flow direction.

Flow rate (LPM)	$\mathbf{h_f}$ $(\frac{W}{m^2K})$	$\mathbf{h_p}$ $(\frac{W}{m^2K})$	$\mathbf{T_{h,in}}$ (℃)	$\mathbf{T_{h,out}}$ (℃)	$\mathbf{T_{c,in}}$ (℃)	$\mathbf{T_{c,out}}$ (℃)	$\mathbf{T_{mf}}$ (℃)	$\mathbf{T_{mp}}$ (℃)
0.2	1119.4	1158.4	70	64.13	20	25.66	47.79	35.88
0.5	1517.4	1569.7	70	66.88	20	23.00	50.70	35.70
0.8	1774	1834.9	70	67.79	20	22.13	52.01	35.29

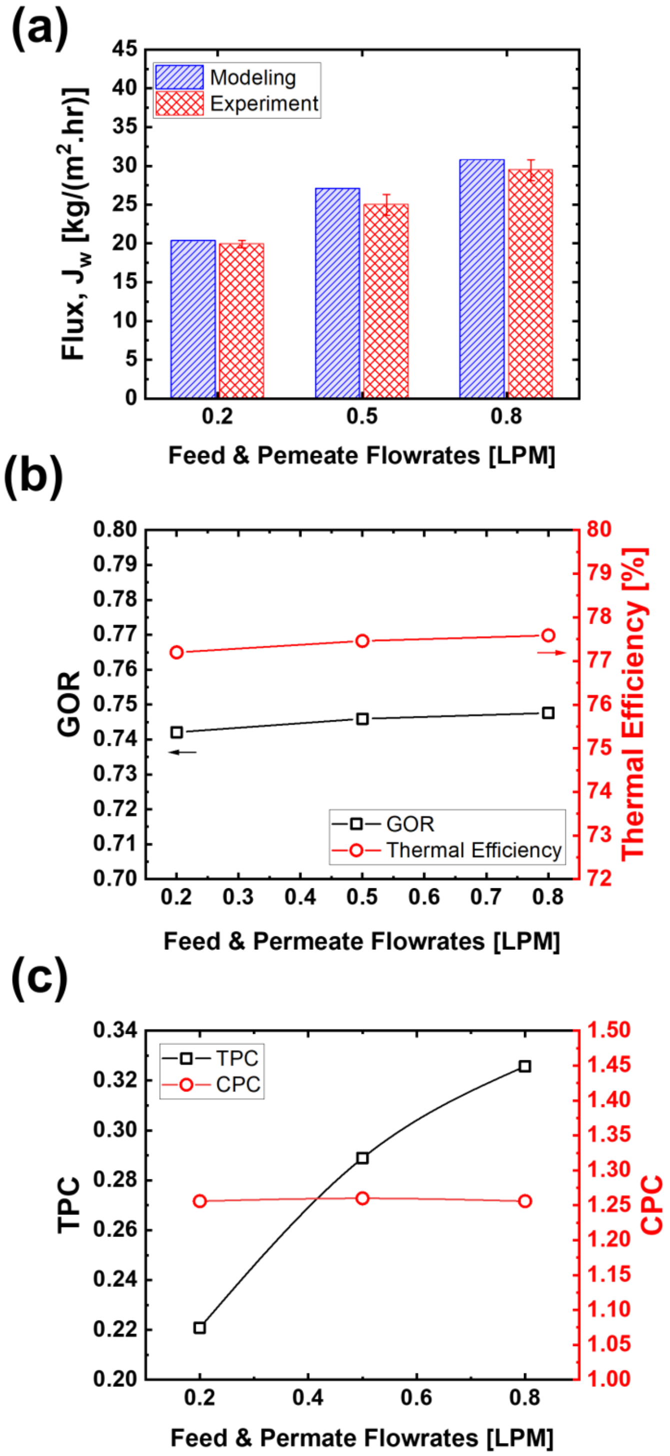

Figure 3.2. DCMD performance based on different feed & permeate flow rates a) modeling and experimental results for permeate flux b) GOR & thermal efficiency c) TPC & CPC. For all, 35 gr/L NaCl was used in the feed solution. Feed and permeate temperatures were kept at 70 ℃ and 20 ℃, respectively. PTFE (0.45 μm) was used as a membrane.

3.2.2 Effect of membrane properties on DCMD performance

3.2.2.1 Membrane pore size

To explore the effect of membrane pore size on the permeate flux, three commercial PTFE membranes with different pores sizes (0.1, 0.2, and 0.45 micron) were tested. According to Figure **3.3** (a), the maximum deviation between theoretical and experimental results obtained for the PTFE with the lowest pore size (0.1 μm). For 0.1 μm pore size, the calculated Knudsen number by modeling was more than 1, and the flow type was assumed to be Knudsen flow (Equations 46-48), which caused a higher mass transfer coefficient (B_{M}) and as a result, higher predicted water flux by the modeling. However, the pores of the PTFE membrane were not uniformly distributed, thereby a combination form of Knudsen and molecular diffusion flow types could have occurred, leading to a lower water flux in the experiment and a large deviation between the experimental results and mathematical calculations.

In order to find the actual contribution of pore size on the performance of the MD process, numerical modeling was utilized. Based on the theoretical results for membranes having different pore sizes, the permeate flux increased by increasing the pore size, mainly due to reduced resistance to mass transfer. Based on Figure **3.3** (a), permeate flux increased by increasing the pore size, mainly due to reduced resistance to mass transfer. The PTFE membrane with a pore size of 0.45 μm showed 27.06 $(\mathrm{kg/(m^2hr)})$ permeate flux, with 38.3% and 13.8% increments compared to water fluxes delivered by 0.1 μm and 0.2 μm pore size membranes, respectively. Our results indicated that membranes with larger pore sizes provide better performance regarding permeate flux. However, MD membranes with larger pore sizes are more prone to pore wetting and thus may completely fail during the filtration process due to the significant reduction in salt rejection. Therefore, the trade-off relation between permeate flux and rejection must be taken into account for selecting a membrane with optimum pore size.

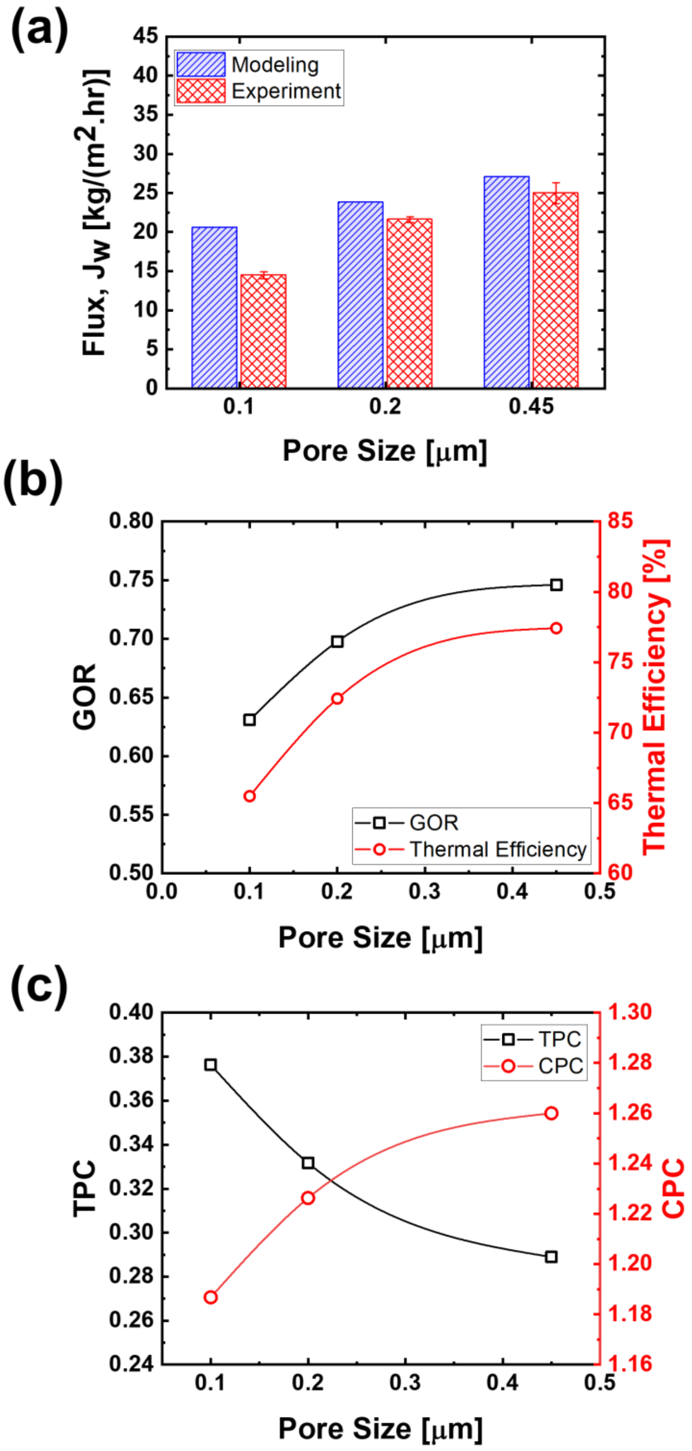

Figure 3.3 .DCMD performance based on different pore sizes a) modeling and experimental results for permeate flux b) GOR & thermal efficiency c) TPC & CPC. For all, 35 gr/L NaCl was used in the feed solution. Feed and permeate temperatures were kept at 70 ℃ and 20 ℃, respectively, and flow rates were adjusted at 0.5 LPM. For (b) and (c), the thickness and porosity of membranes are assumed to be the same with 100 μm and 83%, respectively.

The effect of pore size on GOR and thermal efficiency values are presented in Figure **3.3** (b). Increasing the pore size from 0.1 to 0.45 micron elevated both GOR and thermal efficiency by almost 20%, primarily due to enhancement of water flux (Eqs. (20), (65), and (68)). Furthermore, the TPC showed a 25% reduction because the surface temperature difference between two sides of the membrane reduced more significantly at larger pore size, as can be observed from Table **3.3**. Figure **3.3** (c) shows that pore size increment only caused a 6% increment in CPC due to higher permeate fluxes for larger pore sizes.

Table 3.3. Variation of membrane surface temperatures in the membranes having different pore sizes.

d_p (μm)	T_{bf} (℃)	T_{bp} (℃)	ΔT_{bulk} (℃)	T_{mf} (℃)	T_{mp} (℃)	$\Delta T_{membrane\ surface}$ (℃)
0.1	70	20	50	54.40	35.06	19.34
0.2	70	20	50	53.00	36.41	16.59
0.45	70	20	50	51.91	37.46	14.45

3.2.2.2 Membrane porosity

According to Figure **3.4** (a), by increasing the porosity from 70% to 85%, the permeate flux increased 30% (from 21.7 to 27.9 (kg/(m^{2}h)). Figure **3.4** (b) & (c) show that GOR, thermal efficiency, and CPC increased 20.8%, 20.7%, and 6.4%, respectively. When the membrane porosity enhances, a higher membrane permeability (B_{M}) could be obtained based on Eqs. (46-48). Higher permeate flux and Q_v could be translated into larger GOR, thermal efficiency, and CPC. However, by 21.4% increase in porosity, the TPC decreased by 12.24%, owing to the slight variation of membrane surface temperatures with porosity, as shown in Table **3.4**.

3.2.2.3 Membrane thickness

The effect of membrane thickness on the MD performance is studied in this section. As illustrated in Figure **3.5** (a-c), by increasing the membrane thickness from 50 to 550 μm, the permeate flux and CPC declined 148% (from 31.25 to 12.56 (kg/(m^{2}hr)) and 16% (from 1.30 to 1.12), respectively. However, thickness increment resulted in 2.1%, 2.7%, and 74.4% enhancements in GOR, thermal efficiency, and TPC, respectively. Higher membrane thickness caused more resistance against mass and heat transfers, which resulted in a lower permeate flux and heat loss, thereby higher thermal efficiency and GOR could be achieved. Moreover, because of lower heat loss, the surface temperatures of the membrane were closer to the bulk temperatures, which led to a higher TPC. Given that, an optimum membrane thickness should be adopted for the best performance of the MD system. In general, the effect of membrane thickness on permeate flux was found to be more significant than energy efficiency in the DCMD system.

Table 3.4. Membrane surface temperatures based on different membrane porosity

ε (%)	T_{bf} (℃)	T_{bp} (℃)	ΔT_{bulk} (℃)	T_{mf} (℃)	T_{mp} (℃)	$\Delta T_{membrane\ surface}$ (℃)
70	70	20	50	52.80	36.60	16.19
75	70	20	50	52.47	36.92	15.56
80	70	20	50	52.13	37.25	14.89
85	70	20	50	51.78	37.58	14.20

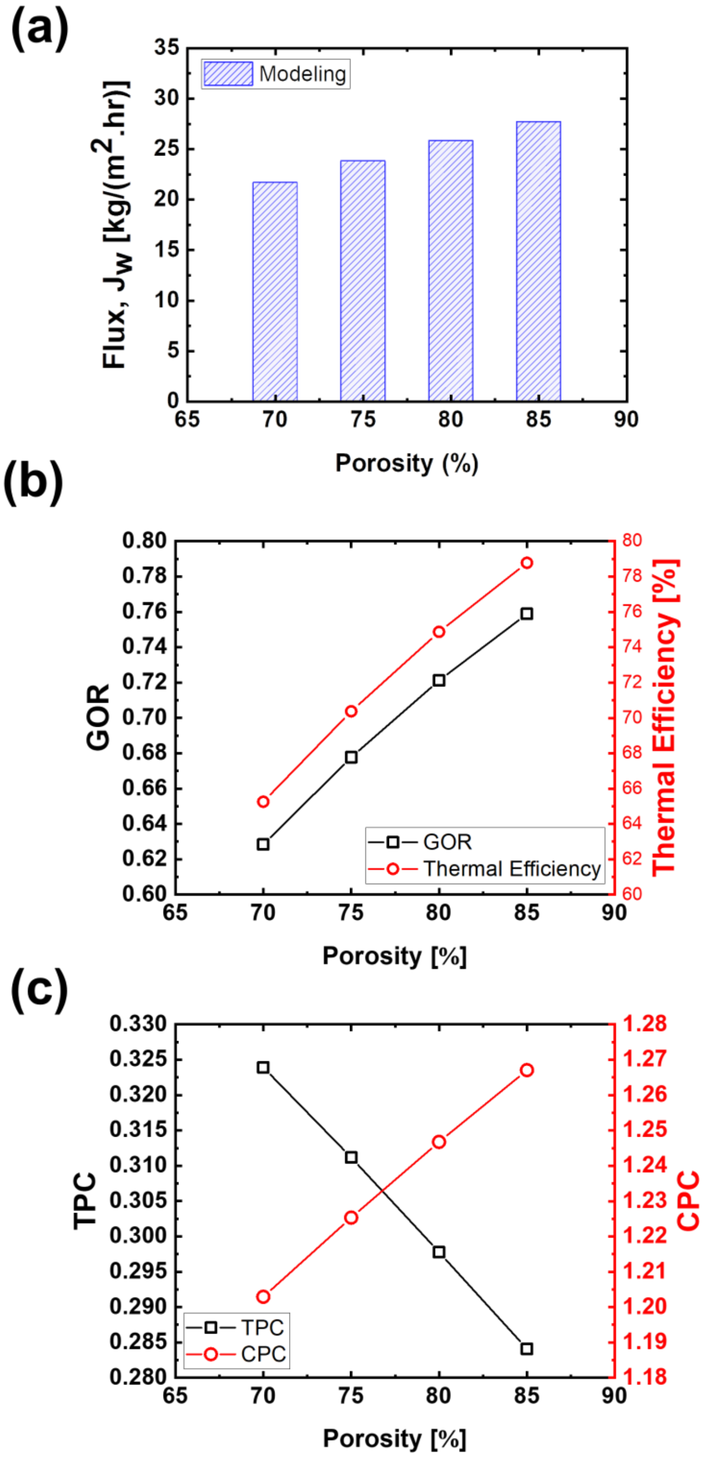

Figure 3.4. DCMD performance based on different porosity a) modeling results for permeate flux, b) GOR & Thermal efficiency, and c) TPC & CPC. All data were provided when the feed solution contained 35 gr/L NaCl. Permeate and feed temperatures were 20 ℃ and 70 ℃, respectively, circulating with flow rates of 0.5 LPM across the PTFE (0.45-micron pore size) membrane.

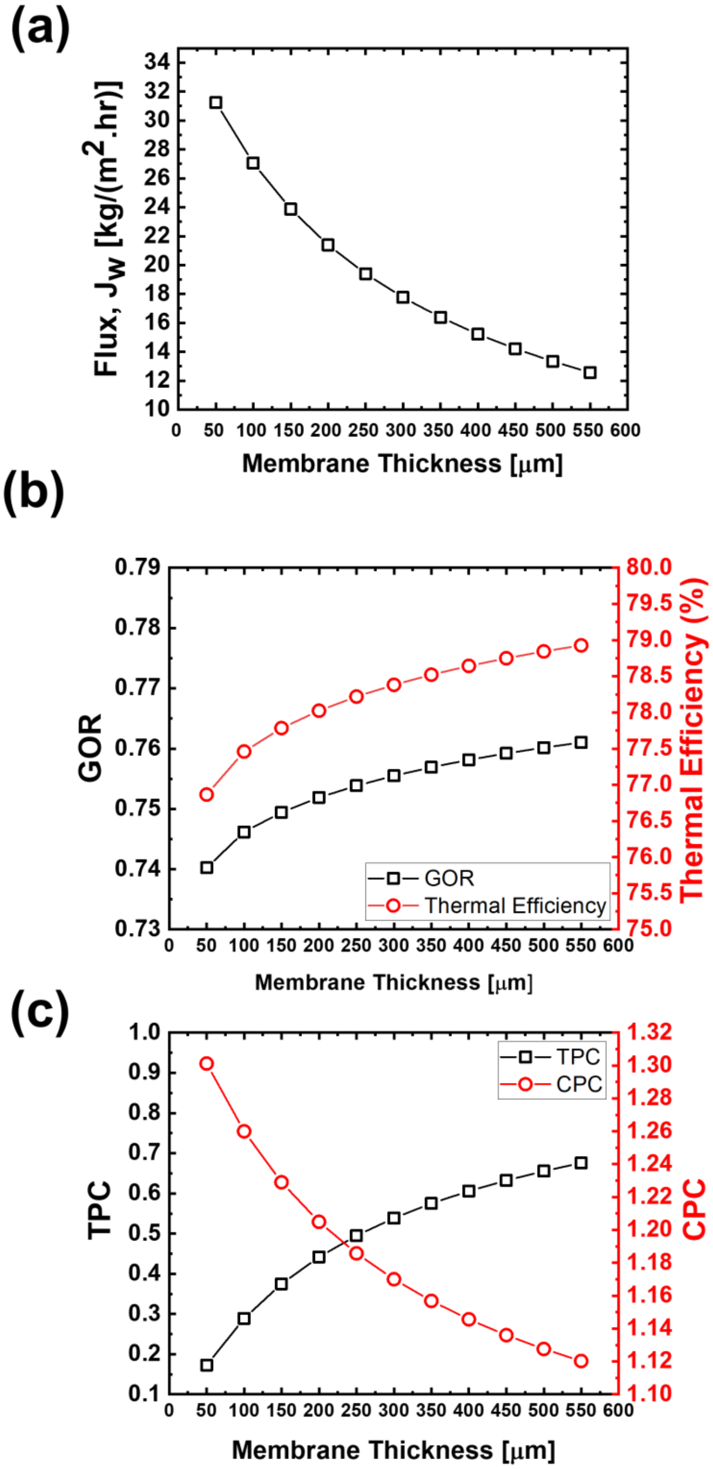

Figure 3.5. DCMD performance based on various membrane thickness a) modeling results for permeate flux, b) GOR & Thermal efficiency, and c) TPC & CPC. All data were achieved when 35 gr/L NaCl was used in the feed solution with a temperature of 70 ℃. The permeate temperature was kept at 20 ℃, and flow rates were 0.5 L. A PTFE sheet with a 0.45-micron pore size was used as a membrane.

3.2.2.4 Membrane material and thermal conductivity

Two different types of membranes, namely PTFE (0.45 μm) and PVDF (0.3 μm) with thermal conductivities of 0.2726 and 0.1926 (W/mK), respectively, were tested at the same operating conditions and the obtained fluxes are illustrated in Figure **3.6** (a). The PTFE membrane with a larger thermal conductivity provided higher flux compared to the PVDF membrane. However, it should be noted that other excellent properties of the PTFE membrane, including lower thickness, larger pore size, and higher hydrophobicity, positively contributed to the achievement of such higher flux. In order to find the actual contribution of thermal conductivity on water flux, the numerical modeling was employed. Most of the polymers being used for the fabrication of MD membranes have a low thermal conductivity, ranging from 0.1 to 0.5 W/(mK). It is worth mentioning that the thermal conductivity of these polymers changes sharply when the working temperature is around the glass transition temperature (T_g) of the polymer. Therefore, it is unlikely that temperature variation in the MD process, which was operated at moderate feed temperatures, would have a significant impact on the magnitude of thermal conductivity [142–144]. As can be observed in Figure **3.6** (b), a membrane with higher thermal conductivity produced lower permeate flux. The higher thermal conductivity allowed more heat to transfer across the membrane, which led to a larger difference between surface temperature and bulk temperature of the fluids. The reduction in the driving force, therefore, caused a decrease in permeate flux, GOR, TPC, and thermal efficiency. Nevertheless, the effect of thermal conductivity on MD performance was found to be trivial. By increasing the thermal conductivity from 0.1 to 0.5 W/(.K), the permeate flux, GOR, thermal efficiency, and TPC reduced only around 2.70%, 3.84%, 3.82%, and 2.60%, respectively and the CPC almost remained constant.

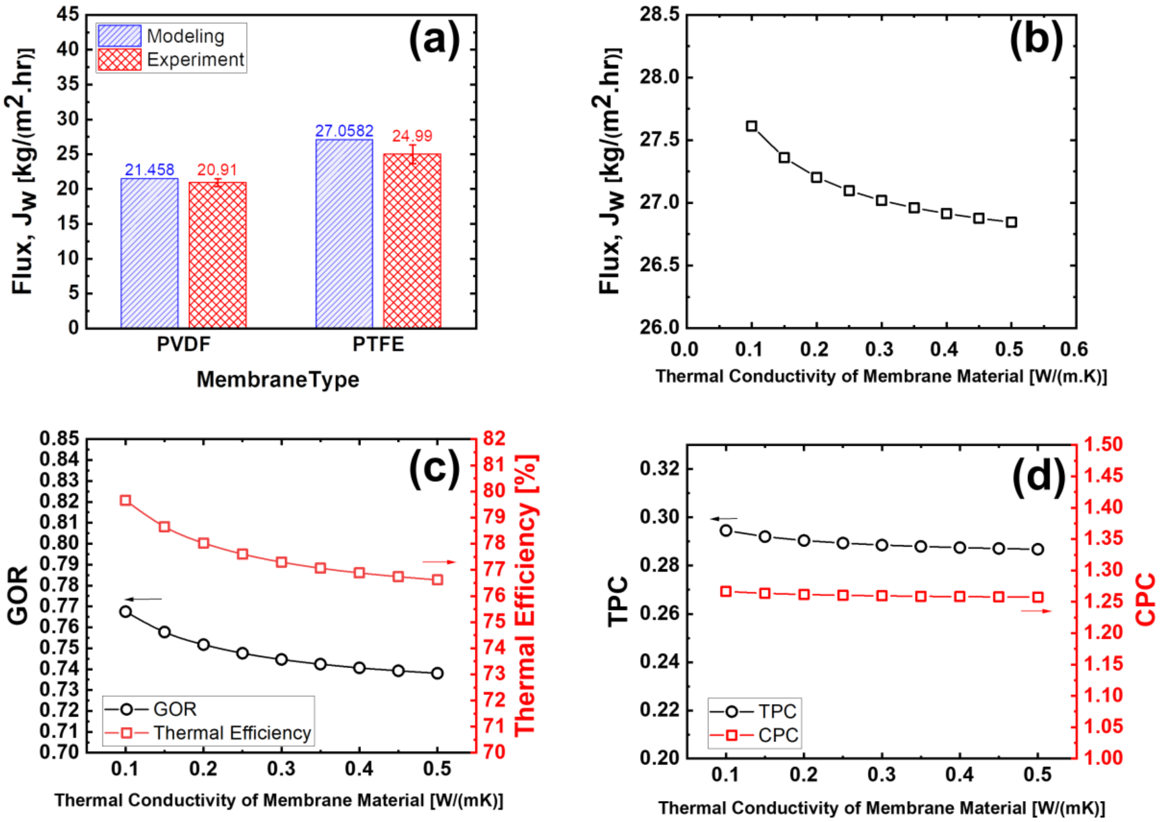

Figure 3.6. DCMD performance based on various thermal conductivity of membrane material a) modeling & experimental results for permeate flux when PVDF and PTFE membranes were used in the MD system. b) Detailed modeling results for permeate flux, c) GOR & thermal efficiency, and d) TPC & CPC. For all tests, 35 gr/L NaCl was used in feed solution and permeate and feed temperatures were kept at 20 ℃ and 70 ℃, respectively, with flow rates of 0.5 LPM.

In summary, our results showed that among all studied operating conditions and membrane properties, the feed temperature, membrane porosity, pore size, and thickness were the most influential parameters on permeate flux, GOR, and thermal efficiency. Higher feed temperature, porosity, and pore size had positive impacts on DCMD performance by increasing the permeate flux, GOR, and thermal efficiency values. However, permeate flux reduced significantly by increasing the membrane thickness. Increasing feed temperature, pore size, and porosity enhanced the CPC, which is undesirable for the MD process. Also, by increasing all parameters, excluding the membrane thickness and flow rate, the TPC decreased, which is not favored in the MD process. To achieve a higher TPC (as close as possible to 1), the heat loss from the membrane surface to the ambient environment should be reduced. Adjustment of flow rates at the highest values is firstly recommended as a major approach to reduce the effect of both temperature and concentration polarizations without sacrificing permeate flux and energy efficiency. It is worth mentioning that the obtained results in this study were for small and Lab-scale MD cells. For larger scale modules, the cold outlet temperature becomes closer to the hot inlet temperature (based on the $\in -\mathrm{NTU}$ method). Therefore, heat recovery features can be added to the MD process. In that case, the membrane area becomes an effective parameter, and the GOR could get values much higher than unity [119,128,141,145–147].

3.3 Conclusion

In this study, a novel 2D mathematical model was developed to predict the DCMD performance in terms of permeate flux, energy efficiency, membrane surface temperature profile, and temperature and concentration polarization effects. Through mathematical modeling, a design map to achieve the optimum performance of a DCMD system by proper adjustment of the operating conditions (temperature, flow rates, module dimension) and membrane properties (pore size, porosity, thickness, and thermal conductivity) was introduced. The modeling results were found to be in good agreement with experimental results with maximum deviation of $\sim 10\%$. A likely reason for the deviation of modeling and experimental results is underestimating the heat loss from the DCMD setup to the environment. Although some parts of the setup, such as the hot feed stream pipes, were covered with insulation, there are some other parts such as the membrane cell, feed tank, and heat exchanger that might contribute to heat loss. Hence the real feed temperature on the membrane surface was lower than the one used in the model that has consequently led to lower experimental permeate flux. Another possible reason is inaccuracy in the measurement of membrane properties such as porosity and thickness. These parameters (membrane porosity and thickness are highly influential on the permeate flux results, and even a minor uncertainty in the measurement of these properties can affect the predictions significantly. In addition, the correlation that was used for the calculation of Nu number could also contribute to the deviation between the model predictions and experimental results. Finally, although we used the most accurate method (Maxwell equation) for calculating thermal conductivity, some possible inaccuracies may contribute to the final deviation between theoretical and experimental results. Based on the results, feed temperature, membrane porosity, pore size, and thickness were found to be the most effective parameters on the permeate flux and energy efficiency. The effect of membrane thermal conductivity on flux and energy efficiency of MD was insignificant. By 60% enhancement of feed temperature, the permeate flux, GOR, and thermal efficiency increased by 181%, 19.63%, and 19.68%, respectively. Also, by 21.4% increment in membrane porosity, the permeate flux, GOR, and thermal efficiency increased 28.93%, 20.85%, and 20.72%, respectively. Pore size increment from 0.1 to 0.45 micron also resulted in 38.34%, 19.22%, and 19.25% enhancement in permeate flux, GOR, and thermal efficiency, respectively. By increasing the membrane thickness from 50 to 550 μm, a 148.6% reduction in permeate flux, and ~2% increment in energy efficiency were obtained. Moreover, a 300% increment in flow rates resulted in a 51.4% increase in permeate flux and reduced the unfavorable effects of temperature and concentration polarizations. It is worth mentioning that the effect of concentration polarization in the MD process is not as high as RO, UF and NF methods mainly due to larger pore size existing in the structure of the hydrophobic porous MD membrane. To achieve higher permeate flux, GOR, and thermal efficiency in the DCMD process, it is suggested that the feed temperature, flow rates, and porosity of the membrane be adjusted at the highest possible values. However, the proper pore size and thickness of the membrane should be obtained with more caution, as changes in these two parameters result in a trade-off between permeate flux, energy efficiency, and rejection. A practical suggestion to obtain a higher GOR is to recover heat from the outlet permeate stream of the membrane module. However, such an energy-saving feature requires a larger scale membrane cell design, which yields a high temperature of permeate outlet close to the feed inlet temperature. Overall, in our lab-scale experiments and the studied range for each factor, the optimum permeate flux, GOR, and thermal efficiency were 40.75 ($\mathrm{kg/(m^2hr)}$), 0.783, and 81.29%, respectively, which was achieved at 80℃ feed temperature, 0.8 LPM flow rate, and using PTFE with 0.45-micron pore size, 100 μm thickness, and 83% porosity. The introduced design map provides valuable guidelines to engineers and membrane scientists to properly adjust the operating conditions and utilize optimal membrane properties.

Acknowledgments: The authors gratefully acknowledge the financial support provided by the Natural Sciences and Engineering Research Council of Canada (NSERC) and Canada's Oil Sands Innovation Alliance (COSIA).

Chapter 4

4 Air gap membrane distillation modeling[2]

4.1 Introduction

Depending on how water is collected in the permeate side, MD can be operated in different configurations [27,63,148]. The two more commonly-used configurations are 1) direct contact membrane distillation (DCMD) and 2) air gap membrane distillation (AGMD). In DCMD, the cold pure water is in direct contact with the membrane surface at the permeate side, while in AGMD, a condensing plate separates the membrane surface from the cold water stream [60,116,128]. The DCMD provides more operational simplicity and relatively higher flux; however, it suffers from a more significant heat loss from the membrane cell to the ambient environment. The air-gap between the membrane surface and the condensing plate in the AGMD can partially decline the rate of heat loss, but it creates an extra resistance against vapor transfer [61–63,149,150]. Figure **4.1** shows the schematic of the DCMD and AGMD processes.

---

[2] The material presented in this chapter is ready for submission as a research paper.

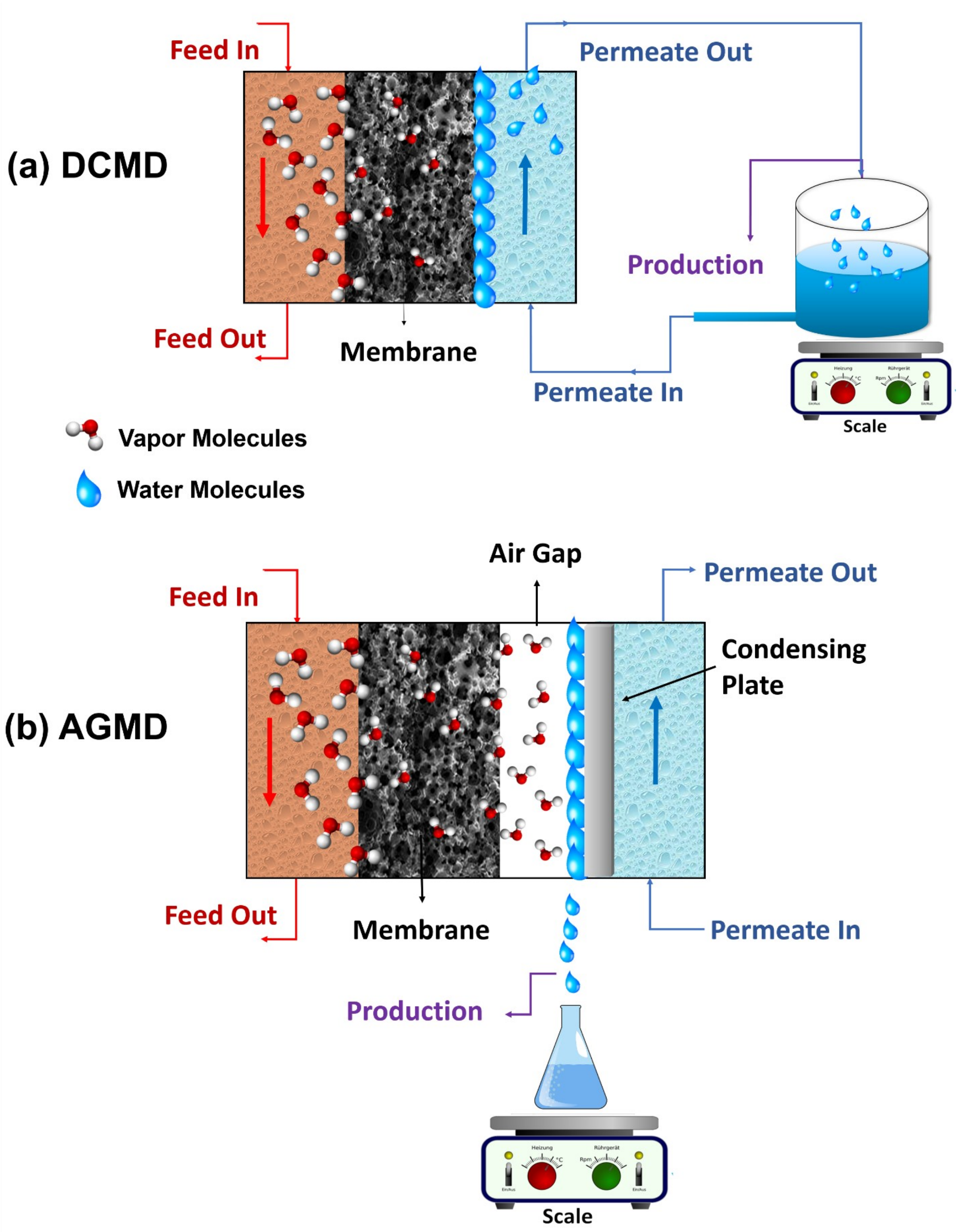

Figure 4.1. A schematic of (a) direct contact membrane distillation process (DCMD) and (b) Air-gap membrane distillation process (AGMD)

Developing a theoretical model enables a comparative study of different configurations, the prediction of the MD performance, and provides an influential tool to justify and optimize the experimental conditions. Mathematical modeling provides the sensitivity analyses of effective parameters including operating conditions (feed and permeate temperature, flow rate, salt concentration, the width of the air-gap for AGMD) and membrane properties (pore size, thermal conductivity, porosity, thickness) on the MD performance which is evaluated by permeate flux, rejection of contaminants (salt) and energy efficiency. Therefore, by utilizing mathematical modeling, valuable insight and a strong framework can be provided for smart adjustment of process parameters and innovative membranes fabrication.

So far, extensive research has been carried out on the mathematical modeling of the MD process [116,119,128,132–134,145,150–155]. Computational fluid dynamics (CFD) was used as one of the numerical methods for MD modeling. Karbasi et al. conducted CFD simulation and experimental studies for two different geometries of membrane module (rectangular and disc-type) in the air-gap membrane distillation (AGMD) syste. Their simulation indicated a 6% deviation from experimental results [133]. Khalifa et al. used a simplified form of dusty gas model (DGM), which is a transport model describing the multicomponent fluid flow through porous media, to study the effects of different operating parameters, such as feed temperature, flow rate, and salt concentration on permeate flux in an AGMD process. Their results indicated that the AGMD performance was mostly affected by changing feed temperature and the width of the air-gap [9,118]. In another modeling and experimental study of AGMD, El Mokhtar et al. used DGM and evaluated the mass transfer through the membrane based on combined Knudsen and molecular diffusion mechanisms, assuming one-directional flow through the feed chamber [132]. They studied the effects of different factors, including feed temperature, the width of the air-gap, salt concentration, flow rates, and pore size of the membrane (0.45 and 0.22 µm) on the permeate flux and salt rejection 34. Feed temperature was reported as the most crucial parameter on AGMD performance, and their modeling results showed a 7% deviation from experimental ones [132]. H. Boukhriss et al. proposed a one-dimensional model for heat and mass transfer in the AGMD process to explore the effects of temperature and the width of air-gap on permeate flux. They obtained maximum permeate flux was 7.4 ($(\mathrm{kg}/(\mathrm{m}^2\mathrm{h}))$) for the highest feed temperature (80 °C) and the smallest air-gap width of 1.5 mm [83].

Despite the development of promising theoretical models for the prediction of the AGMD process, there are still some challenges that need to be addressed. Most of the developed theoretical models relied on experimentally determined parameters such as outlet temperatures [88] which made the simulation to be dependent on a specific experimental condition. Experimentally measurement of all involved parameters, especially in larger scales, is an arduous task where expensive instrumentation should be used in place to record analytical data. In some cases, one-dimensional and simplified models were developed by making many unrealistic assumptions [83,125]. On the other hand, more sophisticated models suffered from high computational complexity and time such as CFD models [122,140]. Besides, the literature is sparse regarding the energy efficiency of the AGMD process. Finally, only a few studies have critically compared the two main configurations of the MD, i.e., direct contact membrane distillation (DCMD) and AGMD [116,119,128,150,154]. Given that, the research would have been more relevant if a self-sustained model, with more realistic assumptions, had been developed to explore the effect of operating and membrane structural parameters on a broader range of response variables, including energy and thermal efficiencies.

In this study, a novel two-dimensional mathematical model is developed by combining the Effectiveness-Number of Transfer Units ($\in -$NTU) and finite difference methods to analyze the AGMD performance. The developed model can predict the permeate flux, energy efficiency, and thermal efficiency of an AGMD process. The model can also estimate the temperature and vapor pressure profiles and detailed thermal cycles without requiring a single parameter obtained from experimentation. The modeling procedure is presented in detail, and the impact of each parameter (the membrane properties and operating conditions) on the AGMD performance is provided. Theoretical results are validated with experimental data for three membranes with different properties at a broad range of operating conditions. Finally, the performance of AGMD is compared with DCMD at similar conditions to provide insight into the strength and limitation of each configuration.

The details of mathematical modeling for AGMD system was explained in chapter 2. The results and discussion of theoretical and experimental studies for the AGMD process are presented in the following section.

4.2 Results and Discussion

In this section, the predictions of the developed mathematical model are first validated against experimental data. Then, the effect of design parameters, including operating conditions (e.g., feed temperature, fluid flow rates and air gap thickness) and membrane properties (e.g., thickness, pore size, porosity, and thermal conductivity) on the permeate flux, energy efficiency, thermal efficiency, and temperature and concentration polarization effects are investigated. The results for the AGMD are also compared with the DCMD process under the same conditions. Finally, the optimum operating conditions and membrane properties to achieve the highest performance of the AGMD system are determined.

4.2.1 Sensitivity analysis of effective operating conditions on the AGMD performance

4.2.1.1 Feed Temperature

The influence of feed temperature variation between 50 to 80 ℃ on the AGMD performance is depicted in Figure **4.2**. The width of the air-gap in the AGMD module was adjusted at 5.6 mm. As can be observed from Figure **4.2**(a), the theoretical results match well with the experimental data, with less than 4% deviation. Also, increasing the feed temperature enhanced the permeate flux significantly. This can be attributed to an increase in the feed-side membrane surface temperature (T_{mf}), which, based on Eqs. (36) and (37), increased the driving force and vapor pressure gradient. Our results showed that a 60% increase in the feed temperature elevated the permeate flux about 200% (from 4.07 to 12.22 $\mathrm{kg/(m^2hr)}$).

According to Figure **4.2**(b), increasing the feed temperature from 50 to 80 ℃ resulted in 1.3% and 2.0% increments in GOR (from 0.725 to 0.734) and thermal efficiency (from 96.2 to 98.2%), respectively. Higher feed temperature has led to higher permeate flux and, based on Eqs. (20), (66) and (68), a larger Q_{v} and energy efficiency achieved. On the other hand, the magnitude of heat loss ($Q_{\mathrm{c,M-ag}}$) increased due to higher T_{mf} at larger feed temperature (Eq. (67)), that countered the positive effect of feed temperature increase on energy efficiency.

Figure **4.2**(c) demonstrates the effect of feed temperature on TPC and CPC. As the feed temperature increased (50 to 80 °C), the TPC reduced by 30% (from 0.63 to 0.44). According to Eqs. (31) and (32) both T_{mf} and T_{film} increased by increasing feed temperature (Table **4.1**). Due to thermal polarization, the actual temperature gradient across the membrane increased less significantly than the bulk temperature difference. As a result, the value of TPC decreased by increasing feed temperature (see Eq. (62)). a 60% increase in the feed temperature, a larger salt concentration was created on the membrane surface due to higher permeate flux (see Eq. (63)) which led to a 16.52% increase in CPC value (from 1.08 to 1.26).

Table 4.1. Calculated membrane surface temperature at the feed side and water film temperature based on different bulk temperatures

δ_{AG}	T_{bf} (°C)	T_{bp} (°C)	ΔT_{bulk} (°C)	T_{mf} (°C)	T_{film} (°C)	$\Delta T_{\mathrm{actual\ driving\ force}}$ (°C)
5.6	50	20	30	44.58	25.69	18.89
	60	20	40	51.51	28.91	22.6
	70	20	50	57.81	32.75	25.06
	80	20	60	63.54	37.09	26.45

4.2.1.2 Feed and Permeate flow rates

The effect of flow rates on the AGMD performance is illustrated in Figure **4.3**. By increasing the flow rates from 0.2 to 8 LPM, permeate flux increased by 67.2%, from 6.38 to 10.68 $\mathrm{kg/(m^2hr)}$, as shown Figure **4.3** (a). A possible explanation is an increase in the convection heat transfer coefficients (h_{i}) at larger Reynolds number. Also, as can be observed in Table **4.2**, the $\mathrm{T_{mf}}$ and $\mathrm{T_{film}}$ became closer to the bulk temperatures , leading to a higher driving force and permeate flux. Figure **4.3** (b), shows that the increment in flow rates from 0.2 to 8 LPM caused only a 1.18% increase in GOR, and thermal efficiency almost remained constant.

Based on Eqs. 20 and 68, larger permeate flux at higher flow rates results in greater Q_{v} and GOR. However, at higher the flow rate, higher energy was transferred from the heat exchanger (Q_{H}), which somehow compromises the effect of enhanced Q_{v} (Eq. (68)) [19]. What's more, the larger driving force at higher flow rates resulted in larger $Q_{\mathrm{c,M-ag}}$ (Eq. (67)) and and consequently a trivial increase in thermal efficiency was observed. An increase in flow rates from 0.2 to 8 LPM diminished the effect of temperature and concentration polarization, where a 53.2% increment in TPC (0.56 to 0.86) and a 9.2% drop in CPC (from 1.13 to 1.03) were observed (Figure **4.3**(c)). Possible reasons for such observations are larger convection transfer coefficient and closer membrane surface and water film temperatures to the bulk temperatures at higher flow rates (Table **4.2**).

Table 4.2. Effect of different flow rates on the membrane surface and water film temperatures, for PTFE 0.45-micron membrane and counter-current flow direction.

δ_{ag} (μm)	**Flowrate** (LPM)	$T_{\mathrm{h,in}}$ (°C)	$T_{\mathrm{c,in}}$ (°C)	$T_{\mathrm{h,out}}$ (°C)	T_{mf} (°C)	T_{film} (°C)
5.6	0.2	60	20	57.017	51.51	28.91
	0.5	60	20	58.61	53.30	27.23
	0.8	60	20	59.07	54.08	26.50
	1	60	20	59.24	54.42	26.18
	2	60	20	59.59	55.37	25.28
	2.9	60	20	59.71	55.81	24.851
	3.2	60	20	59.75	54.86	24.46
	5	60	20	59.81	57.43	24.56
	7	60	20	59.86	58.26	24.71
	8	60	20	59.88	58.48	23.86

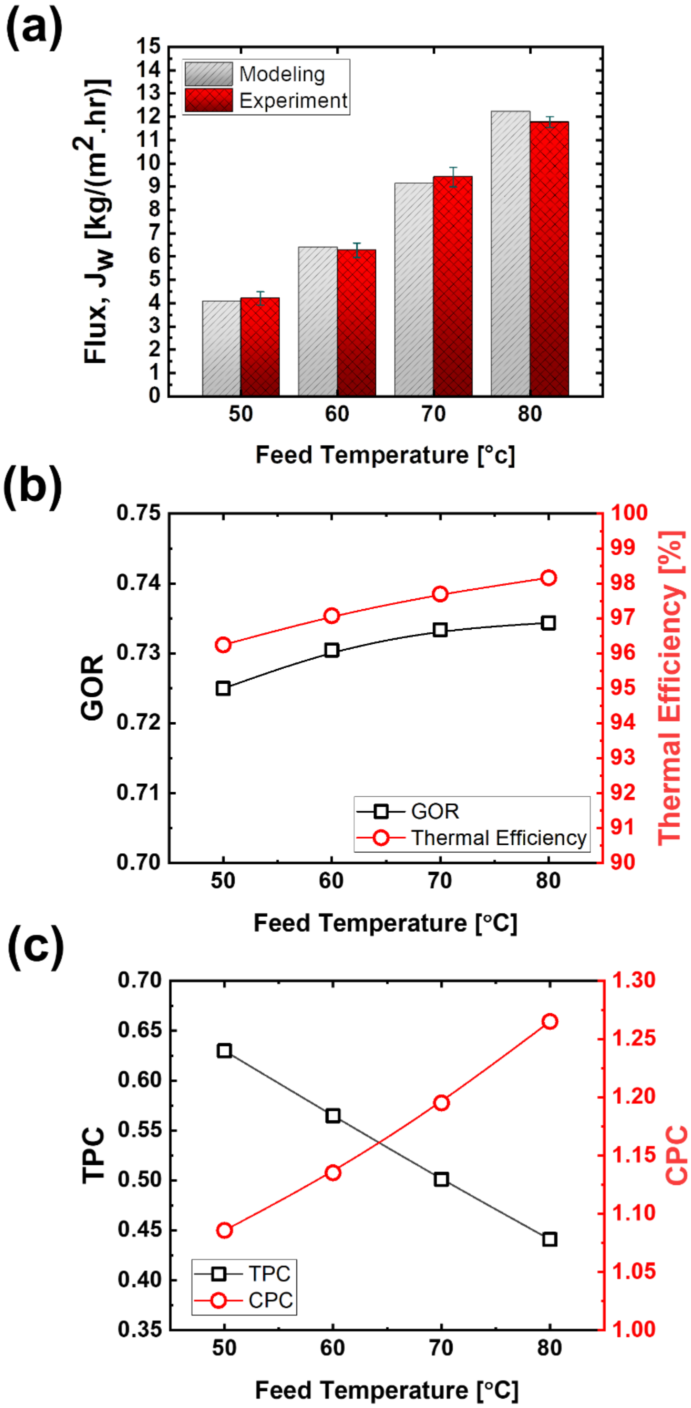

Figure 4.2. AGMD performance based on various feed temperatures a) modeling and experimental results for permeate flux, b) GOR & thermal efficiency, and c) TPC & CPC. For all, 35 gr/L NaCl was used in the feed solution, and permeate temperature was kept at 20 °C. Both streams had flow rates of 0.2 LPM, and PTFE (0.45 µm) was used as a membrane, and the air-gap width was 5.6 mm.

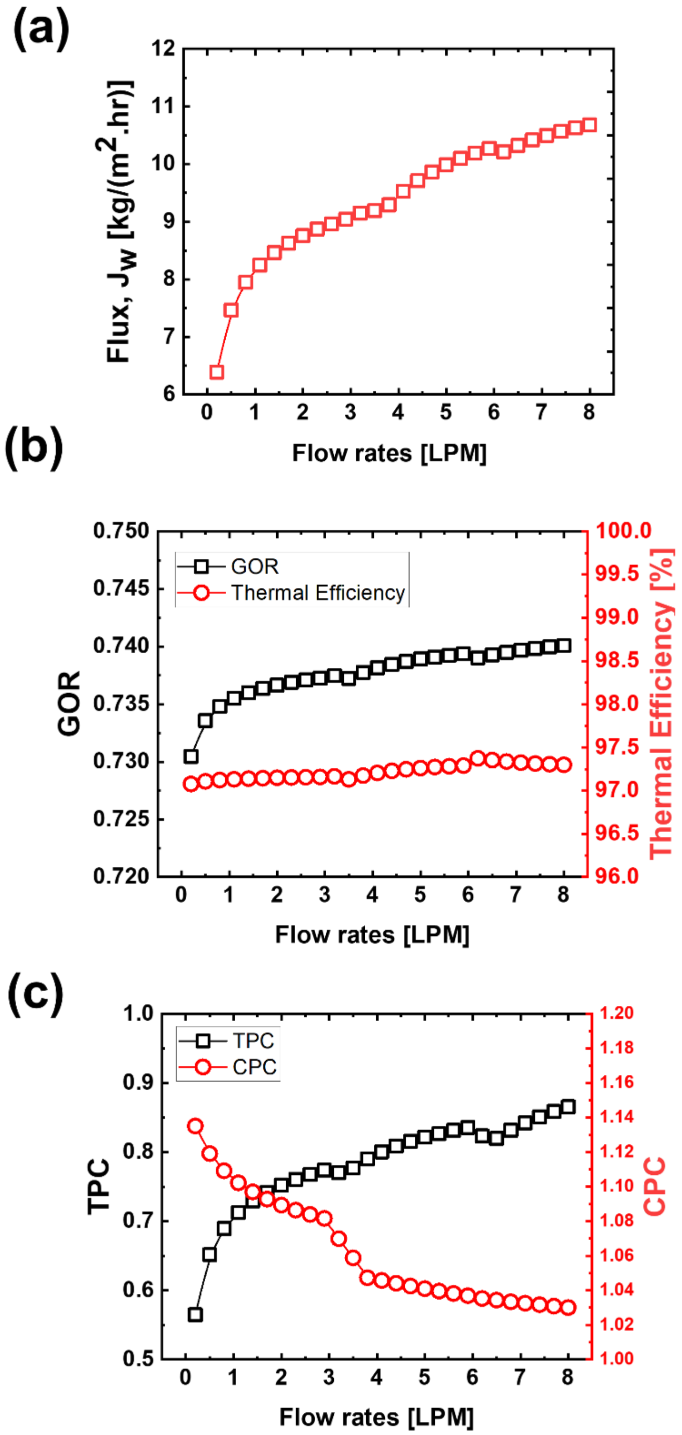

Figure 4.3. AGMD performance based on various feed and permeate flow rates a) modeling results for permeate flux b) GOR & thermal efficiency c) TPC & CPC. For all, 35 gr/L NaCl was used in the feed solution, and Feed and permeate temperatures were kept at 60 ℃ and 20 ℃, respectively. PTFE (0.45 µm) was used as a membrane and air gap thickness was 5.6 mm.

4.2.1.3 The width of the air gap

The air-gap is used to reduce the heat loss from the membrane module to the ambient environment and thus increase the thermal and energy efficiencies. However, it creates an extra resistance against the mass transfer, reducing permeate flux. Figure **4.4** (a) shows an excellent agreement between the theoretical and experimental results, with less than 2% deviation. As can be seen in Figure **4.4**(b) by increasing the width of the air-gap from 0.6 mm to 5.6 mm, the water flux decreased significantly. The permeate flux decreased by 36.8% from 10.1 to 6.4 $\mathrm{kg/(m^2hr)}$ when the width of the air-gap increased from 0.6 mm to 5.6 mm. Such a flux decline can be attributed to an increase in R_{ag}, which resulted in lower total mass transfer coefficient ($\mathrm{B_M}$), based on Eqs (49) to (51) and Eq. (36). In addition, due to less heat loss ($Q_{\mathrm{c,M-ag}}$) for the larger air-gaps, thermal efficiency and GOR increased 4.06% and 9.26%, respectively (Figure **4.4**(c)). Finally, according to Figure **4.4**(d) and Table **4.3**, the increment in the width of the air-gap reduced the undesirable temperature and concentration polarization effects. As can be seen, a 118% increase in TPC (from 0.25 to 0.56) and a 6.7% reduction in CPC (from 1.21 to 1.13) were obtained by increasing the width of the air-gap from 0.6 mm to 5.6 mm. This can be attributed to the larger driving force and lower permeate flux for larger air gaps.

Table 4.3. Effect of different air gap widths on driving force and overall mass transfer coefficient, for PTFE 0.45-micron membrane and 0.2 LPM counter-current flow rates

$\boldsymbol{\delta_{ag}}$ (μm)	$\mathbf{T_{bf}}$ (°C)	$\mathbf{T_{bp}}$ (°C)	$\mathbf{\Delta T_{bulk}}$ (°C)	$\mathbf{T_{mf}}$ (°C)	$\mathbf{T_{film}}$ (°C)	$\mathbf{\Delta T_{actual\ driving\ force}}$ (°C)	$\mathbf{R_{ag}}$ $\mathrm{(m^2.s.Pa)/kg)}$	$\mathbf{B_M}$ $\mathrm{(kg/(m^2.s.Pa))}$
5.6	60	20	40	51.51	28.91	22.59	4.15E6	1.97E-7
4.6	60	20	40	50.79	29.69	21.09	3.43E6	2.29E-7
3.6	60	20	40	49.931	30.64	19.29	2.69E6	2.75E-7
2.6	60	20	40	48.88	31.81	17.06	1.97E6	3.45E-7
1.6	60	20	40	47.56	33.33	14.23	1.21E6	4.61E-7
0.6	60	20	40	45.88	35.53	10.35	4.57E5	7.02E-7

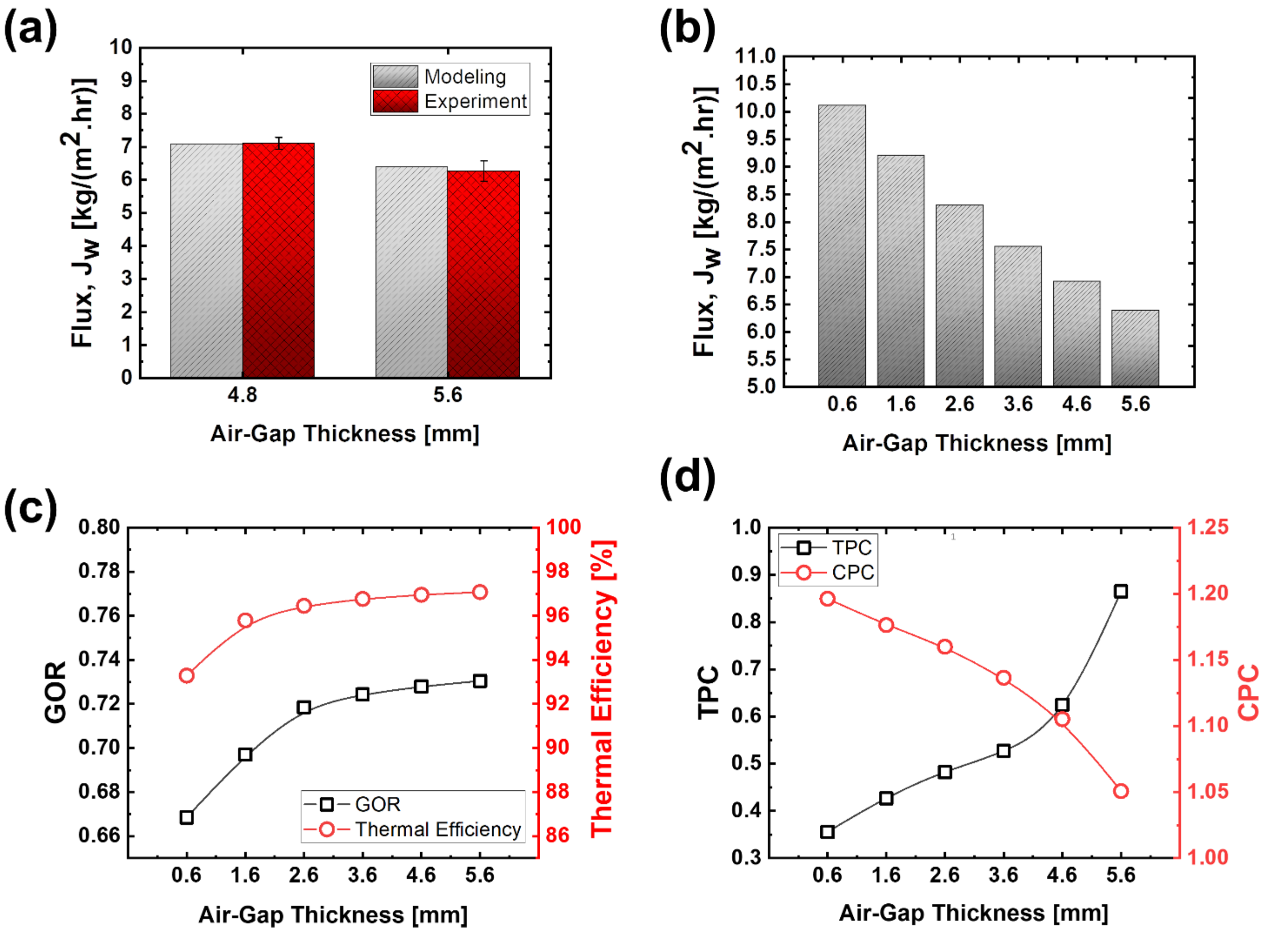

Figure 4.4. AGMD performance based on various air gap thicknesses a) modeling and experimental results for permeate flux b) GOR & thermal efficiency c) TPC & CPC. For all, 35 gr/L NaCl was used in the feed solution, and Feed and permeate temperatures were kept at 60 ℃ and 20 ℃, respectively, with 0.2 LPM flow rates. PTFE (0.45 μm) was used as a membrane.

4.2.2 Sensitivity analysis of effective membrane properties on the AGMD performance

4.2.2.1 Membrane thickness

The impact of membrane thickness on the AGMD performance is presented in Figure **4.5**. Increasing the membrane thickness causes higher resistance against mass and heat transfer ($\mathrm{R_K}$ and $\mathrm{R_m}$), resulting in a higher membrane surface temperature in the feed side ($\mathrm{T_{mf}}$) and a lower total mass transfer coefficient. Therefore, as illustrated in Figure **4.5**.(a), increasing the membrane thickness from 50 to 250 μm, decreased the permeate flux by 20.5% from 6.8 to 5.4 $\mathrm{kg/(m^2hr)}$. However, as can be seen from Figure **4.5**(b), membrane thickness did not have significant impacts on energy efficiency. Increasing the membrane thickness and $\mathrm{T_{mf}}$ reduces $\mathrm{Q_v}$ and $\mathrm{Q_H}$ parameters, while $\mathrm{Q_{c,M-ag}}$ increases (see Eqs. (20), (67) and (68)). As a result of such counter effects, energy efficiency could not be notably be affected by the membrane thickness. Moreover, based on Figure **4.5**(c), increasing the membrane thickness had a positive impact on the temperature and concentration polarization, which are manifested in a 16. 9% increase in TPC (from 0.54 to 0.63) and a 2.6% drop in CPC (from 1.14 to 1.11).

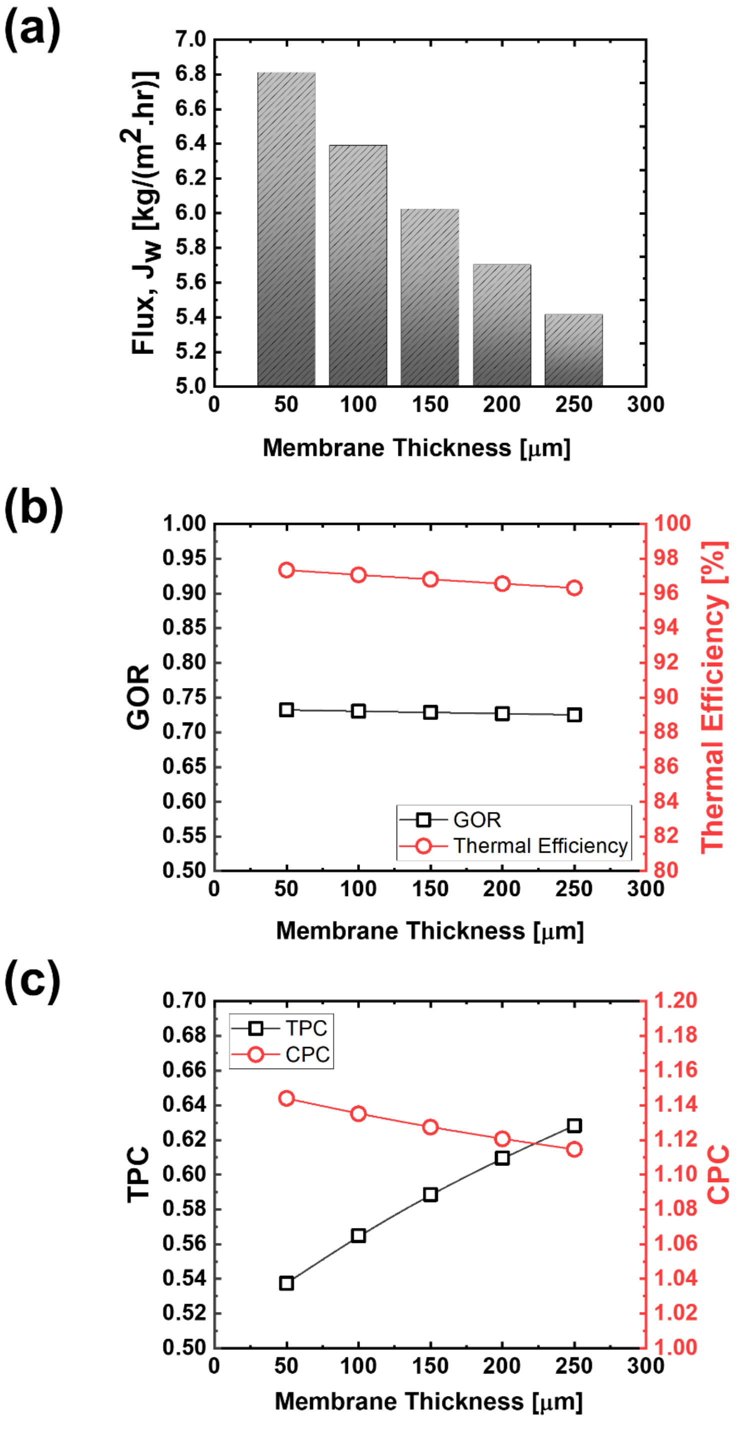

Figure 4.5. AGMD performance based on various membrane thicknesses a) modeling results for permeate flux, b) GOR & thermal efficiency, and c) TPC & CPC. For all, 35 gr/L NaCl was used in the feed solution, and Feed and permeate temperatures were kept at 60 ℃ and 20 ℃, respectively, with 0.2 LPM flow rates. PTFE (0.45 μm) was used as a membrane.

4.2.2.2 Membrane pore size, porosity, and thermal conductivity

The effect of membrane pore size, porosity, and thermal conductivity on the AGMD performance are investigated and presented in Figure **4.6.**, panels (i), (ii), (iii) respectively. These three factors influence the magnitude of resistances against mass and heat transfer and subsequently can change the water flux through the membrane

The results of AGMD performances for three commercial PTFE membranes with different pores sizes (0.1, 0.2, and 0.45 μm) are provided in Figure **4.6**. (i). Based on Figure **4.6**(i,a), theoretical and experimental results are in good agreement, with less than 2% deviation. However, the deviation between modeling and experimental results in the case of 0.1 μm pore size was larger, which can be rationalized by looking at the flow type passing through the membrane pores. For 0.1 μm pore size, based on the calculated Knudsen number (Eq.(41)), only the Knudsen flow type (Eqs. (49)-(51)), was assumed in the modeling, which resulted in a higher mass transfer coefficient (B_{M}) and predicted water flux. However, in real PTFE membranes, the pores are not cylindrical and randomly distributed; therefore, the combination of molecular diffusion and Knudsen flow types could have simultaneously occurred, resulting in a lower real permeate flux.

Figure **4.6** (panels b and c) shows that the GOR, thermal efficiency, TPC, and CPC remained almost constant by increasing the pore size from 0.1 to 0.45 μm, porosity from 70 to 85%, and thermal conductivity from 0.1 to 0.5 W/mK. A likely explanation is that extremely thick air-gap compared to membrane thickness creates a huge resistance against mass (R_{ag}) and heat ($\frac{\delta_{\mathrm{ag}}}{\mathrm{K}_{\mathrm{air}}}$) transfer, so that the effect of altering the membrane structural parameters on the AGMD performance cannot be detected. In addition, the permeate flux almost remained constant by increasing the porosity and membrane thermal conductivity.

.

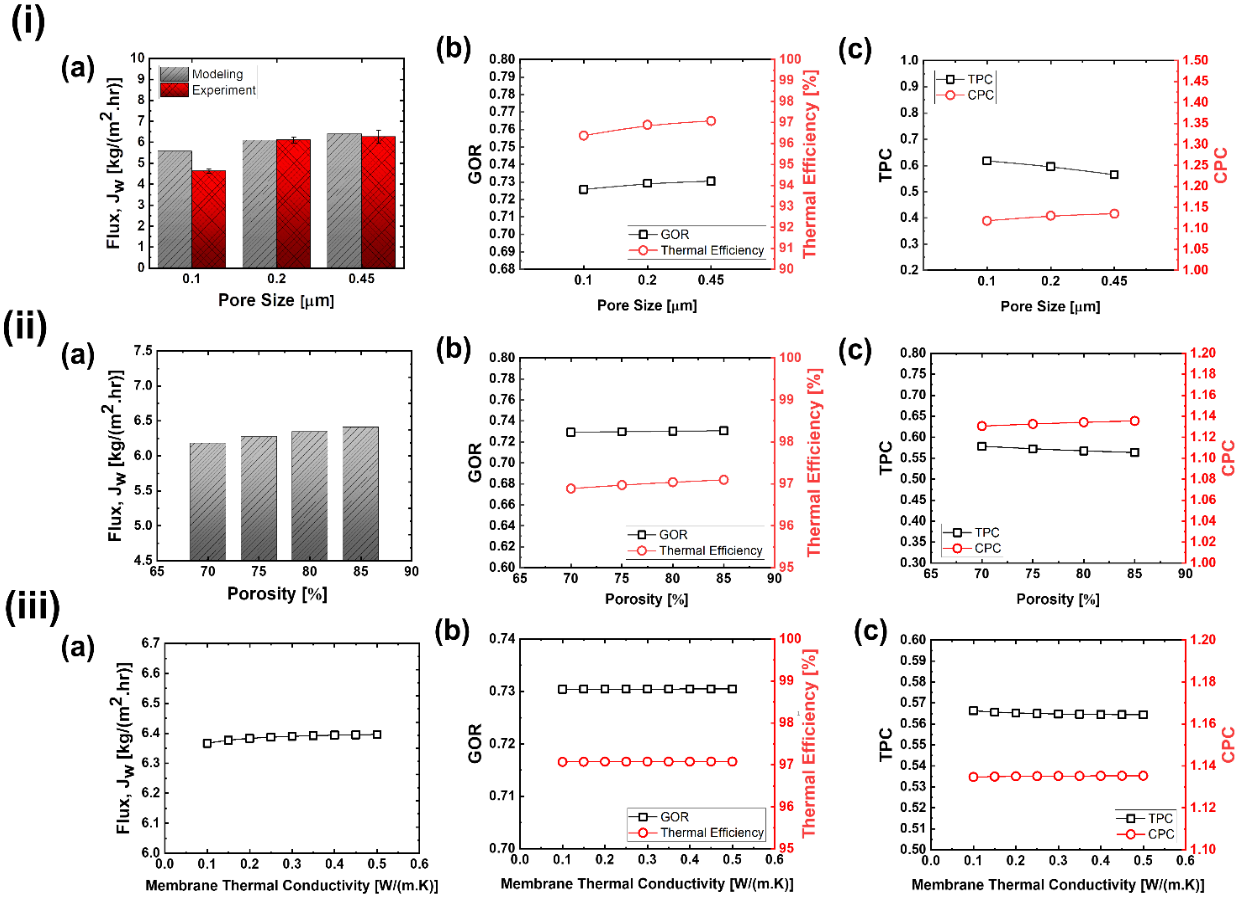

Figure 4.6. AGMD performance for (i) different membrane pore sizes of the PTFE membrane, (ii) membrane porosity of PTFE membrane (0.45 μm), and (iii) membrane thermal conductivity. a) Modeling results for permeate flux, b) GOR & thermal efficiency, and c) TPC & CPC. For all, 35 gr/L NaCl was used in the feed solution, and feed and permeate temperatures were kept at 60 °C and 20 °C, respectively, with 0.2 LPM flow rates. The width of the air-gap was 5.6 mm.

4.2.3 Comparative study of AGMD and DCMD process

In this section, AGMD and DCMD modeling results are compared. DCMD was modeled with the same $\in -$NTU approach, integrated with the finite-difference method. The only difference was an extra resistance against mass and heat transfer in the AGMD system due to the presence of an air-gap in the permeate side. The driving force in the DCMD system is the temperature difference between the membrane surface temperatures (T_{mf} & T_{mp}), while for the AGMD process is the difference between T_{mf} and T_{film} . Here, we compared the performance of both systems at the same operating conditions, membrane properties, and module dimensions. The feed temperature and flow rates were set to 60 ℃ and 0.2 LPM, respectively, and the PTFE membrane of 0.45 μm pore size (see Table **2.8** for other properties of this membrane) was used. The comparative results are illustrated in Figure **4.7**. According to this figure, as the width of the air-gap decreased, the permeate flux increased due to lower mass transfer resistance originated from the air gap (R_{ag}).

Figure **4.7**(a) shows that shows that the permeate flux for the DCMD was 14.7 $\frac{\mathrm{kg}}{\mathrm{m^2hr}}$, while it was $6.38\ \mathrm{kg/(m^2hr)}$ for the AGMD with a 5.6 mm width of air-gap, indicating 56.6% flux decline for the AGMD process. On the other hand, the thermal efficiency of AGMD was larger than that of DCMD, and it was elevated by increasing the thickness of the air-gap (Figure **4.7** (b)). This can be attributed to the added thermal resistance ($\frac{\delta_{\mathrm{ag}}}{\mathrm{K_{air}}}$), which led to a lower heat loss from the membrane module to the ambient environment ($Q_{\mathrm{c,M-ag}}$). However, the GOR value for the DCMD was more than the AGMD system due to its higher permeate flux. Moreover, the GOR value (Eq. (68)) did not change significantly by increasing the thickness of the air-gap due to the reduction of both Q_{v} and Q_{H} (Table **4.4**). The thermal efficiencies were 73.05% and 97.07% for the DCMD and AGMD, respectively. However, the GOR was 27.31% higher for the DCMD. The thermal efficiencies were 73% and 97% for the DCMD and AGMD, respectively. However, the DCMD demonstrated a 27.3% higher GOR value than AGMD. As it is illustrated in Figure **4.7**(c), the AGMD process reduced the undesirable effects of temperature and concentration polarization by lowering the heat loss and permeate flux. The TPC increased by 121% from 0.14 to 0.56, and CPC reduced by 4% from 1.16 to 1.13 for DCMD and AGMD, respectively. Overall, it can be concluded that AGMD can provide better performance than DCMD in desalination if the thickness of the air-gap is properly optimized.

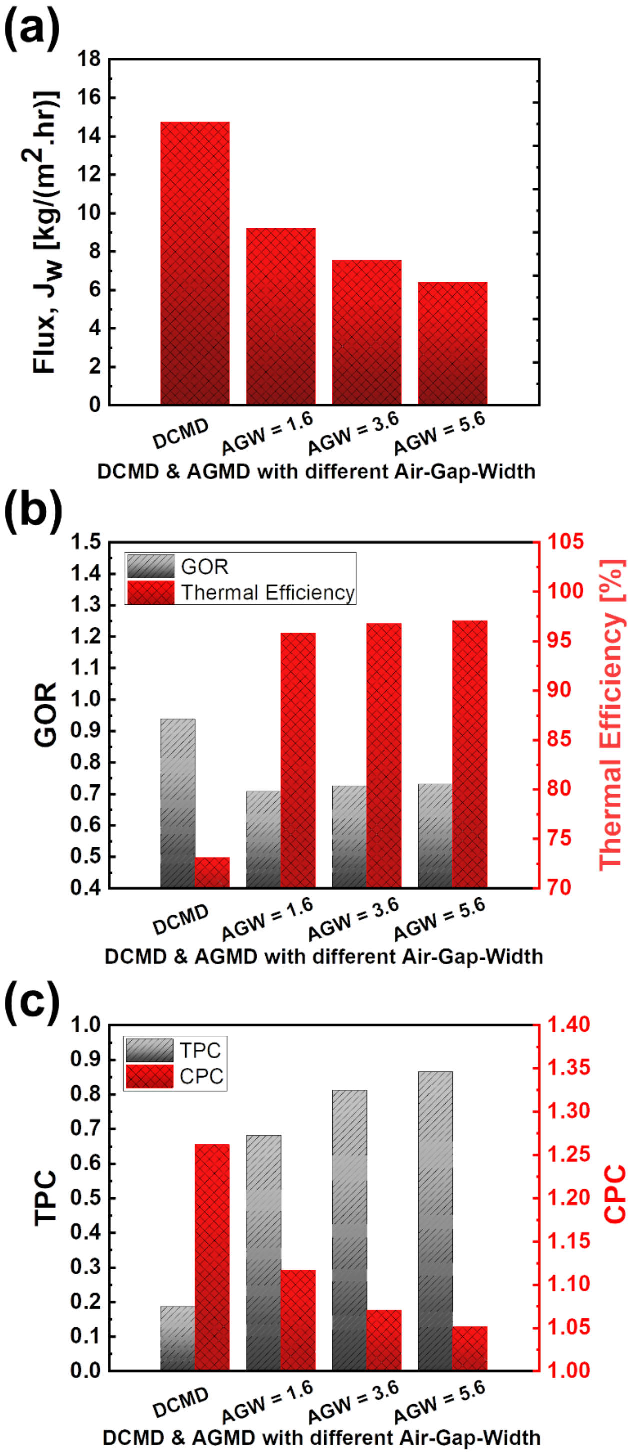

Figure 4.7. Comparative study on AGMD and DCMD performances. a) Modeling results for permeate flux, b) GOR & thermal efficiency, and c) TPC & CPC. For all, 35 gr/L NaCl was used in the feed solution and feed and permeate temperatures were kept at 60 ℃ and 20 ℃, respectively, with 0.2 LPM flow rates and a PTFE with a pore size of 0.45 µm.

Table 4.4. Effects of different air gap widths on outlet hot temperature from membrane module ($T_{hot,out}$), heat carried by vapor molecules (Q_v) and energy consumption for heating the feed solution (Q_H) for PTFE 0.45-micron membrane and 0.2 LPM counter-current flow rates.

Configuration		$\mathbf{T_{h,in}}$ [°C]	$\mathbf{T_{h,out}}$ [°C]	$\mathbf{Q_H}$ [W]	$\mathbf{Q_v}$ $[\frac{W}{m^2}]$
DCMD		60	53.49	91.87	1.042E4
AGMD	δ_{ag} = 1.6	60	55.52	62.33	5.21E3
	δ_{ag} = 3.6	60	55.58	49.99	4.28E3
	δ_{ag} = 5.6	60	56.45	42.03	3.63E3

In summary, as can be observed from Table **4.5**, among all studied operating conditions, the feed temperature was the most effective parameter on permeate flux, GOR, and thermal efficiency. The thickness of the air-gap and flow rates were found to be the second most significant impact on permeate flux and energy efficiency. Moreover, increasing flow rates and the thickness of the air-gap reduced the undesirable effects of temperature and concentration polarization. Among the membrane properties, membrane thickness and pore size were the most influential ones on on permeate flux, TPC, and CPC. Other membrane properties, including membrane porosity and thermal conductivity, did not show a significant impact on AGMD performance.

By minimizing the thickness of the air-gap, the contribution of membrane properties (porosity and pore size) in resistances against mass transfer becomes more significant; thereby, they could effectively alter the AGMD overall performance. Membrane properties like pore size and thickness should be optimized to prevent pore wetting and provide better mechanical stability during the operation. Even though larger air-gaps result in better AGMD performance by improving the energy efficiency and reduction of temperature and concentration polarization effects, but this improvement is achieved at the expense of reduced permeate flux.

Table 4.5. The alteration of AGMD performance (Permeate flux, thermal efficiency, GOR, TPC, CPC) based on changing effective parameters. The plus and minus signs show the increment and reduction of each parameter, respectively.

Parameter		Alteration Percentage %	Permeate Flux	Thermal efficiency	GOR	TPC	CPC
Operating conditions and module properties	**Feed Temperature** [°C]	(50 -80) + 60%	+ 200.17	+ 1.99	+ 1.294	- 30.002	+ 16.52
	Flow Rates [LPM]	(0.2-8) + 3900%	+ 67.19	+ 0.23	+ 1.318	+ 53.22	- 9.25
	Air gap thickness [mm]	(0.6-5.6) + 833%	- 36.81	+ 4.064	+ 9.26	+ 118.28	- 6.703
Membrane properties	**Pore size** [µm]	(0.1-0.45) + 350%	+ 14.55	+ 0.73	+ 0.65	- 8.56	+ 1.52
	Porosity [%]	(70-85) + 21.43%	+ 3.69	+ 0.21	+ 0.19	- 2.58	+ 0.43
	Membrane Thickness [µm]	(50-250) + 400%	- 20.49	- 1.05	- 0.93	+ 16.89	- 2.57
	Thermal conductivity [W/mK]	(0.1-0.5) + 400%	+ 0.47	+ 0.0084	+ 0.0058	- 0.33	+ 0.052

4.3 Conclusion

In this study, the performance of AGMD was evaluated by developing a novel self-sustained 2D theoretical model. The system performance was assessed in terms of permeate flux, energy efficiency, temperature profile on the membrane surface, as well as temperature and concentration polarization effects. The predictions from the theoretical model were in good agreement with the experimentally measured values at a wide range of conditions (<4% deviation). According to the results, feed temperature, thickness of air-gap, and flow rates were found to be the most influential parameters on AGMD performance. By a 60% increase in the feed temperature, the permeate flux, GOR, and thermal efficiency increased by 200%, 1.29%, and 2.0%, respectively. In addition, by increasing the flow rate from 0.2 to 8 LPM, the permeate flux enhanced 67.2%. However, increasing the thickness of the air-gap caused a 36.8% reduction in the permeate flux. Besides, by increasing the flow rates and width of the air-gap, the unfavorable effects of temperature and concentration polarization reduced. On the other hand, membrane properties such as thermal conductivity and porosity did not show significant impacts on system performance. Pore size increment from 0.1 to 0.45 μm resulted in a 14.5% enhancement in the permeate flux. Increasing the membrane thickness from 50 to 250 μm caused a 20.5% reduction in the permeate flux. The energy efficiency of the system was more sensitive to the feed temperature compared to other effective parameters. The results of a comparative study between DCMD and AGMD systems showed that the permeate flux for the DCMD was 56.6% higher compared to AGMD at the same conditions. Although the GOR was 27.3% higher for DCMD due to its larger permeate flux, AGMD showed a 24.7% higher thermal efficiency compared to DCMD. The AGMD process reduced the undesirable effects of temperature and concentration polarization by a 121% increase in TPC value and a 4% reduction in CPC value as compared to DCMD. Increasing the width of the air-gap was found to provide higher energy efficiency and lower temperature and concentration polarization effects at the expense of significant flux decline. Our studies showed that by optimizing the thickness of the air-gap, better performance could be achieved without a significant reduction in permeate flux. To obtain a higher TPC and lower CPC (as close as possible to 1) in the AGMD system, improvement of flow rate is initially recommended as the main approach to reduce the effect of both temperature and concentration polarizations without sacrificing permeate flux and energy efficiency. Overall, in our lab-scale experiments and the studied range of each factor, the optimum permeate flux, GOR, and thermal efficiency were 12.81 ($\mathrm{kg/(m^2hr)}$), 0.73, and 98.1%, respectively, which were achieved when feed temperature and flow rate were adjusted at 80°C and 0.2 LPM, respectively, and a PTFE membrane with 0.45-micron pore size, 100 μm thickness, and 83% porosity was used in an AGMD module with 4.8 mm air-gap thickness. The introduced design map provides valuable guidelines to scientists and engineers for proper adjustment of the operating conditions and optimization of membrane properties.

Chapter 5

5 Conclusions

5.1 Overall conclusion

Researchers in industry and academia found the MD process very attractive because: (a) it has high potential to be performed for water desalination with salt rejection rate as high as 100% (b) it is able to solve the current facing challenges for other conventional desalination techniques (c) it can be implemented under atmospheric pressure, and (d) it has a relatively simple design, moreover, (e) it can be utilized in a wide range of applications and take advantages of renewable energy due to low operational temperature. However, there are also some limitations such as membrane wetting, uncertain energy consumption and cost, temperature, and concentration polarization that have prevented its full deployment on a large industrial scale. In order to overcome these shortcomings and improve the performance of the MD process, there is a need for (1) evaluation and prediction of the MD performance by mathematical modeling of heat and mass transfer mechanisms (2) providing an optimum design map for the system performance before implementation in small or larger scales to maximize the energy efficiency and obtain a steady high permeate flow, (3) reduction of the heat loss from the system and seek for sustainable sources of heating such as solar irradiation and geothermal to reduce the cost of separation, and (4) development of long-life, reliable, thermally-stable and low-cost membranes that are resistant against pore wetting and fouling due to the presence of contaminants.

Therefore, in order to make the MD technology to be competitive to alternative separation and desalination techniques in the industry, in this study, we developed a mathematical model to give a powerful insight into detailed MD process and optimization of the system performance. Since MD system can be operated in different configurations, we provided our model for two commonly used configurations (DCMD and AGMD) due to their simplicity, lower cost, higher permeate flux, and lower heat loss compared to other configurations.

First, we developed a novel 2D mathematical model inspiring by the Effectiveness-Number of Transfer Units (∈-NTU) method for both DCMD and AGMD systems, which was successfully implemented by using MATLAB software. The introduced model does not need to utilize any parameter obtained from an experimental operation such as permeate flux and outlet properties of fluid streams, which makes the modeling to be applied to any systems with different dimensions and properties. Moreover, the developed model provides low computational burden but accurate theoretical results in comparison with experimentations.

Through theoretical modeling, the system performance in terms of permeate flux, energy efficiency, temperature profile over and across the membrane, temperature, and concentration polarization effects was predicted. By sensitivity analyses through the developed model, a design map to achieve the optimum performance of DCMD and AGMD systems was provided by proper adjustment of the operating conditions (temperature, flow rates, module dimension) and membrane properties (pore size, porosity, thickness, and thermal conductivity). The predictions from the theoretical model were validated with experimental results at various conditions. They have shown good agreements with deviation as low as ~10% and <4% for DCMD and AGMD systems, respectively.

According to the results and sensitivity analyses of influential parameters, feed temperature, membrane porosity, pore size, and thickness were found to be the most effective parameters on the permeate flux and energy efficiency of DCMD system. In contrast, feed temperature, air gap thickness, and flow rates were the most influential parameters on the AGMD performance. Due to the larger air gap thickness compared to membrane thickness, the impact of membrane properties such as thermal conductivity and porosity were less significant in the AGMD system compared to the DCMD process, especially for energy efficiency. Moreover, flow rate and air gap thickness increment could reduce the undesirable effects of temperature and concentration polarization for DCMD and AGMD process.

Therefore, based on our sensitivity analyses study, as an optimum design map to achieve higher permeate flux, GOR, and thermal efficiency, it is suggested to adjust the feed temperature and flow rates at the highest possible values for both systems. However, the membrane properties and air gap thickness should be optimized more carefully because by increasing the membrane thickness and air gap width, the trade-off between water production and energy efficiency could occur. Moreover, the larger pore size may results in pore wetting in the membrane. In order to reduce the effect of temperature and concentration polarization, the flow rate adjustment at the highest values is firstly recommended as a major approach for both DCMD and AGMD systems without sacrificing permeate flux and energy efficiency. The second suggestion for the AGMD system is the larger air gap thickness, but it should be determined by more caution to have a less significant effect on lowering the permeate flux. In addition, for the larger-scale applications, to obtain higher GOR, it is recommended to recover heat from the outlet permeate stream of the membrane module as the energy-saving feature.

Furthermore, in our comparative study between DCMD and AGMD systems, DCMD indicated 56.59% and 27.31% higher permeate flux and GOR, respectively, than the AGMD system. However, the AGMD process showed 24.74% higher energy efficiency and less effect of temperature and concentration polarization by a 120.8% increase in TPC value and a 4.01% reduction in CPC value. Therefore, if the air gap thickness is appropriately optimized, in a way not to have a considerable reduction rate of permeate flux compare to DCMD, the AGMD system can be a better option for desalination.

5.2 Future Perspectives

MD is a burgeoning technology that needs more investigations and improvements to be deployed in large scale industrial applications. So here, we highlight a few recommendations and ideas which can be carried out in the near future.

(1) The major challenge in the MD process is membrane pore wetting and fouling. If the membrane for the MD process is fabricated with high antifouling properties with the capability to prevent wetting, the membrane distillation can be utilized for treating a wide range of industrial wastewaters, especially the wastewaters with high temperature containing several pollutants such as steam-assisted gravity drainage (SAGD) produced water. Therefore, developing long-life, reliable, thermally-stable, and low-cost membranes that are

resistant against pore wetting and fouling due to the presence of contaminants leaves more room for future study. Fabricating nanocomposite membranes having the omniphobic (hydrophobic and oleophobic) properties is an attempt to develop fouling resistance membranes with higher permeate flux. These properties enhance the resistance against oil and surfactant contamination in the feed solution. The presence of fillers (e.g., graphene, carbon nanotubes, silica nanoparticles, etc.) can create the antifouling properties in membranes and enhance the permeate flux by increasing the porosity and pore size of the membranes [22,45].

(2) To reduce the operational costs, energy consumption, and adverse effects on the environment because of using unsustainable energy sources for heating the feed solution, renewable energy (solar energy) can be contributed to the MD process. As future work, the cost analysis and energy efficiency can be investigated if the MD process couples with renewable energy sources.

(3) MD technology might be effective at water filtration when both the permeate and feed streams are at equal or nearly equal temperatures; however, low energy heating elements on the contaminated feed side would be needed and would represent a novel extension of this current study. Therefore, another way to reduce the energy consumption in the MD process is by fabricating the membrane that capable of creating the driving force by applying a small amount of electric current on the membrane surface. It prevents consuming a large amount of energy for heating the feed solution. However, it needs in-depth knowledge of the properties of different materials and polymers and various fabrication techniques to guide how this kind of membranes can be fabricated. Moreover, the mathematical modeling of this process also can be helpful here to find out what properties of membrane materials are more suitable for providing the temperature difference by low energy consumption [156].

(4) The other future work which might be influential in membrane-based treatment processes is combining the membrane process (MD here) with the Advanced-Oxidation process (AOP). Membrane technology is a physical barrier and can separate pure water from the contaminated solution; however, at the end of the separation process, the feed solution becomes more concentrated, containing hazardous organic/inorganic matters. Therefore, we need to find a solution to treat the produced concentrated solution. AOP is a chemical process that could degrade the hazardous pollutants into nontoxic materials. This process has some challenges related to using the chemicals and temperature in the MD process and can be studied as a promising technology for future works.

6 References

[1] Green Facts, Facts on Water Resources, United Nations World Water Dev. Rep. (n.d.). https://www.greenfacts.org/en/water-resources/index.htm.

[2] I. Hitsov, Model based analysis and optimization of membrane distillation, 2017.

[3] Green Facts, Water and Climate Change, United Nations Educ. Sci. Cult. Organ. (2020) 243. https://www.greenfacts.org/en/water-resources/index.htm.

[4] N.W. Arnell, Climate change and global water resources: SRES emissions and socio-economic scenarios, Glob. Environ. Chang. 14 (2004) 31–52. doi:10.1016/j.gloenvcha.2003.10.006.

[5] Green Facts, Wastewater The Untapped Resource, United Nations Educ. Sci. Cult. Organ. 53 (n.d.) 1689–1699. https://www.greenfacts.org/en/water-resources/index.htm.

[6] B. Khorshidi Mianaee, Advanced Thin Film Composite and Nanocomposite Polyamide membrane for water treatment, 2017.

[7] Progress on sanitation and drinking water– 2015 update and MDG assessment, World Health Organization and UNICEF Joint Monitoring Programme (JMP), n.d., 2015.

[8] B.L. Pangarkar, M.G. Sane, M. Guddad, Reverse Osmosis and Membrane Distillation for Desalination of Groundwater: A Review, ISRN Mater. Sci. 2011 (2011) 1–9. doi:10.5402/2011/523124.

[9] A. Khalifa, H. Ahmad, M. Antar, T. Laoui, M. Khayet, Experimental and theoretical investigations on water desalination using direct contact membrane distillation, Desalination. 404 (2017) 22–34. doi:10.1016/j.desal.2016.10.009.

[10] Food and Agriculture Organizations, Coping with water scarcity An action framework for

agriculture and food security 8 Coping with water scarcity An action framework for agriculture and food security, 2012. http://www.fao.org/docrep/016/i3015e/i3015e.pdf.

[11] Coping with water scarcity, challenge of the twenty-first century, 2007. http://ci.nii.ac.jp/naid/40005232449/.

[12] The Global Risks Report 2019, 14th Edition, World Economic Forum, 2019.

[13] D.U. Lawal, Desalination using air gap membane distillation, 2014.

[14] Mike Hightower and Suzanne A. Pierce, the Energy Challenge, 2008. doi:10.1111/j.1467-8292.1982.tb01436.x.

[15] X. Li, H. Xu, J. Liu, J. Zhang, J. Li, Z. Gui, Cyclonic state micro-bubble flotation column in oil-in-water emulsion separation, Sep. Purif. Technol. 165 (2016) 101–106. doi:10.1016/j.seppur.2016.01.021.

[16] X. Yue, J. Li, T. Zhang, F. Qiu, D. Yang, M. Xue, In situ one-step fabrication of durable superhydrophobic-superoleophilic cellulose/LDH membrane with hierarchical structure for efficiency oil/water separation, Chem. Eng. J. 328 (2017) 117–123. doi:10.1016/j.cej.2017.07.026.

[17] B.S. Al-Anzi, O.C. Siang, Recent developments of carbon based nanomaterials and membranes for oily wastewater treatment, RSC Adv. 7 (2017) 20981–20994. doi:10.1039/c7ra02501g.

[18] C. Ao, W. Yuan, J. Zhao, X. He, X. Zhang, Q. Li, T. Xia, W. Zhang, C. Lu, Superhydrophilic graphene oxide@electrospun cellulose nanofiber hybrid membrane for high-efficiency oil/water separation, Carbohydr. Polym. 175 (2017) 216–222. doi:10.1016/j.carbpol.2017.07.085.

[19] D. Winter, A Thermodynamic , Technological and Technological and Economic Analysis,

2014.

[20] J. Swaminathan, Unified Framework to Design Efficient Membrane Distillation for Brine Concentration, 2017.

[21] T.M. Khayet Mohamed, Membrane distillation principles and applications, 2011. doi:10.1016/B978-0-444-53126-1.10016-8.

[22] M.S. and T. Mohammadi, Nanocomposit membranes for water and gas separation, 2020.

[23] [online] DesalData.com, Global Water Intelligence, access in 2020, July 10th., (n.d.).

[24] L.M. Camacho, L. Dumée, J. Zhang, J. Li, M. Duke, Advances in Membrane Distillation for Water Desalination and Purification Applications, (2013) 94–196. doi:10.3390/w5010094.

[25] T. Mezher, H. Fath, Z. Abbas, A. Khaled, Techno-economic assessment and environmental impacts of desalination technologies, Desalination. 266 (2011) 263–273. doi:10.1016/j.desal.2010.08.035.

[26] A.N.A. Mabrouk, Techno-economic analysis of tube bundle orientation for high capacity brine recycle MSF desalination plants, Desalination. 320 (2013) 24–32. doi:10.1016/j.desal.2013.04.014.

[27] S.O. Olatunji, L.M. Camacho, Heat and mass transport in modeling membrane distillation configurations: A review, Front. Energy Res. 6 (2018) 1–18. doi:10.3389/fenrg.2018.00130.

[28] Andrea Cipollina · Giorgio Micale · Lucio Rizzuti, Seawater Desalination: Conventional and Renewable Energy Processes, 2012. doi:10.2174/97816080528511120101.

[29] S. Al-Amshawee, M.Y.B.M. Yunus, A.A.M. Azoddein, D.G. Hassell, I.H. Dakhil, H.A.

Hasan, Electrodialysis desalination for water and wastewater: A review, Chem. Eng. J. 380 (2020). doi:10.1016/j.cej.2019.122231.

[30] S. Burn, M. Hoang, D. Zarzo, F. Olewniak, E. Campos, B. Bolto, O. Barron, Desalination techniques - A review of the opportunities for desalination in agriculture, Desalination. 364 (2015) 2–16. doi:10.1016/j.desal.2015.01.041.

[31] R. Borsani, S. Rebagliati, Fundamentals and costing of MSF desalination plants and comparison with other technologies, Desalination. 182 (2005) 29–37. doi:10.1016/j.desal.2005.03.007.

[32] A. Al-Karaghouli, L.L. Kazmerski, Energy consumption and water production cost of conventional and renewable-energy-powered desalination processes, Renew. Sustain. Energy Rev. 24 (2013) 343–356. doi:10.1016/j.rser.2012.12.064.

[33] I.S. Al-Mutaz, A.M. Al-Namlah, Characteristics of dual purpose MSF desalination plants, Desalination. 166 (2004) 287–294. doi:10.1016/j.desal.2004.06.083.

[34] A.K. El-Feky, Simulation of a giant MSF recirculation plants, Desalin. Water Treat. 51 (2013) 1511–1518. doi:10.1080/19443994.2012.714859.

[35] J.E. Miller, Review of Water Resources and Desalination Technologies, Sandia Lab. SAND. (2009).

[36] Marcel Mulder, Basic principle of membrane technology, KLUWER ACADEMIC PUBLISHERS, 1996.

[37] RICHARD W. BAKER, Membrane Technology and Applications, Third, 2012. doi:10.1017/CBO9781107415324.004.

[38] A. Al-Karaghouli, D. Renne, L.L. Kazmerski, Technical and economic assessment of photovoltaic-driven desalination systems, Renew. Energy. 35 (2010) 323–328.

doi:10.1016/j.renene.2009.05.018.

[39] A. Gambier, A. Wellenreuther, E. Badreddin, Optimal control of a reverse osmosis desalination plant using multi-objective optimization, Proc. IEEE Int. Conf. Control Appl. (2007) 1368–1373. doi:10.1109/CCA.2006.286057.

[40] A. Gambier, E. Badreddin, Control of small reverse osmosis desalination plants with feed water bypass, Proc. IEEE Int. Conf. Control Appl. (2009) 800–805. doi:10.1109/CCA.2009.5281041.

[41] T. Younos, Environmental Issues of Desalination, J. Contemp. Water Res. Educ. 132 (2009) 11–18. doi:10.1111/j.1936-704x.2005.mp132001003.x.

[42] V.G. Gude, N. Nirmalakhandan, S. Deng, Renewable and sustainable approaches for desalination, Renew. Sustain. Energy Rev. 14 (2010) 2641–2654. doi:10.1016/j.rser.2010.06.008.

[43] H. Abu Qdais, Environmental impacts of the mega desalination project: the Red-Dead Sea conveyor, Desalination. 220 (2008) 16–23. doi:10.1016/j.desal.2007.01.019.

[44] S. Lattemann, T. Höpner, Environmental impact and impact assessment of seawater desalination, Desalination. 220 (2008) 1–15. doi:10.1016/j.desal.2007.03.009.

[45] S. Noamani, S. Niroomand, M. Rastgar, M. Sadrzadeh, Carbon-based polymer nanocomposite membranes for oily wastewater treatment, Npj Clean Water. 2 (2019) 1–14. doi:10.1038/s41545-019-0044-z.

[46] M. Shannon, P.W. Bohn, M. Elimelech, J.G. Georgiadis, B.J. Mariñas, A.M. Mayes, Science and technology for water purification in the coming decades, Nature. 452 (2008) 301–310. doi:10.1038/nature06599.

[47] S. Wu, Analysis of water production costs of a nuclear desalination plant with a nuclear

heating reactor coupled with MED processes, Desalination. 190 (2006) 287–294. doi:10.1016/j.desal.2005.08.010.

[48] S. Wu, Z. Zhang, An approach to improve the economy of desalination plants with a nuclear heating reactor by coupling with hybrid technologies, Desalination. 155 (2003) 179–185. doi:10.1016/S0011-9164(03)00295-9.

[49] A. Ophir, F. Lokiec, Advanced MED process for most economical sea water desalination, Desalination. 182 (2005) 187–198. doi:10.1016/j.desal.2005.02.026.

[50] M.G. Buonomenna, J. Bae, Membrane processes and renewable energies, Renew. Sustain. Energy Rev. 43 (2015) 1343–1398. doi:10.1016/j.rser.2014.11.091.

[51] A. Subramani, J.G. Jacangelo, Emerging desalination technologies for water treatment: A critical review, Water Res. 75 (2015) 164–187. doi:10.1016/j.watres.2015.02.032.

[52] D. Zhao, L.Y. Lee, S.L. Ong, P. Chowdhury, K.B. Siah, H.Y. Ng, Electrodialysis reversal for industrial reverse osmosis brine treatment, Sep. Purif. Technol. 213 (2019) 339–347. doi:10.1016/j.seppur.2018.12.056.

[53] M.J.K. Ahmed, M. Ahmaruzzaman, A review on potential usage of industrial waste materials for binding heavy metal ions from aqueous solutions, J. Water Process Eng. 10 (2016) 39–47. doi:10.1016/j.jwpe.2016.01.014.

[54] U. Lachish, Osmosis and thermodynamics, Am. J. Phys. 75 (2007) 997–998. doi:10.1119/1.2752822.

[55] S.A. Avlonitis, Operational water cost and productivity improvements for small-size RO desalination plants, Desalination. 142 (2002) 295–304. doi:10.1016/S0011-9164(02)00210-2.

[56] R. Semiat, Energy issues in desalination processes, Environ. Sci. Technol. 42 (2008) 8193–

8201. doi:10.1021/es801330u.

[57] A. Alkhudhiri, N. Darwish, N. Hilal, Membrane distillation: A comprehensive review, Desalination. 287 (2012) 2–18. doi:10.1016/j.desal.2011.08.027.

[58] K.-J.L.T.-S. Chung, Membrane Distillation Membranes, Hybrid Systems, and Pilot Studies, 2019. doi:10.1017/CBO9781107415324.004.

[59] A.S. Hassan, H.E.S. Fath, Review and assessment of the newly developed MD for desalination processes, Desalin. Water Treat. 51 (2013) 574–585. doi:10.1080/19443994.2012.697273.

[60] E. Curcio, E. Drioli, Membrane distillation and related operations - A review, Sep. Purif. Rev. 34 (2005) 35–86. doi:10.1081/SPM-200054951.

[61] Z. Ding, L. Liu, Z. Li, R. Ma, Z. Yang, Experimental study of ammonia removal from water by membrane distillation (MD): The comparison of three configurations, J. Memb. Sci. 286 (2006) 93–103. doi:10.1016/j.memsci.2006.09.015.

[62] P. Taylor, C. Huayan, W. Chunrui, J. Yue, W. Xuan, L. Xiaolong, C. Huayan, W. Chunrui, J. Yue, W. Xuan, L. Xiaolong, Comparison of three membrane distillation confi gurations and seawater desalination by vacuum membrane distillation, Desalin. Water Treat. (2013) 37–41.

[63] M.S. El-bourawi, Z. Ding, R. Ma, M. Khayet, A framework for better understanding membrane distillation separation process, Membr. Sci. 285 (2006) 4–29. doi:10.1016/j.memsci.2006.08.002.

[64] A.R. Tehrani-Bagha, Waterproof breathable layers – A review, Adv. Colloid Interface Sci. 268 (2019) 114–135. doi:10.1016/j.cis.2019.03.006.

[65] F. Macedonio, E. Drioli, Pressure-driven membrane operations and membrane distillation

technology integration for water purification, Desalination. 223 (2008) 396–409. doi:10.1016/j.desal.2007.01.200.

[66] S. Fadhil, Q.F. Alsalhy, H.F. Makki, R. Ruby-Figueroa, T. Marino, A. Criscuoli, F. Macedonio, L. Giorno, E. Drioli, A. Figoli, Seawater desalination using PVDF-HFP membrane in DCMD process: assessment of operating condition by response surface method, Chem. Eng. Commun. 206 (2019) 237–246. doi:10.1080/00986445.2018.1483349.

[67] A. Mustafa, M. Aljumaily, A. Alsaadi, N.A. Hashim, Q.F. Alsalhy, F.S. Mjalli, M.A. Atieh, A. Al-harrasi, PVDF-co-HFP/superhydrophobic acetylene-based nanocarbon hybrid membrane for seawater desalination via DCMD, Chem. Eng. Res. Des. (2018). doi:10.1016/j.cherd.2018.08.032.

[68] J. Lee, Y. Kim, L. Francis, G. Amy, Performance modeling of direct contact membrane distillation (DCMD) seawater desalination process using a commercial composite membrane, J. Memb. Sci. (2014). doi:10.1016/j.memsci.2014.12.053.

[69] N.A. Hashim, Q.F. Alsalhy, R. Das, F.S. Mjalli, Embedded high-hydrophobic CNMs prepared by CVD technique with PVDF-co-HFP membrane for application in water desalination by DCMD, Desalin. Water Treat. 142 (2019) 23431. doi:10.5004/dwt.2019.23431.

[70] J. Kujawa, E. Guillen-Burrieza, H.A. Arafat, M. Kurzawa, A. Wolan, W. Kujawski, Raw Juice Concentration by Osmotic Membrane Distillation Process with Hydrophobic Polymeric Membranes, Food Bioprocess Technol. 8 (2015) 2146–2158. doi:10.1007/s11947-015-1570-4.

[71] K.S.M.S. Raghavarao, Membrane distillation for the concentration of raw cane-sugar syrup and membrane clarified sugarcane juice, Desalination. 147 (2002) 157–160.

[72] L. Terki, W. Kujawski, J. Kujawa, M. Kurzawa, A. Filipiak-szok, E. Chrzanowska, S. Khaled, K. Madani, Implementation of osmotic membrane distillation with various

hydrophobic porous membranes for concentration of sugars solutions and preservation of the quality of cactus pear juice, J. Food Eng. (2018). doi:10.1016/j.jfoodeng.2018.02.023.

[73] C.A. Quist-jensen, F. Macedonio, C. Conidi, A. Cassano, S. Aljlil, O.A. Alharbi, Direct contact membrane distillation for the concentration of clarified orange juice, J. Food Eng. 187 (2016) 37–43. doi:10.1016/j.jfoodeng.2016.04.021.

[74] X. An, Y. Hu, N. Wang, Z. Zhou, Z. Liu, Continuous juice concentration by integrating forward osmosis with membrane distillation using potassium sorbate preservative as a draw solute, J. Memb. Sci. 573 (2019) 192–199. doi:10.1016/j.memsci.2018.12.010.

[75] M.C. Garc, C.A. Rivier, I.W. Marison, U. Von Stockar, Separation of binary mixtures by thermostatic sweeping gas membrane distillation II . Experimental results with aqueous formic acid solutions, Membr. Sci. 198 (2002) 197–210.

[76] C.A. Rivier, M.C. Garc, I.W. Marison, U. Von Stockar, Separation of binary mixtures by thermostatic sweeping gas membrane distillation I . Theory and simulations, Membr. Sci. 201 (2002) 1–16.

[77] H. Udriot, A. Araque, U. Von Stockar, Azeotropic mixtures may be broken by membrane distillation, Chem. Eng. 54 (1994) 87–93.

[78] I.W.A. Publishing, W. Science, Direct contact membrane distillation for textile wastewater treatment : a state of the art review Heloisa Ramlow , Ricardo Antonio Francisco Machado, Water Sci. Technol. |. (2017) 2565–2579. doi:10.2166/wst.2017.449.

[79] M.C. Carnevale, E. Gnisci, J. Hilal, A. Criscuoli, Direct Contact and Vacuum Membrane Distillation application for the olive mill wastewater treatment, Sep. Purif. Technol. (2016). doi:10.1016/j.seppur.2016.06.002.

[80] M. Khayet, Membranes and theoretical modeling of membrane distillation: A review, Adv. Colloid Interface Sci. 164 (2011) 56–88. doi:10.1016/j.cis.2010.09.005.

[81] L. Eykens, K. De Sitter, C. Dotremont, L. Pinoy, B. Van der Bruggen, Membrane synthesis for membrane distillation: A review, Sep. Purif. Technol. 182 (2017) 36–51. doi:10.1016/j.seppur.2017.03.035.

[82] R. Bouchrit, A. Boubakri, A. Ha, S.A. Bouguecha, Direct contact membrane distillation : Capability to treat hyper-saline solution, Desalination, ELSEVIER. 376 (2015) 117–129. doi:10.1016/j.desal.2015.08.014.

[83] M. Boukhriss, S. Khemili, M.B. Ben Hamida, H. Ben Bacha, Simulation and experimental study of an AGMD membrane distillation pilot for the desalination of seawater or brackish water with zero liquid discharged, Heat Mass Transf. Und Stoffuebertragung. 54 (2018) 3521–3531. doi:10.1007/s00231-018-2383-6.

[84] M. Gryta, M. Tomaszewska, Heat transport in the membrane distillation process, J. Memb. Sci. 144 (1998) 211–222. doi:10.1016/S0376-7388(98)00050-7.

[85] J. Phattaranawik, R. Jiraratananon, A.G. Fane, Heat transport and membrane distillation coefficients in direct contact membrane distillation, J. Memb. Sci. 212 (2003) 177–193. doi:10.1016/S0376-7388(02)00498-2.

[86] A. Ali, F. Macedonio, E. Drioli, S. Aljlil, O.A. Alharbi, Experimental and theoretical evaluation of temperature polarization phenomenon in direct contact membrane distillation, Chem. Eng. Res. Des. 91 (2013) 1966–1977. doi:10.1016/j.cherd.2013.06.030.

[87] M. Gryta, M. Tomaszewska, A.W. Morawski, Membrane distillation with laminar flow, Sep. Purif. Technol. 11 (1997) 93–101. doi:10.1016/S1383-5866(97)00002-6.

[88] M. Qtaishat, T. Matsuura, B. Kruczek, M. Khayet, Heat and mass transfer analysis in direct contact membrane distillation, Desalination. 219 (2008) 272–292. doi:10.1016/j.desal.2007.05.019.

[89] I. Hitsov, T. Maere, K. De Sitter, C. Dotremont, I. Nopens, Modelling approaches in

membrane distillation: A critical review, Sep. Purif. Technol. 142 (2015) 48–64. doi:10.1016/j.seppur.2014.12.026.

[90] A. Bahmanyar, M. Asghari, N. Khoobi, Numerical simulation and theoretical study on simultaneously effects of operating parameters in direct contact membrane distillation, Chem. Eng. Process. Process Intensif. 61 (2012) 42–50. doi:10.1016/j.cep.2012.06.012.

[91] R.W. Schofield, A.G. Fane, C.J.D. Fell, Gas and vapour transport through microporous membranes. I. Knudsen-Poiseuille transition, J. Memb. Sci. 53 (1990) 159–171. doi:10.1016/0376-7388(90)80011-A.

[92] R.W. Schofield, A.G. Fane, C.J.D. Fell, R. Macoun, Factors affecting flux in membrane distillation, Desalination. 77 (1990) 279–294. doi:10.1016/0011-9164(90)85030-E.

[93] C. Fernández-Pineda, M.A. Izquierdo-Gil, M.C. García-Payo, Gas permeation and direct contact membrane distillation experiments and their analysis using different models, J. Memb. Sci. 198 (2002) 33–49. doi:10.1016/S0376-7388(01)00605-6.

[94] K.W. Lawson, D.R. Lloyd, Membrane distillation, J. Memb. Sci. 124 (1997) 1–25.

[95] S.K. Loyalka, Gas transport in porous media: The dusty gas model, 1984. doi:10.1016/0021-9797(84)90035-3.

[96] K.W. Lawson, D.R. Lloyd, Membrane distillation. II. Direct contact MD, J. Memb. Sci. 120 (1996) 123–133. doi:10.1016/0376-7388(96)00141-X.

[97] R.W. Field, H.Y. Wu, J.J. Wu, Multiscale modeling of membrane distillation: Some theoretical considerations, Ind. Eng. Chem. Res. 52 (2013) 8822–8828. doi:10.1021/ie302363e.

[98] E. Close, E. Sørensen, Modelling of direct contact membrane distillation for desalination, Elsevier B.V., 2010. doi:10.1016/S1570-7946(10)28109-9.

[99] S. Srisurichan, R. Jiraratananon, A.G. Fane, Mass transfer mechanisms and transport resistances in direct contact membrane distillation process, J. Memb. Sci. 277 (2006) 186–194. doi:10.1016/j.memsci.2005.10.028.

[100] M. Khayet, A. Velázquez, J.I. Mengual, Modelling mass transport through a porous partition: Effect of pore size distribution, J. Non-Equilibrium Thermodyn. 29 (2004) 279–299. doi:10.1515/JNETDY.2004.055.

[101] J. Phattaranawik, R. Jiraratananon, A.G. Fane, Effect of pore size distribution and air flux on mass transport in direct contact membrane distillation, Membr. Sci. 215 (2003) 75–85. doi:10.1016/S0376-7388(02)00603-8.

[102] A. Cipollina, A. Di Miceli, J. Koschikowski, G. Micale, L. Rizzuti, CFD simulation of a membrane distillation module channel, Desalin. Water Treat. 6 (2009) 177–183. doi:10.5004/dwt.2009.664.

[103] M. Shakaib, S.M.F. Hasani, I. Ahmed, R.M. Yunus, A CFD study on the effect of spacer orientation on temperature polarization in membrane distillation modules, Desalination. 284 (2012) 332–340. doi:10.1016/j.desal.2011.09.020.

[104] S. Al-Sharif, M. Albeirutty, A. Cipollina, G. Micale, Modelling flow and heat transfer in spacer-filled membrane distillation channels using open source CFD code, Desalination. 311 (2013) 103–112. doi:10.1016/j.desal.2012.11.005.

[105] H. Yu, X. Yang, R. Wang, A.G. Fane, Numerical simulation of heat and mass transfer in direct membrane distillation in a hollow fiber module with laminar flow, J. Memb. Sci. 384 (2011) 107–116. doi:10.1016/j.memsci.2011.09.011.

[106] H. Yu, X. Yang, R. Wang, A.G. Fane, Analysis of heat and mass transfer by CFD for performance enhancement in direct contact membrane distillation, J. Memb. Sci. 405–406 (2012) 38–47. doi:10.1016/j.memsci.2012.02.035.

[107] X. Yang, H. Yu, R. Wang, A.G. Fane, Analysis of the effect of turbulence promoters in hollow fiber membrane distillation modules by computational fluid dynamic (CFD) simulations, J. Memb. Sci. 415–416 (2012) 758–769. doi:10.1016/j.memsci.2012.05.067.

[108] X. Yang, H. Yu, R. Wang, A.G. Fane, Optimization of microstructured hollow fiber design for membrane distillation applications using CFD modeling, J. Memb. Sci. 421–422 (2012) 258–270. doi:10.1016/j.memsci.2012.07.022.

[109] H.J. Hwang, K. He, S. Gray, J. Zhang, I.S. Moon, Direct contact membrane distillation (DCMD): Experimental study on the commercial PTFE membrane and modeling, J. Memb. Sci. 371 (2011) 90–98. doi:10.1016/j.memsci.2011.01.020.

[110] M. Khayet, C. Cojocaru, Artificial neural network modeling and optimization of desalination by air gap membrane distillation, Sep. Purif. Technol. 86 (2012) 171–182. doi:10.1016/j.seppur.2011.11.001.

[111] M. Khayet, C. Cojocaru, Artificial neural network model for desalination by sweeping gas membrane distillation, Desalination. 308 (2013) 102–110. doi:10.1016/j.desal.2012.06.023.

[112] A. Abraham, Artificia Neural Networks, Handb. Meas. Syst. Des. (2005).

[113] P. Onsekizoglu, K. Savas Bahceci, J. Acar, The use of factorial design for modeling membrane distillation, J. Memb. Sci. 349 (2010) 225–230. doi:10.1016/j.memsci.2009.11.049.

[114] M. Khayet, C. Cojocaru, C. García-Payo, Application of response surface methodology and experimental design in direct contact membrane distillation, Ind. Eng. Chem. Res. 46 (2007) 5673–5685. doi:10.1021/ie070446p.

[115] M. Khayet, C. Cojocaru, A. Baroudi, Modeling and optimization of sweeping gas membrane distillation, Desalination. 287 (2012) 159–166. doi:10.1016/j.desal.2011.04.070.

[116] V.T. Shahu, S.B. Thombre, Air gap membrane distillation: A review, J. Renew. Sustain. Energy. 11 (2019). doi:10.1063/1.5063766.

[117] A. Khalifa, D. Lawal, M. Antar, M. Khayet, Experimental and theoretical investigation on water desalination using air gap membrane distillation, Desalination. 376 (2015) 94–108. doi:10.1016/j.desal.2015.08.016.

[118] A.E. Khalifa, D.U. Lawal, M.A. Antar, Performance of air gap membrane distillation unit for water desalination, ASME Int. Mech. Eng. Congr. Expo. Proc. 6A (2014) 1–6. doi:10.1115/IMECE2014-36031.

[119] E.K. Summers, H.A. Arafat, J.H. Lienhard V, Energy efficiency comparison of single-stage membrane distillation (MD) desalination cycles in different configurations, Desalination. 290 (2012) 54–66. doi:10.1016/j.desal.2012.01.004.

[120] H. Geng, Q. He, H. Wu, P. Li, C. Zhang, H. Chang, Experimental study of hollow fiber AGMD modules with energy recovery for high saline water desalination, Desalination. 344 (2014) 55–63. doi:10.1016/j.desal.2014.03.016.

[121] I. Hitsov, L. Eykens, W. De Schepper, K. De Sitter, C. Dotremont, I. Nopens, Full-scale direct contact membrane distillation (DCMD) model including membrane compaction effects, J. Memb. Sci. 524 (2017) 245–256. doi:10.1016/j.memsci.2016.11.044.

[122] Ó. Andrjesdóttir, C.L. Ong, M. Nabavi, S. Paredes, A.S.G. Khalil, B. Michel, D. Poulikakos, An experimentally optimized model for heat and mass transfer in direct contact membrane distillation, Int. J. Heat Mass Transf. 66 (2013) 855–867. doi:10.1016/j.ijheatmasstransfer.2013.07.051.

[123] E.N. Sieder, G.E. Tate, Heat Transfer and Pressure Drop of Liquids in Tubes, Ind. Eng. Chem. 28 (1936) 1429–1435. doi:10.1021/ie50324a027.

[124] M.I. Va, Temperature and concentration polarization in membrane distillation of aqueous

salt solutions, Membr. Sci. 156 (1999).

[125] J.G. Lee, E.J. Lee, S. Jeong, J. Guo, A.K. An, H. Guo, J. Kim, T.O. Leiknes, N. Ghaffour, Theoretical modeling and experimental validation of transport and separation properties of carbon nanotube electrospun membrane distillation, J. Memb. Sci. 526 (2017) 395–408. doi:10.1016/j.memsci.2016.12.045.

[126] G. Rao, S.R. Hiibel, A.E. Childress, Simplified flux prediction in direct-contact membrane distillation using a membrane structural parameter, Desalination. 351 (2014) 151–162. doi:10.1016/j.desal.2014.07.006.

[127] Y.M. Manawi, M. Khraisheh, A.K. Fard, F. Benyahia, S. Adham, Effect of operational parameters on distillate flux in direct contact membrane distillation (DCMD): Comparison between experimental and model predicted performance, Desalination. 336 (2014) 110–120. doi:10.1016/j.desal.2014.01.003.

[128] J. Swaminathan, H.W. Chung, D.M. Warsinger, J.H. Lienhard V, Membrane distillation model based on heat exchanger theory and configuration comparison, Appl. Energy. 184 (2016) 491–505. doi:10.1016/j.apenergy.2016.09.090.

[129] Q. He, P. Li, H. Geng, C. Zhang, J. Wang, H. Chang, Modeling and optimization of air gap membrane distillation system for desalination, Desalination. 354 (2014) 68–75. doi:10.1016/j.desal.2014.09.022.

[130] E. Drioli, A. Ali, F. Macedonio, Membrane distillation: Recent developments and perspectives, Desalination. 356 (2015) 56–84. doi:10.1016/j.desal.2014.10.028.

[131] A. Luo, N. Lior, Critical review of membrane distillation performance criteria, Desalin. Water Treat. 57 (2016) 20093–20140. doi:10.1080/19443994.2016.1152637.

[132] I. El Mokhtar, A. Boubakri, S.A.T. Bouguecha, A. Hafiane, Modeling and experimental study of air gap membrane distillation unit: Application for seawater desalination, Desalin.

Water Treat. 154 (2019) 72–81. doi:10.5004/dwt.2019.23889.

[133] E. Karbasi, J. Karimi-Sabet, J. Mohammadi-Rovshandeh, M. Ali Moosavian, H. Ahadi, Y. Amini, Experimental and numerical study of air-gap membrane distillation (AGMD): Novel AGMD module for Oxygen-18 stable isotope enrichment, Chem. Eng. J. 322 (2017) 667–678. doi:10.1016/j.cej.2017.03.031.

[134] J. Xu, Y.B. Singh, G.L. Amy, N. Ghaffour, Effect of operating parameters and membrane characteristics on air gap membrane distillation performance for the treatment of highly saline water, J. Memb. Sci. 512 (2016) 73–82. doi:10.1016/j.memsci.2016.04.010.

[135] F.A. Banat, J. Simandl, Desalination by Membrane Distillation: A Parametric Study, Sep. Sci. Technol. 33 (1998) 201–226. doi:10.1080/01496399808544764.

[136] D.P.D.F.P. Incropera, Fundemental of Heat and Mass Transfer, 7th ed, 2007. doi:10.16309/j.cnki.issn.1007-1776.2003.03.004.

[137] A. Kays, W. and London, N. York, Compact Heat Exchangers, 2nd edn, McGraw-Hill, Inc., 1964.

[138] L. Xu, S. Xu, X. Wu, P. Wang, D. Jin, J. Hu, L. Li, L. Chen, Q. Leng, D. Wu, Heat and mass transfer evaluation of air-gap diffusion distillation by ε-NTU method, Desalination. 478 (2020). doi:10.1016/j.desal.2019.114281.

[139] J.G. Lee, E.J. Lee, S. Jeong, J. Guo, A.K. An, H. Guo, J. Kim, T.O. Leiknes, N. Ghaffour, Theoretical modeling and experimental validation of transport and separation properties of carbon nanotube electrospun membrane distillation, J. Memb. Sci. 526 (2017) 395–408. doi:10.1016/j.memsci.2016.12.045.

[140] M. Essalhi, M. Khayet, Self-sustained webs of polyvinylidene fluoride electrospun nanofibers at different electrospinning times: 2. Theoretical analysis, polarization effects and thermal efficiency, J. Memb. Sci. 433 (2013) 180–191.

doi:10.1016/j.memsci.2013.01.024.

[141] G. Zuo, R. Wang, R. Field, A.G. Fane, Energy efficiency evaluation and economic analyses of direct contact membrane distillation system using Aspen Plus, Desalination. 283 (2011) 237–244. doi:10.1016/j.desal.2011.04.048.

[142] H. Chen, V. V. Ginzburg, J. Yang, Y. Yang, W. Liu, Y. Huang, L. Du, B. Chen, Thermal conductivity of polymer-based composites: Fundamentals and applications, Prog. Polym. Sci. 59 (2016) 41–85. doi:10.1016/j.progpolymsci.2016.03.001.

[143] W.N. Dos Santos, J.A. De Sousa, R. Gregorio, Thermal conductivity behaviour of polymers around glass transition and crystalline melting temperatures, Polym. Test. 32 (2013) 987–994. doi:10.1016/j.polymertesting.2013.05.007.

[144] E.S.P.B. V, M.Y. Keating, C.S. Mclaren, THERMAL CONDUCTIVITY OF POLYMER MELTS * Thermal conductivity (TC) is an important physical property of materials and describes the ability of that material to conduct heat . The property dictates the design of processing machinery and controls the speed, 166 (1990) 69–76.

[145] L. Eykens, I. Hitsov, K. De Sitter, C. Dotremont, L. Pinoy, B. Van der Bruggen, Direct contact and air gap membrane distillation: Differences and similarities between lab and pilot scale, Desalination. 422 (2017) 91–100. doi:10.1016/j.desal.2017.08.018.

[146] A. Criscuoli, M.C. Carnevale, E. Drioli, Evaluation of energy requirements in membrane distillation, Chem. Eng. Process. Process Intensif. 47 (2008) 1098–1105. doi:10.1016/j.cep.2007.03.006.

[147] J. Swaminathan, J.H. Lienhard, Design and operation of membrane distillation with feed recirculation for high recovery brine concentration, Desalination. 445 (2018) 51–62. doi:10.1016/j.desal.2018.07.018.

[148] M. Baghbanzadeh, C.Q. Lan, D. Rana, T. Matsuura, Membrane Distillation, Nanostructured

Polym. Membr. 1 (2016) 419–455. doi:10.1002/9781118831779.ch11.

[149] L. Eykens, T. Reyns, K. De Sitter, C. Dotremont, L. Pinoy, B. Van Der Bruggen, How to select a membrane distillation configuration ? Process conditions and membrane influence unraveled, Desalination. 399 (2016) 105–115. doi:10.1016/j.desal.2016.08.019.

[150] A.S. Alsaadi, N. Ghaffour, J.D. Li, S. Gray, L. Francis, H. Maab, G.L. Amy, Modeling of air-gap membrane distillation process: A theoretical and experimental study, J. Memb. Sci. 445 (2013) 53–65. doi:10.1016/j.memsci.2013.05.049.

[151] H. Attia, M.S. Osman, D.J. Johnson, C. Wright, N. Hilal, Modelling of air gap membrane distillation and its application in heavy metals removal, Desalination. 424 (2017) 27–36. doi:10.1016/j.desal.2017.09.027.

[152] I. Janajreh, K. El Kadi, R. Hashaikeh, R. Ahmed, Numerical investigation of air gap membrane distillation (AGMD): Seeking optimal performance, Desalination. 424 (2017) 122–130. doi:10.1016/j.desal.2017.10.001.

[153] B.G. Im, J.G. Lee, Y.D. Kim, W.S. Kim, Theoretical modeling and simulation of AGMD and LGMD desalination processes using a composite membrane, Elsevier B.V., 2018. doi:10.1016/j.memsci.2018.08.006.

[154] M.M.A. Shirazi, A. Kargari, A.F. Ismail, T. Matsuura, Computational Fluid Dynamic (CFD) opportunities applied to the membrane distillation process: State-of-the-art and perspectives, Desalination. 377 (2016) 73–90. doi:10.1016/j.desal.2015.09.010.

[155] H.C. Duong, P. Cooper, B. Nelemans, T.Y. Cath, L.D. Nghiem, Evaluating energy consumption of air gap membrane distillation for seawater desalination at pilot scale level, Sep. Purif. Technol. 166 (2016) 55–62. doi:10.1016/j.seppur.2016.04.014.

[156] A. Deshmukh, C. Boo, V. Karanikola, S. Lin, A.P. Straub, T. Tong, D.M. Warsinger, M. Elimelech, Membrane distillation at the water-energy nexus: Limits, opportunities, and

challenges, Energy Environ. Sci. 11 (2018) 1177–1196. doi:10.1039/c8ee00291f.

[157] T.Y. Kyrychok, Mechanical measurements, Meas. Tech. 57 (2014) 166–171. doi:10.1007/s11018-014-0424-1.

7 Appendices: More details on materials and methods

Appendix A Physical Properties of Saltwater

The physical properties of the feed solution (saltwater) are calculated with empirical correlations. The units for temperature T and salinity S are [◦C] and [g/kg], respectively [19].

A-1 Density

For temperatures from 10 to 180 ◦C and for salinities from 0 to 160 g/kg, the density ρ is calculated according to the following equations.

$$\rho = 0.5\, a_0 + a_1 Y + a_2 (2 Y^2 - 1) + a_3 (4 Y^3 - 3 Y) \quad \text{[kg/dm]} \tag{A1}$$

with:

$$a_0 = 2.01611 + 0.115313\, \sigma + 0.000326\, (2\, \sigma^2 - 1) \tag{A2}$$

$$a_1 = -0.0541 + 0.001571\, \sigma - 0.000423\, (2\, \sigma^2 - 1) \tag{A3}$$

$$a_2 = -0.006124 + 0.00174\, \sigma - 0.000009\, (2\, \sigma^2 - 1) \tag{A4}$$

$$a_3 = 0.000346 + 0.000087\, \sigma - 0.000053\, (2\, \sigma^2 - 1) \tag{A5}$$

And

$$Y = \frac{2\,T - 200}{160} \tag{A6}$$

$$\sigma = \frac{2\,S - 150}{150} \tag{A7}$$

A-2 Dynamic Viscosity

For temperatures from 10 to 180 ◦C and for salinity values from 0 to 130 g/kg, the dynamic viscosity μ is calculated by the following equations (1000 cP = 1 kg /(ms)) [19].

$$\mu = \mu_w \mu_R \qquad \text{[cP]} \tag{A8}$$

with:

$$ln(\mu_w) = -3.79418 + \frac{604.129}{139.18 + T} \tag{A9}$$

$$\mu_R = 1 + a_1 S + a_2 S^2 \tag{A10}$$

and

$$a_1 = 1.474 \times 10^{-3} + 1.5 \times 10^{-5} T - 3.927 \times 10^{-8} T^2 \tag{A11}$$

$$a_2 = 1.0734 \times 10^{-5} + 8.5 \times 10^{-8} T - 2.23 \times 10^{-10} T^2 \tag{A12}$$

A-3 Thermal Capacity

For temperatures from 0 to 180 ◦C and for salinity values from 0 to 160 g/kg, the thermal capacity c_p is calculated from the following equations [19].

$$c_p = A + BT + CT^2 + DT^3 \quad [\mathrm{J/(kgK)}] \tag{A13}$$

And

$$A = 4206.8 - 6.6197 S + 1.2288 \times 10^{-2} S^2 \tag{A14}$$

$$B = -1.1262 + 5.4178 \times 10^{-2} S - 2.2719 \times 10^{-4} S^2 \tag{A15}$$

$$C = 1.2026 \times 10^{-2} - 5.3566 \times 10^{-4} S + 1.8906 \times 10^{-6} S^2 \tag{A16}$$

$$D = 6.8774 \times 10^{-7} + 1.5170 \times 10^{-6} S - 4.4268 \cdot\times 10^{-9} S^2 \tag{A17}$$

A-4 Thermal Conductivity

For temperatures from 10 to 150 ◦C and for salinity values from 0 to 100 g/kg, the thermal conductivity k is calculated from the following equations [19].

$$k = (A + B\,T + C\,T^2) \times 10^{-3} \quad [\frac{\mathrm{W}}{\mathrm{m\,K}}] \tag{A18}$$

with

$$A = 576.6 - 34.64 X + 7.286 X^2 \tag{A19}$$

$$B = (1526 + 466.2 X - 226.8 X^2 + 28.67 X^3) \times 10^{-3} \tag{A20}$$

$$C = -(581 + 2055 X - 991.6 X^2 + 146.4 X^3) \times 10^{-5} \tag{A21}$$

$$X = \frac{28.17 S}{1000 - S} \tag{A22}$$

Appendix B Radiation heat transfer

Any object with a temperature greater than absolute zero temperature can emit thermal radiation. The heat transfer rate due to radiation can be calculated for two boddies with temperature of T_1 and T_2 from equation B.1.

$$Q = h_r(T_1 - T_2), \tag{B1}$$

$$h_r = \frac{\sigma(T_1 + T_2)({T_1}^2 + {T_2}^2)}{\frac{1}{E_1} + \frac{1}{E_2} - 1} \tag{B2}$$

where, h_r is radiation heat transfer coefficient and E is the emmisivity of each object. In our modeling in the MD system, the heat transfer coeafficient due to radiation is negligible in comparison to the heat transfer coefficient due to other heat transfer rates such as convection [136].

Appendix C Free and forced convection

Depending on how the fluid motion initiated, convection heat transfer is classified as natural (or free) and forced convection. In free convection, the fluid motion is caused by natural means not external forces such as the buoyancy effect, or density differences in the fluid occurring due to temperature gradients. While in forced convection, the fluid is forced to flow in a channel by external forces such as a pump. In free convection, Grashof (Gr) number plays the same role as the Reynolds number (Re) plays in the forced convection. Grashof number is defined by equation C1 which is the ratio of the buoyancy forces to the viscous forces acting on the fluid. By comparing the values of Gr and Re number, we can estimate that what type of convection can be occurred in the fluid channel as expalned in equations C2-C4 in the following [136].

$$Gr = \frac{g\beta(T_s - T_\infty){D_h}^3}{\vartheta^2} \tag{C1}$$

If $\frac{\mathrm{Gr}}{\mathrm{Re}^2} \ll 1$: Forced convection (C2)

If $\frac{\text{Gr}}{\text{Re}^2} \gg 1$: Free convection (C3)

If $\frac{\text{Gr}}{\text{Re}^2} = 1$: Mixed convection (C4)

where, g is the gravitational acceleration, β is the thermal expansion of fluid and ϑ is the kinematic viscousity.

Appendix D Nusselt Number calculation

Based on the fluid flow regime in the flow channel, the Nu number can be calculated from the following equations [2,9,21,80,122,123].

Re< 2100	Laminar flow	$Nu = 1.86\,(Re.Pr.D_h/Length)^{1/3}$	(D1)
210<Re<6000	Transient flow	$Nu = 0.116\,(Re^{\frac{2}{3}} - 125)(Pr^{\frac{1}{3}})(1 + (D_h/Length)^{\frac{2}{3}})$	(D2)
Re>6000	Turbulent flow	$Nu = 0.027\,\left(Re^{\frac{4}{5}}\right)\left(Pr^{\frac{1}{3}}\right) * \,(\mu_{bulk}/\mu_{surface})^{\,0.14}$	(D3)

where Reynolds number is $Re = \frac{\rho.u.D_h}{\mu}$, Prandtl number is $Pr = \frac{\mu.C_p}{k}$ and u is the velocity. The calculation for density (ρ), dynamic viscosity (μ) and specific heat capacity (C_p) are described for either feed or permeate solution in the above section.

Appendix E Concentration polarization effect

$$CPC = \frac{C_{mf}}{C_{bf}} \tag{E1}$$

$$C_{mf} = C_{bf}.e^{(\frac{J_w}{\rho_f.K})} \tag{E2}$$

$$K = Sh.Diff\,/D_h \tag{E3}$$

For laminar flow Re< 2100 $$Sh = 1.86(\,Re_f.SC.D_h/Length)^{0.33} \tag{E4}$$

For Turbulent flow Re> 2100 $$Sh = 0.023(\,Re_f)^{0.8}(SC)^{0.33} \tag{E5}$$

$$SC = \frac{\mu_{mf}}{\rho_f.\mathrm{Diff}} \tag{E6}$$

where, C_{mf} is the salt concentration on the membrane surface in the feed side, C_{bf} is the bulk salt concentration, K [m/s] is the overall mass transfer coefficient for salt particles through the concentration boundary layer in the feed side. SC is Schmidt number which is the ratio of momentum diffusivity to the mass diffusivity, Diff is t the diffusion coefficient of solute (NaCl here), and Sh is the Sherwood number, which is the ratio of convective to diffusive mass transport and it is dependent to Reynolds and Schmidt number.

Appendix F $\in -$NTU Equations for parallel flow

If the feed and permeate streams flow in the same direction on both sides of the membrane (co-current), the outlet temperatures are calculated based on the $\in -$NTU equations for parallel flow. In our study, the flow mode was counter current, but in the iteration loop of the modeling, the inlet permeate temperature was guessed as an initial guess for the first element. Therefore, from this point, the flow mode direction was assumed to be parallel flow, and the outlet temperatures were calculated based on the following equation for finding $\in$ [136,137].

$$C_c = \dot{m}_c c_{p,cold} \tag{F1}$$

$$C_h = \dot{m}_h c_{p,hot} \tag{F2}$$

$$C_{min} = Min\,(C_h\,,C_c) \tag{F3}$$

$$C_{max} = Max\,(C_h, C_c) \tag{F4}$$

$$NTU = U.(membrane\ area)/C_{min} \tag{F5}$$

$$C_r = \frac{C_{min}}{C_{max}} \tag{F6}$$

$$\in= \frac{1 - exp\,(-NTU(1 + C_r))}{1 + C_r} \tag{F7}$$

Appendix G Contact Angels of membranes surface

In the MD process, hydrophobic membranes were used. Two different kinds of commercial hydrophobic membranes, namely polytetrafluoroethylene (PTFE) and polyvinylidene difluoride (PVDF), which were acquired from Sterlitech (Kent, USA), were used for the experiments. The water contact angles of the membranes are illustrated in Table G.1.

Table G. 1. Water contact angles on the membrane surface

PTFE **0.1 µm** **138 °**	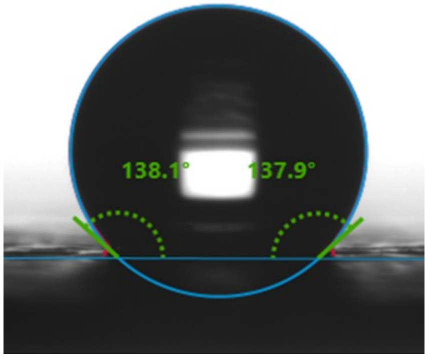	**PTFE** **0.2 µm** **135.5 °**	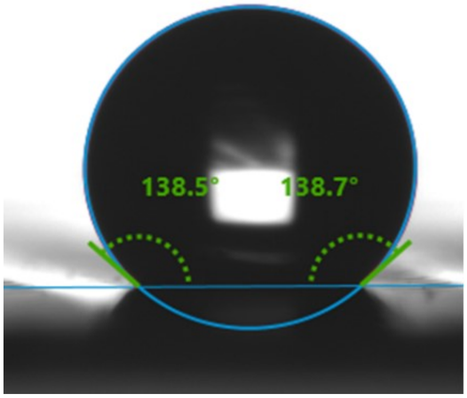
PTFE **0.45 µm** **123 °**	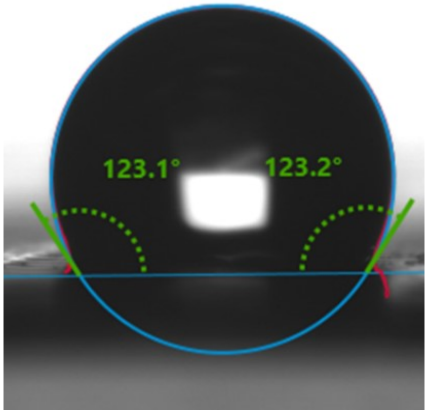	**PVDF** **0.3 µm** **95 °**	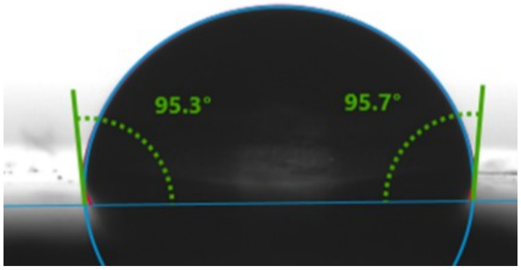

Appendix H Uncertainty analysis for mass flux measurement in experiments

The total uncertainty in the mass flux combines systematic and random uncertainties to maintain a 95% confidence interval. The error of a calculated parameter (mass flux) is determined from the errors propagated in the measured variables (Δm, t, and area), which is mathematically expressed by equations (H1 to H6). The systematic (Bias (B_x)) uncertainty is from the measurement calibration and upset of instruments. The precision or random uncertainty (P_x) is from data measurement and is calculated from equation (44) (Uncertainty for time (t) and area (A) can be neglected) [157].

$$permeate\ flux = \frac{\Delta m}{At}\ [\frac{kg}{m^2 hr}] \tag{H1}$$

$$\frac{U_{flux}}{flux} = \sqrt{(\frac{U_{\Delta m}}{\Delta m})^2 + (\frac{U_t}{t})^2 + (\frac{U_{area}}{A})^2} \tag{H2}$$

$$\frac{U_{flux}}{flux} = \sqrt{(\frac{U_{\Delta m}}{\Delta m})^2} \tag{H3}$$

$$(U_{\Delta m})^2 = (P_{mass})^2 + (B_{mass})^2 \tag{H4}$$

$$\frac{U_{flux}}{flux} = \frac{\sqrt{(P_{mass})^2 + (B_{mass})^2}}{\Delta m} \tag{H5}$$

$$P_x = t_{\frac{\alpha}{2},\vartheta} \cdot \frac{\delta_x}{\sqrt{n}} \qquad \alpha = 1 - c\ , \qquad \vartheta = n - 1 \tag{H6}$$

where δ_x, is the standard deviation of data (here is the mass in the permeate tank during the experiment over time), n is the number of measurements, and ϑ is the degree of freedom. The student t-distribution can be obtained from the standard table [157].C is a confidence interval, and the value of 95% is almost universally used in calculations. Student t-distribution is around 2 for more than 30 measurements and 95% of a confidence interval. Here, to find the precision uncertainty for the mass flux (P_{mass}), the STEYX function in Excel is used which returns the standard error of the predicted mass-value (kg) for each second (time) in the regression [157], and Bias fixed value is calculated based on the error in weight scale ($B_{mass} = \pm 5\ gr$).